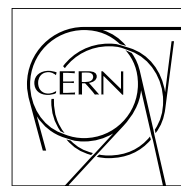


The Compact Muon Solenoid Experiment
Analysis Note

The content of this note is intended for CMS internal use and distribution only



22 March 2021 (v12, 02 February 2023)

Search for neutral long-lived particles decaying in the CMS Muon Barrel

James Sheplock, David Stuart, Matthew Citron, Daniel Diaz, Javier Duarte, Farouk Mokhtar, Cristian Pena, Joerg Schindler, Christina Wang, Si Xie

Abstract

A search for long-lived particles decaying in the Muon Barrel System is presented. The search utilizes the full Run 2 dataset totaling 137 fb^{-1} of proton-proton collisions recorded by the CMS experiment at $\sqrt{s} = 13 \text{ TeV}$. Hits in the Drift Tubes are clustered together and properties of the cluster are used to reject backgrounds. The results of the search are interpreted using a Twin Higgs model, showing sensitivity to Higgs-mediated long-lived particle production with proper lifetimes up to 100m. Limits are also set on a previously untested Dark Shower model.

1 Contents

2	1	Introduction	3
3	2	Executive summary	4
4	2.1	Changes from v2 to v3 of the analysis note	4
5	2.2	Changes from v3 to v4 of the analysis note	4
6	2.3	Changes from v4 to v5 of the analysis note	4
7	2.4	Changes from v5 to v6 of the analysis note	4
8	2.5	Changes from v6 to v7 of the analysis note	4
9	2.6	Changes from v7 to v8 of the analysis note	4
10	2.7	Changes from v9 to v10 of the analysis note	4
11	2.8	Changes from v10 to v11 of the analysis note	4
12	3	Datasets	5
13	3.1	Data	5
14	3.2	Signal simulation	5
15	4	Trigger strategy	9
16	4.1	Trigger efficiency	9
17	5	Physics objects	11
18	5.1	DT rechits	11
19	5.2	Jets	13
20	5.3	Muons	14
21	5.4	Missing transverse momentum	14
22	6	Event selection	15
23	6.1	Control regions	15
24	6.2	Background sources	16
25	6.3	Cluster vetoes	16
26	6.4	RPC matching	19
27	6.5	Overall detector activity	20
28	6.6	Orientation of cluster and missing transverse energy	21
29	6.7	Cluster size	23
30	6.8	Signal region orthogonality	23
31	6.9	DT noise	23
32	6.10	The signal regions	24
33	7	Background estimation	27
34	7.1	Testing the ABCD prediction method	28
35	7.2	Estimation of non-random background	28
36	8	Modeling of key variables	36
37	8.1	Muon bremsstrahlung comparison	36
38	8.2	Event level modeling	42
39	9	Uncertainties	45
40	9.1	Background uncertainties	45
41	9.2	Signal uncertainties	45
42	10	Results	47
43	11	Interpretation	48

44	11.1	Signal Efficiency	48
45	11.2	Likelihood model	49
46	11.3	Expected Limits	52
47	12	Summary	58
48	A	Dark Shower features	60
49	B	Punch-through background	63
50	B.1	Event displays	64
51	C	Control regions comparison	67
52	D	Dark shower Monte Carlo validation	70
53	E	Signal efficiency tables	76
54	E.1	4d and 4 τ final states	76
55	E.2	VBF production	76

DRAFT

56 1 Introduction

57 Many Beyond the Standard Model (BSM) theories predict long-lived particles that could be
 58 produced in LHC collisions [1]. The long-lived particles can decay hadronically to Standard
 59 Model particles. Searches for such signatures are particularly challenging for lighter long-lived
 60 particles, such as those produced in decays of the Higgs boson. A wide range of searches have
 61 targeted this signature using a range of detector subsystems at CMS and ATLAS [2–6]. For
 62 longer lifetimes, the sensitivity of searches for such signatures with the tracker is limited by ac-
 63 ceptance as decays typically occur beyond the tracker volume. Searches for long-lived particles
 64 decaying in the ATLAS calorimeter and the ATLAS muon system face very large backgrounds
 65 from QCD punch-through jets (see Section 6.2). In order to control such backgrounds, two
 66 displaced decays are required, which limits the reach in lifetime. The ATLAS muon system
 67 based search also contains a final state with a single displaced decay, however the sensitivity
 68 is limited by the $\mathcal{O}(100)$ of background events faced. The CMS Barrel Muon System provides
 69 an opportunity to substantially improve the reach for long lifetimes as it is interwoven with a
 70 thick iron return-yoke, dramatically reducing the punch-through jet background.

71 This note describes a search for long-lived particles using the CMS Barrel Muon System to
 72 detect showers from hadronic decays. These decays produce many hits in the Drift Tubes
 73 (DTs), and these hits are clustered using the DBSCAN algorithm. Several background processes
 74 can produce DT clusters, so these are rejected with various event and cluster requirements.
 75 Clusters are separated based on which station within the DT system contains the majority of
 76 the hits. The analysis uses two signal regions, one for events with a cluster in the second Barrel
 77 Muon System station (MB2) and one for events with a cluster in either the third or fourth
 78 station (MB3/4), in order to achieve optimal coverage in long-lived particle lifetime. An ABCD
 79 method is used to predict the random background contribution in each signal region, and a
 80 separate method is used to predict the contribution of the correlated background. These signal
 81 regions achieve backgrounds on the order of one event. This analysis is complementary to a
 82 related analysis that uses the CMS Endcap Muon System, and a combined interpretation of the
 83 results for signal models targeted by both analyses is planned [7].

84 The results of the analysis are interpreted using a "Twin Higgs" model where the Higgs boson
 85 decays to two long-lived scalars, which decay to a quark-antiquark pair [8, 9]. The phase space
 86 considered for the scalar covers masses up to 55 GeV and lifetimes up to 100 m. Additionally,
 87 a "Dark Shower" model is considered, in which the Higgs boson decays to dark QCD quarks
 88 that hadronize to showers of dark vector and scalar mesons that gradually decay to Standard
 89 Model (SM) particles. The dark shower forms an "emerging jet" signature [10], which has only
 90 previously been searched for in the case of heavy $\mathcal{O}(\text{TeV})$ scale mediators [11]. This analysis
 91 considers dark showers produced in Higgs decays with lifetimes up to 10 m and dark meson
 92 masses up to 20 GeV.

93 **2 Executive summary**

94 **2.1 Changes from v2 to v3 of the analysis note**

- 95 • Updated muon and jet vetoes
96 • Added punch-through background prediction
97 • Added signal systematics
98 • Updated dark shower signal model/MC

99 **2.2 Changes from v3 to v4 of the analysis note**

- 100 • Updated fit function for MB1 veto efficiency plot used in punch-through prediction
101 • Added punch-through background appendix

102 **2.3 Changes from v4 to v5 of the analysis note**

- 103 • Added punch-through prediction for MB3-4 signal region
104 • Added description of DT noise filter
105 • Added control region comparison appendix

106 **2.4 Changes from v5 to v6 of the analysis note**

- 107 • Extended lifetime range for dark shower models
108 • Added private/central MC comparison appendix for subset of dark shower models
109 • Included vetoes to keep single DT search independent from single CSC and double
110 cluster signal regions

111 **2.5 Changes from v6 to v7 of the analysis note**

- 112 • Updated signal yields and expected limits with additional Higgs production modes
113 • Included results for additional Twin Higgs signal model final states

114 **2.6 Changes from v7 to v8 of the analysis note**

- 115 • Included veto for CSC and double cluster analysis control regions

116 **2.7 Changes from v9 to v10 of the analysis note**

- 117 • Removed veto using number of stations and wheels with more than 25 rechits
118 • Added veto using number of DT segments in each hemisphere
119 • Modified the jet veto with larger cone for matching to leading jet
120 • Added MB2 and adjacent wheel MB2 rechit vetoes
121 • Added noise filter in 2018 data

122 **2.8 Changes from v10 to v11 of the analysis note**

- 123 • Added adjacent MB2 veto figured
124 • Minor typo fixes

125 **3 Datasets**

126 **3.1 Data**

127 This analysis uses proton-proton collision data at $\sqrt{s} = 13$ TeV from 2016, 2017 and 2018 corre-
 128 sponding to 35.9, 41.5 and 59.7 fb^{-1} respectively. The JSON files
 129 Cert_271036-284044_13TeV_23Sep2016ReReco_Collisions16_JSON.txt,
 130 Cert_294927-306462_13TeV_EOY2017ReReco_Collisions17_JSON_v1.txt and
 131 Cert_314472-325175_13TeV_PromptReco_Collisions18_JSON.txt are used to iden-
 132 tify the certified data.

133 The datasets used are shown below in Table 1. The analysis requires RECO datasets because
 134 the DT rechits that are clustered are only available at the RECO level. The high MET skim
 135 datasets are used.

Table 1: List of datasets used in this analysis.

```
/MET/Run2016B-HighMET-07Aug17_ver1-v1/RAW-RECO
/MET/Run2016B-HighMET-07Aug17_ver2-v1/RAW-RECO
/MET/Run2016C-HighMET-07Aug17-v1/RAW-RECO
/MET/Run2016D-HighMET-07Aug17-v1/RAW-RECO
/MET/Run2016E-HighMET-07Aug17-v1/RAW-RECO
/MET/Run2016F-HighMET-07Aug17-v1/RAW-RECO
/MET/Run2016G-HighMET-07Aug17-v1/RAW-RECO
/MET/Run2016H-HighMET-07Aug17-v1/RAW-RECO
/MET/Run2018A-HighMET-17Sep2018-v1/RAW-RECO
/MET/Run2018B-HighMET-17Sep2018-v1/RAW-RECO
/MET/Run2018C-HighMET-17Sep2018-v1/RAW-RECO
/MET/Run2018D-HighMET-PromptRECO-v1/RAW-RECO
/MET/Run2018D-HighMET-PromptRECO-v2/RAW-RECO
/MET/Run2017B-HighMET-17Nov2017-v1/RAW-RECO
/MET/Run2017C-HighMET-17Nov2017-v1/RAW-RECO
/MET/Run2017D-HighMET-17Nov2017-v1/RAW-RECO
/MET/Run2017E-HighMET-17Nov2017-v1/RAW-RECO
/MET/Run2017F-HighMET-17Nov2017-v1/RAW-RECO
```

136 **3.2 Signal simulation**

137 The first model used for the interpretation is the Twin Higgs model, where a Higgs boson
 138 decays to two long-lived scalars which then decay back to Standard Model particles. This
 139 model has been interpreted in several previous searches because it produces neutral long-lived
 140 particles and is not as significantly constrained as models with colored top partners. Only
 141 the MC samples for the gluon production channel and 4b final state of the Higgs boson were
 142 used for the optimization of the analysis, but the final interpretation of the results includes the
 143 additional contributions from other Higgs boson production modes and other final states. The
 144 gluon fusion and vector boson fusion samples, which are centrally produced, are normalized

145 with the 48.58 pb NNNLO and 3.78 pb NNLO cross sections respectively, both provided by the
 146 LHC Higgs Cross Section working group. The gluon fusion samples include 4b, 4d, and 4 τ
 147 final states, while the vector boson fusion samples only include 4b and 4 τ . The signal samples
 148 cover long-lived particle masses of 7 (4d and 4 τ only), 15, 40, and 55 GeV and proper lifetimes
 149 of 0.001, 0.01, 0.1, 1, 10, and 100m.

150 Private samples are used to include the contributions from VBF (4d), WH, ZH, and ttH pro-
 151 duction modes. The private samples were generated using the same gridpacks as the official
 152 Higgs samples. These cover the same final states and LLP masses as the central samples, and
 153 proper lifetimes of 0.1, 1, 10, and 100m. The cross sections used are the NNLO values from the
 154 LHC Higgs Cross Section working group.

155 The complete set of signal simulations available are listed in Table 2 and Table 3, and Figure 1
 156 shows a Feynman diagram for this model.

Table 2: List of centrally produced Twin Higgs signal simulations used in this analysis.

Samples	σ (pb)
/ggH_HToSSTobbbb_MH-125_Tune*_*13TeV-powheg-pythia8/*/GEN-SIM-RECO	48.58
/VBFH_HToSSTo4b_MH-125_Tune*_*13TeV-powheg-pythia8/*/GEN-SIM-RECO	3.782
/ggH_HToSSTodddd_MH-125_Tune*_*13TeV-powheg-pythia8/*/GEN-SIM-RECO	48.58
/ggH_HToSSTo4Tau_MH-125_Tune*_*13TeV-powheg-pythia8/*/GEN-SIM-RECO	48.58
/VBFH_HToSSTo4Tau_MH-125_Tune*_*13TeV-powheg-pythia8/*/GEN-SIM-RECO	3.782

Table 3: List of privately produced Twin Higgs signal simulations used in this analysis.

Samples	σ (pb)
/VBFH_HToSS_STodd_ms*_pl*	3.782
/WminusH_HToSS_STo*_*ms*_pl*	0.5328
/WplusH_HToSS_STo*_*ms*_pl*	0.8400
/ZH_HToSS_STo*_*ms*_pl*	0.7612
/ttH_HToSS_STo*_*ms*_pl*	0.5071

157 The second model used for the interpretation is the Dark Shower model [10], where a Higgs bo-
 158 son decays to two dark sector quarks which hadronize into lighter dark sector particles forming
 159 a “dark shower” that includes particles that eventually decay back to Standard Model particles.
 160 Such dark sector models are motivated by a range of mysteries in particle physics, including the
 161 stability of the electroweak hierarchy, dark matter, and the antimatter/matter asymmetry [1].
 162 However, the signature produced by such a dark shower can be highly challenging to simulate
 163 due to the model dependence in the properties of the new states being produced and the diffi-
 164 culty in predicting the dynamics of the dark sector (particularly for incalculable hadronization
 165 processes). To circumvent these issues, Ref. [10] describes a set of benchmark models where the
 166 dark sector is reduced to a single dark quark, vector meson, and scalar meson, and the number
 167 of dark QCD colors is taken as 3. Various portals through which the dark sector decays to the
 168 standard model are then considered. In the case that the decay occurs via a vector portal, the
 169 dark vector meson couples to the Standard Model and the dark scalar meson is invisible. For

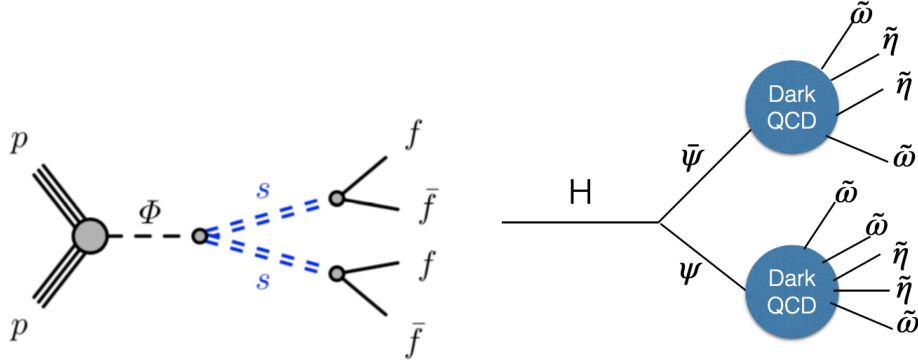


Figure 1: Example diagrams for the two signal models used for interpretation. The left diagram shows the Higgs boson decaying to two long-lived scalars which then decay back to Standard Model fermions. The right diagram shows the Higgs boson decaying to two dark sector quarks which hadronize and form a dark shower, which depending on the portal and mass hierarchy can contain dark sector mesons that decay back to Standard Model particles.

- 170 all other portals, the dark scalar meson couples to the Standard Model and the dark vector me-
 171 son is invisible. In the case of the dark photon portal, the dark scalar meson promptly decays
 172 to two intermediate vector mediators (with a mass taken to be 0.4 times the mass of the dark
 173 scalar meson) that then undergo displaced decays back to the standard model. There are there-
 174 fore double the number of displaced decays for this portal. Figure 1 illustrates the Higgs decay
 175 and dark shower formation.
 176 Unlike the Twin Higgs model, there are no centrally produced simulations of this Dark Shower
 177 model, so samples were privately produced for various decay portals from the dark sector
 178 to the Standard Model as well as various parameters of the long-lived particle. The private
 179 samples were generated using the same gridpacks as the official Higgs samples. The simulation
 180 included a filter that required the Higgs boson had $p_T > 140 \text{ GeV}$. This filter is very efficient
 181 after the $E_T^{\text{miss}} > 200 \text{ GeV}$ requirement detailed in Section 4 and Section 6, as seen in Figure 2.
 182 Each of the portals tested had higher than 99% efficiency for this filter. The plot shows one
 183 choice of model parameters, but similar results were seen for all models tested.

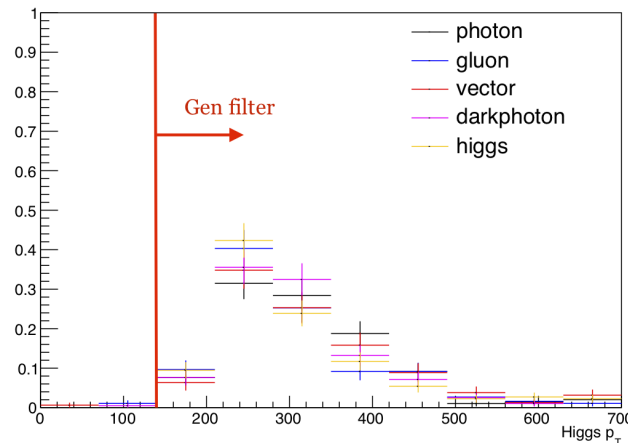


Figure 2: Higgs boson p_T distributions for various Dark Shower portals with a long-lived par-
 ticle with mass 10 GeV, proper lifetime 1 meter, and energy scale ratios $x_{i\omega} = x_{i\Lambda} = 1$, with a
 $E_T^{\text{miss}} > 200 \text{ GeV}$ cut applied. In this high E_T^{miss} selection, the p_T filter is nearly 100% efficient.

184 The samples cover proper lifetimes of 0.5, 1, 5, and 10m. The long-lived particle masses simu-
 185 lated for each decay portal are different because of different theoretically motivated minimums.
 186 The final parameters are $x_{i\omega}$, the ratio of the dark vector meson mass to the dark scalar meson
 187 mass, and $x_{i\Lambda}$, the ratio of the dark scalar meson mass to the dark sector QCD scale Λ . If
 188 the mass of the vector meson is greater than twice the mass of the scalar meson, it will decay
 189 promptly into scalar mesons, but the more massive vector meson can only be produced if its
 190 mass is below the dark QCD scale Λ , i.e. if $x_{i\omega} \leq x_{i\Lambda}$. Since the scalar meson does not couple
 191 to the Standard Model for the vector portal, the shower will be entirely invisible if the vector
 192 meson can decay to two scalar mesons, but for all other portals the visible content is increased
 193 because the scalar mesons do couple to the Standard Model. Three scenarios were simulated
 194 for each decay portal. In the first case, $x_{i\omega} = x_{i\Lambda} = 1$. In this scenario, both vector and scalar
 195 mesons are produced, and the shower is semi-invisible for all portals since only one of the par-
 196 ticles couples to the Standard Model. In the second case $x_{i\omega} = 2.5$ and $x_{i\Lambda} = 1$, so only scalar
 197 mesons are produced, which means the shower is fully visible (except for the vector portal
 198 where the scalar does not couple to the Standard Model). In the final case $x_{i\omega} = x_{i\Lambda} = 2.5$, so
 199 both mesons are produced and the vector can decay to two scalar mesons. Since the scalars are
 200 visible (except for vector portal), this case has a high multiplicity of visible decays. Since the
 201 showers are invisible for the vector portal whenever $x_{i\omega} > 2$, only the first scenario is simulated
 202 for that portal. The simulated parameters for each decay portal are summarized in Table 4. The
 203 visible content of the jet is summarized in the last column.

Table 4: Summary of privately produced Dark Shower signal simulations used in this analysis.

Decay portal	LLP masses [GeV]	LLP lifetimes [m]	$(x_{i\omega}, x_{i\Lambda})$	Features
Gluon	3, 5, 10, 15, 20	0.5, 1, 5, 10	(1.0,1.0), (2.5,1.0), (2.5,2.5)	hadron-rich shower
Photon	2, 5, 10, 15, 20	0.5, 1, 5, 10	(1.0,1.0), (2.5,1.0), (2.5,2.5)	photon shower
Vector	2, 5, 10, 15, 20	0.5, 1, 5, 10	(1.0,1.0)	semi-visible jet
Higgs	4, 5, 10, 15, 20	0.5, 1, 5, 10	(1.0,1.0), (2.5,1.0), (2.5,2.5)	heavy flavor-rich shower
Dark photon	2, 5, 10, 15, 20	0.5, 1, 5, 10	(1.0,1.0), (2.5,1.0), (2.5,2.5)	lepton-rich shower

204 Appendix A includes some of the key MC generator-level distributions of the LLP decay and
 205 shower for each of the different model portals and parameters. A request has been made for a
 206 central MC production for a small subset of these samples to use for validation, and the note
 207 will be updated with the results of the validation when the central samples are available.

208 4 Trigger strategy

209 For cases where the long-lived particle lifetime is long enough that it decays in the muon system
 210 or outside CMS, there will be a momentum imbalance possibly giving large E_T^{miss} in the event.
 211 If the Higgs boson recoils against initial state radiation (ISR) so that the entire Higgs system is
 212 boosted there will be significant E_T^{miss} pointing opposite the ISR jet. This analysis pursues these
 213 types of events by using the E_T^{miss} -based triggers, summarized in Table 5.

Table 5: Trigger paths used in this analysis.

Year	Trigger path
2016	HLT_PFMET120_PFMHT120_IDTight OR HLT_PFMETNoMu120_PFMHTNoMu120_IDTight
2017	HLT_PFMET120_PFMHT120_IDTight OR HLT_PFMETNoMu120_PFMHTNoMu120_IDTight OR HLT_PFMET140_PFMHT140_IDTight OR HLT_PFMETNoMu140_PFMHTNoMu140_IDTight OR HLT_PFMET120_PFMHT120_IDTight_PFHT60 OR HLT_PFMETNoMu120_PFMHTNoMu120_IDTight_PFHT60
2018	HLT_PFMET120_PFMHT120_IDTight OR HLT_PFMETNoMu120_PFMHTNoMu120_IDTight OR HLT_PFMET140_PFMHT140_IDTight OR HLT_PFMETNoMu140_PFMHTNoMu140_IDTight OR HLT_PFMET120_PFMHT120_IDTight_PFHT60 OR HLT_PFMETNoMu120_PFMHTNoMu120_IDTight_PFHT60

214 An additional offline $E_T^{\text{miss}} > 200 \text{ GeV}$ requirement is made, since the E_T^{miss} -skimmed RECO
 215 datasets make this cut. As shown in Section 4.1, this cut is in the plateau region of the trigger.

216 4.1 Trigger efficiency

217 The trigger efficiency is measured in data and MC using the WJetsToLNu dataset. Events
 218 are required to contain exactly one muon that passes loose identification requirements and
 219 has $30 < p_T < 100 \text{ GeV}$. The efficiency is measured for events that pass the HLT_IsoMu27
 220 trigger and as a function of the $E_T^{\text{miss}}_{\text{noMu}}$, the remaining missing momentum after the muon
 221 momentum has been added back in to the E_T^{miss} , in the event. The data and MC agree within
 222 about 5% with no significant difference seen between the years (see Figure 3).

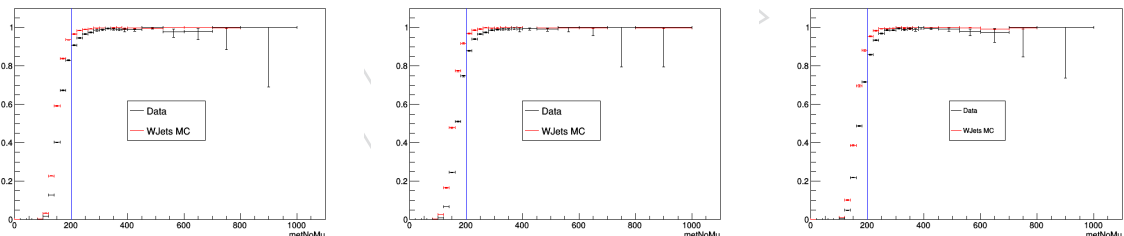


Figure 3: Comparison of trigger efficiency in data and MC for 2016 (left), 2017 (middle), and 2018 (right) using a single muon selection of WJetsToLNu dataset. Overall, there is about a 5% difference between data and MC, across all three years.

223 These trigger efficiency studies are done using a single muon AOD dataset with minimal re-
 224 quirements on the muon, while signal events have clusters in the muon system in addition to
 225 the missing transverse momentum. Since DT rechit information (and therefore DT clusters)
 226 is not available in AOD, the previous study cannot ensure that the trigger efficiency is well-
 227 modeled in MC when there is a large cluster of hits in the muon system, which could affect
 228 the E_T^{miss} and therefore the trigger. Another test can be done using the 2017 ZToMuMu data
 229 RECO dataset used for modeling of key cluster variables in Section 8. Figure 4 shows the same
 230 trigger efficiency plot, comparing events with no cluster requirement to those with at least one
 231 DT cluster. No difference is seen when events are required to have a DT cluster.

232 The difference between MC modeling of the trigger efficiency and the measured efficiency in
 233 data can be measured by studying WJetsToLNu AOD datasets. The 2017 ZToMuMu RECO

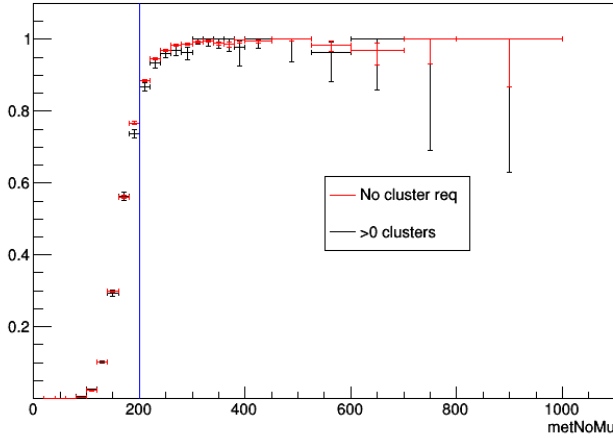


Figure 4: Comparison of trigger efficiency for events with a DT cluster to those with no cluster requirement in a 2017 ZToMuMu dataset with single muon requirements made to match the WJetsToLNu trigger efficiency study. No significant difference is measured between all events and those with a DT cluster.

dataset confirms that the efficiency in data does not change when there is a cluster in the DT system, so the comparison made without cluster information can be applied to the events selected in this analysis. This comparison showed that the MC trigger efficiency is higher than the efficiency in data, so a year- and E_T^{miss} -dependent correction factor, which ranges from 0.95 to 1, is applied to all MC.

239 5 Physics objects

240 The definitions of physics objects used in the analysis are given below.

241 5.1 DT rechits

242 5.1.1 Barrel Muon System

243 The Muon Barrel System (see Figure 5) consists of 5 wheels separated in the z direction, each
 244 about 2.5m long. Each wheel is divided into 4 stations in the radial direction, separated by the
 245 steel flux-return yoke, and each station is made up of 12 chambers in the ϕ direction. The first 3
 246 stations, MB1-3, are made up of three superlayers, each made up of 4 layers of drift tubes. Two
 247 of these measure position in the bending $R - \phi$ plane and the third measures position in the
 248 longitudinal R-theta plane. MB4 only has the two $R - \phi$ superlayers. MB1-2 have two layers
 249 of RPCs, one on the inner radius of the DTs and one on the outer radius. MB3-4 both have just
 250 one layer on the outer radius. The RPCs only measure position in the bending plane.

251 The precise position of the DT hit is obtained from fitting to a muon segment made of several
 252 DT rechits. Until the segment is made, there is an ambiguity about which side of the wire
 253 the hit occurred on, since all that is known is the drift time. In the RECO format used for the
 254 analysis because of this position ambiguity the hits are all assumed to be at the center of the
 255 drift tube, and similarly the RPC rechits are positioned at the center of the chamber.

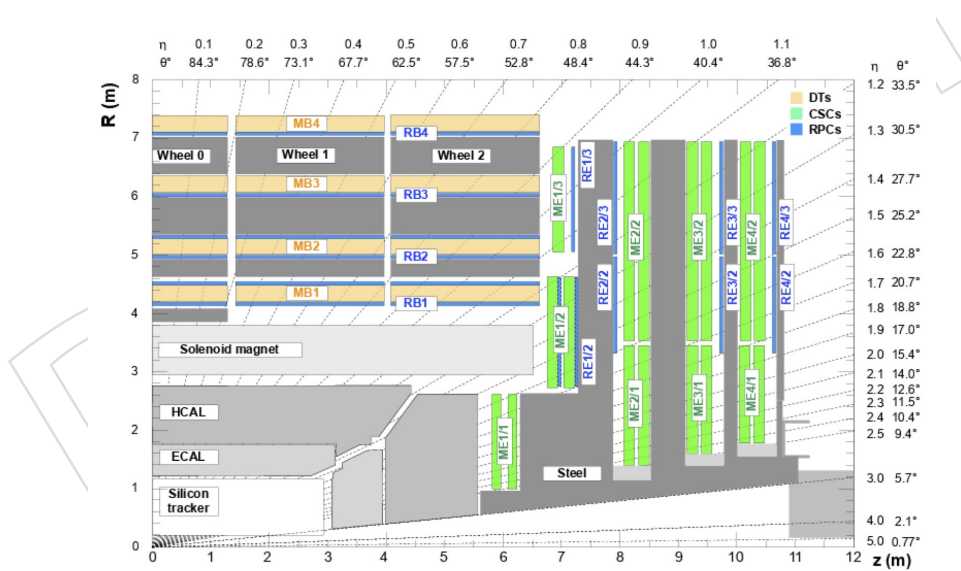


Figure 5: Diagram showing the geometry of CMS and the Muon System in the $R - z$ plane.

256 5.1.2 DT rechit clusters

257 As the LLP decays back to the SM, all the charged particles can interact with the gas within
 258 the DTs, producing hits. While a single muon typically produces one hit per DT layer, giving
 259 a total of 8 or 12 hits per station, the LLP decay can produce showers of particles which all
 260 produce hits, resulting in many more hits than a single muon. Additionally, the decay products
 261 can travel in any direction, so the hits associated with one decay product are not necessarily
 262 consistent with a path from the interaction point. Because of this and the overall large number

263 of hits present, the muon track reconstruction is not effective. Instead, the hits are combined
 264 into clusters rather than tracks.

265 DT rechits are clustered using their η and ϕ position according to the Density-based spatial
 266 clustering of applications with noise (DBSCAN) algorithm, with a distance parameter $\Delta R = 0.2$
 267 and a minimum of 50 rechits per cluster. The cluster reconstruction efficiency as a function of
 268 LLP decay radius and z position for Twin Higgs signal models are shown in Figure 6 and
 269 Figure 7. Efficiency is higher when the LLP decay occurs at lower radius, as there are more
 270 DT chambers for the decay products to give hits in and cause a cluster, compared to decays at
 271 higher radius where there are fewer stations the decay products can interact with. Efficiency is
 272 fairly constant as a function of z decay position, but there are dips between wheels and at the
 273 edge of the barrel.

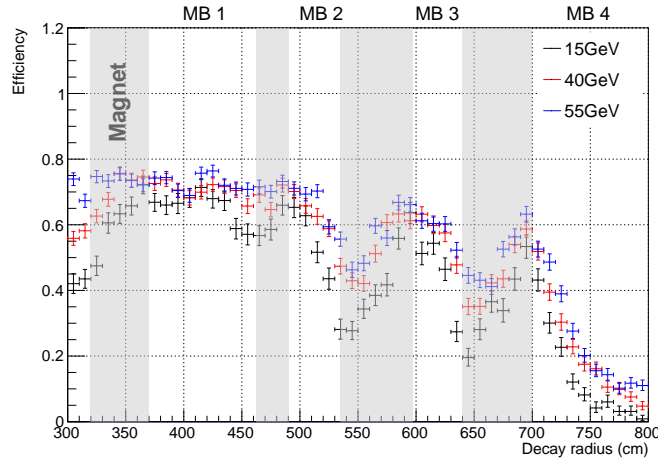


Figure 6: Cluster reconstruction efficiency for Twin Higgs signal models as a function of detector radius where LLP decays. Efficiency slowly decreases with increasing radius, as there is less detector material for the cluster of hits from the decay to form in after the LLP travels through one or more MB stations.

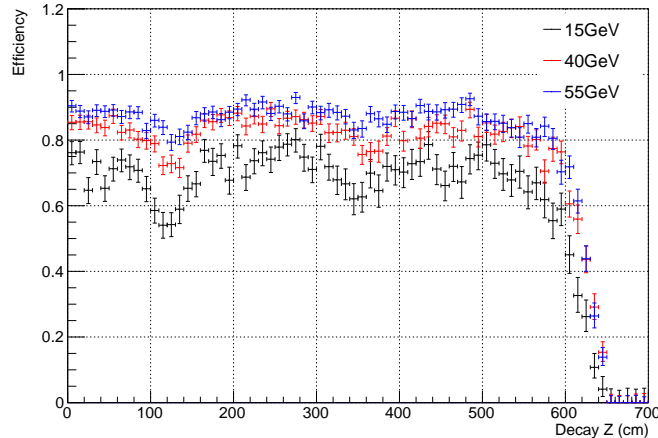


Figure 7: Cluster reconstruction efficiency for Twin Higgs signal models as a function of detector z position where LLP decays. Efficiency is constant across z , except for dips between MB wheels and a lower efficiency when the decay happens at the edge of the detector barrel.

274 Due to the rechits being positioned at the center of the DTs, clusters tend to be fairly localized in

275 η . Figure 8 shows the η and ϕ spread of the clusters. Signal and background clusters generally
 276 have similar spreads. Figure 9 shows the z position of clusters, defined as the average z position
 277 of all clustered rechits. The center of clusters tends to be at the center of MB wheels, except
 278 for some rare instances toward higher η when clusters are made from hits in two wheels and
 279 centered between the wheels.

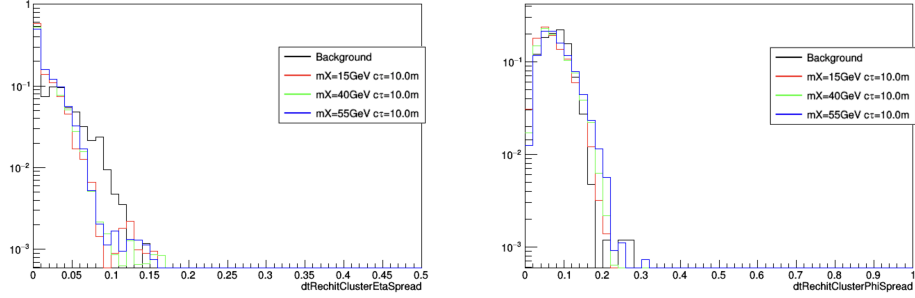


Figure 8: Spread of clustered DT rechits in η (left) and ϕ (right) for Twin Higgs signal models and background measured in a control region defined by inverting $|\Delta\phi(jet, \vec{E}_T^{\text{miss}})|$ cut.

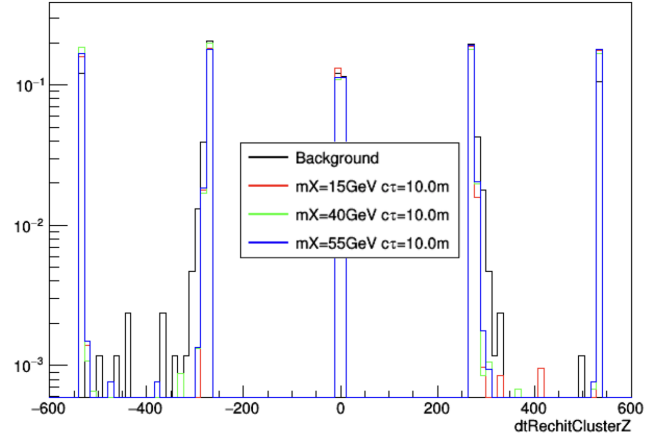


Figure 9: Cluster z position for Twin Higgs signal models and background measured in a control region defined by inverting $|\Delta\phi(jet, \vec{E}_T^{\text{miss}})|$ cut. Clusters are almost all centered at the center of MB wheels, except for a very small fraction spread across 2 higher z wheels.

280 The minimum cluster size threshold is greater than the 44 expected hits from a muon passing
 281 through the Barrel Muon System and generating one hit for each DT layer. Most signal clusters
 282 contain more than 50 rechits, so a tighter cluster size requirement is used to define the signal
 283 region, while the smaller clusters can be used as a control sample. This cut and other cluster
 284 requirements are discussed further in Section 6.

285 5.2 Jets

286 Jets are defined as sets of reconstructed PF candidates [12] clustered with the anti- k_T jet clustering
 287 algorithm. Jet energy corrections are then applied to all jets. Only jets with $|\eta| < 2.4$ are
 288 considered, and there must be at least one jet with $p_T > 30$ GeV that passes the loose jet ID
 289 criteria since signal events will contain an ISR jet that the Higgs boson recoils against. Other
 290 jets with $p_T > 10$ GeV that do not necessarily pass jet ID criteria are still considered for the jet
 291 veto described in Section 6.

292 5.3 Muons

293 Muon objects are reconstructed with the standard muon reconstruction, which finds aligned
 294 hits in the muon system, uses them to build track segments, and finally reconstructs a muon
 295 trajectory by performing a fit with the track segments and hits in the Tracker. Muons with
 296 $p_T > 10 \text{ GeV}$, $|\eta| < 2.4$, and passing the Muon POG loose identification requirements are used
 297 for a muon veto. These muons are reconstructed either as a global-muon or as an arbitrated
 298 tracker-muon.

299 5.4 Missing transverse momentum

300 The \vec{E}_T^{miss} in an event is the negative vector sum of the transverse momentum of all PF candidates
 301 and the magnitude is the E_T^{miss} . The \vec{E}_T^{miss} used in this analysis is the Type-I Corrected
 302 PFMET, which propagates the jet energy corrections to the \vec{E}_T^{miss} by replacing individual jet
 303 constituents in the vector sum with the energy-corrected jets.

304 The xy-Shift correction, which reduces the ϕ modulation and mitigates pile-up effects, is also
 305 applied to the \vec{E}_T^{miss} . The effect of the xy-Shift is small for the $E_T^{\text{miss}} > 200 \text{ GeV}$ events used in
 306 this analysis. There is also a correction to address an issue that causes EE towers to be noisy in
 307 2017 data. To address this, jets with p_T (raw) $< 50 \text{ GeV}$ and $2.65 < |\eta| < 3.139$ are not included
 308 in the \vec{E}_T^{miss} calculation.

309 Additionally, filters are applied to both data and MC to remove fake E_T^{miss} due to non-collision
 310 sources such as noise, cosmic showers, or beam-halo. The filters applied are given in Table 6.

Table 6: List of E_T^{miss} filters used in the analysis.

Filter	Years	Applied to data	Applied to MC
primary vertex filter	2016, 2017, and 2018	Yes	Yes
beam halo filter	2016, 2017, and 2018	Yes	Yes
HBHE noise filter	2016, 2017, and 2018	Yes	Yes
HBHEiso noise filter	2016, 2017, and 2018	Yes	Yes
ECAL TP filter	2016, 2017, and 2018	Yes	Yes
Bad PF Muon Filter	2016, 2017, and 2018	Yes	Yes
ee badSC noise filter	2016, 2017, and 2018	Yes	No
ECAL bad calibration filter	2017 and 2018	Yes	Yes

311 6 Event selection

312 The major backgrounds for this signature and the variables used to reject those backgrounds are
 313 discussed in this section. Several event-level selections are made based on the type of signal
 314 event that could pass the trigger. A $E_T^{\text{miss}} > 200 \text{ GeV}$ requirement is made to be consistent
 315 with the RECO datasets. For signal events with high E_T^{miss} , the Higgs system is assumed to
 316 be recoiling against an ISR jet. Because of this, events are required to have at least one jet
 317 with $p_T > 30 \text{ GeV}$ and $|\eta| < 2.4$ and the leading p_T jet in the event must pass loose jet ID
 318 criteria. The 30 GeV requirement is fairly loose for signal events, however a lower threshold
 319 allows for model independence while the E_T^{miss} cut indirectly forces the event to have high
 320 ISR. Minimizing over all $p_T > 30 \text{ GeV}$ jets, the minimum $|\Delta\phi(\text{jet}, \vec{E}_T^{\text{miss}})|$ must be greater than
 321 0.6. Together, these jet and E_T^{miss} requirements select a signal-like event with a well-measured
 322 jet and a lot of E_T^{miss} that is not aligned with any jets, since signal should be invisible to the
 323 detector until the decay in the muon system. Finally, to select signal events with decays in
 324 the muon system, the event must contain at least one cluster of DT rechits, as described in
 325 Section 5.1.2.

326 The several types of background after these event-level requirements will be discussed as well
 327 as the other event and cluster selections used to reject these backgrounds. Plots will be shown
 328 illustrating the difference between signal and background for these variables measured in con-
 329 trol samples defined by inverting other variables.

330 6.1 Control regions

331 As described in the previous section, signal events need high p_T ISR in order to pass the E_T^{miss}
 332 trigger, which leads to a back-to-back jet and \vec{E}_T^{miss} . Figure 10 shows signal and background
 333 $|\Delta\phi(\text{jet}, \vec{E}_T^{\text{miss}})|$ distributions for events with $E_T^{\text{miss}} > 200 \text{ GeV}$. Because there is a large peak in
 334 background near 0 and most signal peaks near π , the events in the < 0.6 region are used as a
 335 background control sample.

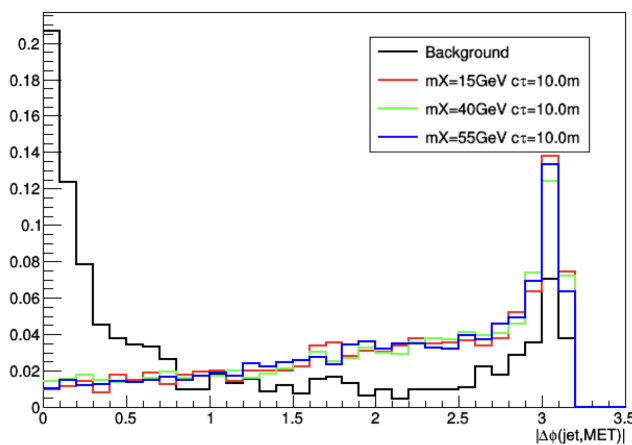


Figure 10: Signal and background distributions showing the minimum $|\Delta\phi(\text{jet}, \vec{E}_T^{\text{miss}})|$ in the event. The signal peaks near π , while there is a large background peak near 0. The low $\Delta\phi$ region can be used as a background control sample.

336 Because the LLP decay in signal causes both the E_T^{miss} and the cluster, they tend to be aligned
 337 in ϕ . Background clusters are not generally correlated with the E_T^{miss} so the distribution of
 338 angle between clusters and \vec{E}_T^{miss} is flat, as seen in Figure 11. Clusters > 1.0 can be used as a

339 background control sample.

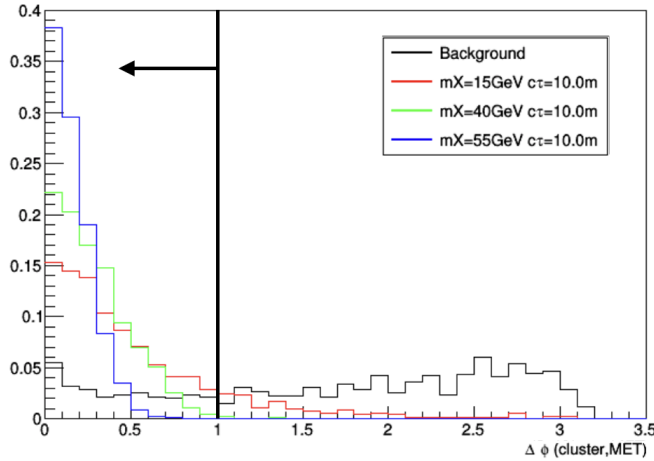


Figure 11: Signal and background distributions showing $|\Delta\phi(\text{cluster}, \vec{E}_T^{\text{miss}})|$. Background is measured in the low $|\Delta\phi(\text{jet}, \vec{E}_T^{\text{miss}})|$ region. The signal distribution peaks near 0, while background is flat. The high $\Delta\phi$ region can be used as a background control sample.

340 Background clusters often come from physics originating at the interaction point, while the
 341 signal signature includes a shower in the muon system with no corresponding physics in the
 342 inner parts of the detector. Because of this, requiring that clusters are associated with objects
 343 at a smaller radius results in a background-enriched control sample crucial for studying these
 344 types of background clusters.

345 6.2 Background sources

346 The dominant backgrounds after these event-level requirements are described below.

- 347 • Punch-through jets: The shower from a jet may continue through the magnet and
 348 into the Barrel Muon System, giving a cluster of hits in the DTs
- 349 • Primary vertex muons: A muon from the interaction point may produce a bremsstrahlung
 350 photon which produces a cluster of hits in the DTs
- 351 • Cosmic muons: Cosmic muons can undergo bremsstrahlung to leave hits in the DTs
 352 or may be part of a large cosmic shower with many particles able to produce hits
- 353 • Noise: There could be a noise event in part of the muon system which looks like a
 354 signal cluster
- 355 • Pileup: An event may have a cluster and event properties that appear signal-like
 356 because of pileup effects

357 6.3 Cluster vetoes

358 Signal clusters in the muon system will not be associated with any physics objects in inner parts
 359 of the detector, while backgrounds such as punch-through jets and muons will be. Therefore,
 360 a cluster is vetoed if it is within $\Delta R < 0.4$ of any jets with $p_T > 10 \text{ GeV}$ or muons with $p_T >$
 361 10 GeV that pass loose identification requirements. Figure 12 and Figure 13 show the p_T of
 362 any matched jets and muons, respectively, for signal and background. The jet veto threshold is
 363 made as low as possible to reject as much of the background as possible that leaves hits in the
 364 calorimeters, but signal efficiency remains high even using 10 GeV jets for the veto. Conversely,

365 signal efficiency is sensitive to the requirements placed on the muons used to veto clusters. Due
 366 to low-quality muons that can be reconstructed from DT rechits from the long-lived particle
 367 decay which can in turn veto signal clusters, only muons that pass loose identification are
 368 used.

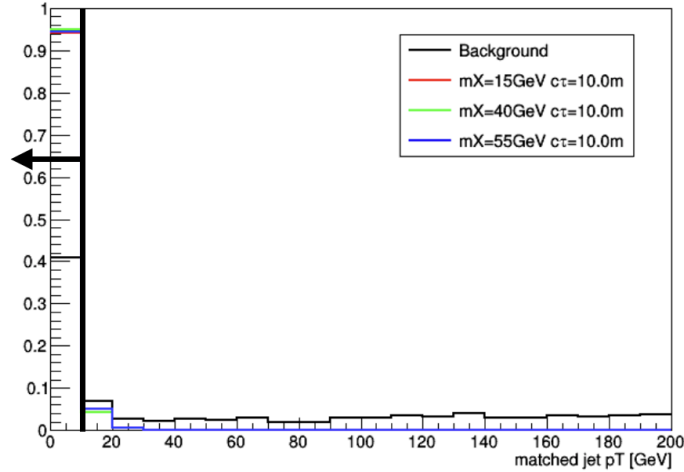


Figure 12: Signal and background distributions showing the maximum p_T of jets within $\Delta R < 0.4$ of the cluster. The background is in a control region selected by inverting the $|\Delta\phi(\text{cluster}, \vec{E}_T^{\text{miss}})|$ cut. The MB1 veto is applied. If no jets are matched to the cluster then the entry is 0.

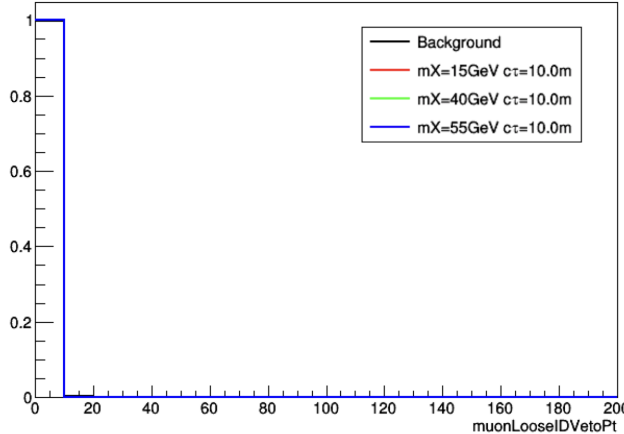


Figure 13: Signal and background distributions showing the maximum p_T of loose ID muons within $\Delta R < 0.4$ of the cluster. The background is measured in a control region selected by inverting the $|\Delta\phi(\text{cluster}, \vec{E}_T^{\text{miss}})|$ cut. If no muons are matched to the cluster then the entry is 0. After the jet and MB1 vetoes are applied, the efficiency is nearly 100% for both signal and background.

369 In addition to the jet veto using a $\Delta R < 0.4$ cone, a veto is made using the leading p_T jet
 370 and a larger cone. The smaller cone does not completely remove clusters resulting from the
 371 leading jet, as shown in Figure 14. The distribution of ΔR between the leading jet and cluster
 372 shows a large amount of background just outside the matching cone. Therefore, clusters within
 373 $\Delta R < 1.2$ are vetoed. The large cone removes all clusters originating from the leading jet. This

374 larger cone veto is not applied to all jets because the probability of randomly matching to a low
 375 p_T jet from noise or pileup within the large cone would lead to large signal inefficiency. Since
 376 the leading jet in signal events is the ISR that the signal system recoils against, signal efficiency
 377 for this leading jet veto is nearly 100%.

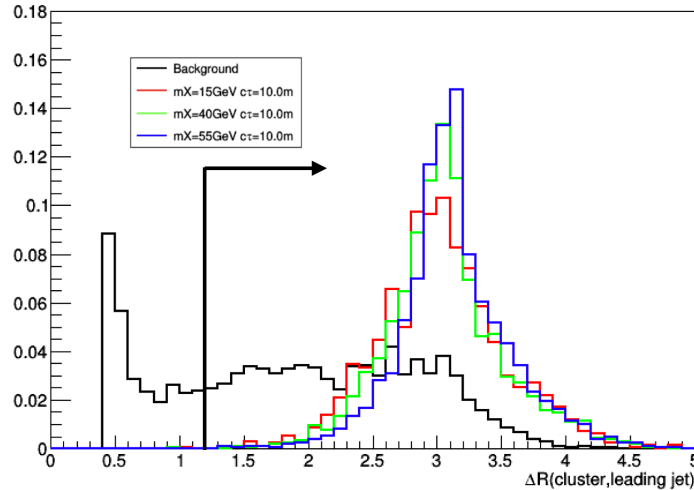


Figure 14: Signal and background distributions showing $\Delta R(\text{cluster}, \text{leading } p_T \text{ jet})$. The background is in a control region selected by inverting the MB1 veto. Clusters that match to any jet with $p_T > 10 \text{ GeV}$ with $\Delta R < 0.4$ are vetoed.

378 To further suppress background, clusters are also vetoed if they are associated with hits in
 379 stations at a smaller radius than the cluster. Clusters from punch-through or muons will most
 380 likely cause hits in the innermost DT station, MB1, even when the cluster forms at a larger
 381 radius. Similarly, clusters in MB3 or MB4 will also have hits in MB2. Conversely, a long-
 382 lived particle can travel through multiple stations leaving no hits before decaying in one of the
 383 outer stations. The difference between signal and background is illustrated in Figure 15 and
 384 Figure 16.

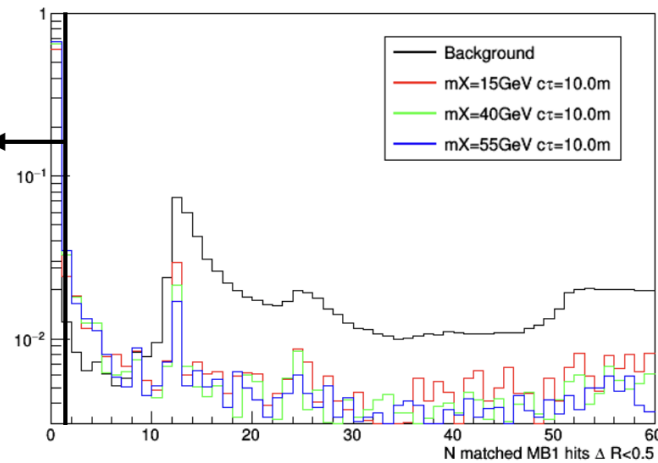


Figure 15: Signal and background distributions showing the number of MB1 rechits within $\Delta R < 0.4$ of the cluster. The background is measured in a control region selected by inverting the $|\Delta\phi(\text{cluster}, \vec{E}_T^{\text{miss}})|$ cut. The peak at 12 hits corresponds to 1 hit per DT layer in MB1, as expected for muon backgrounds.

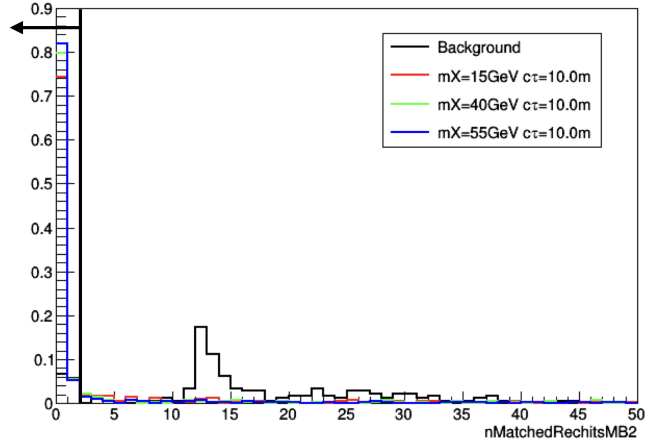


Figure 16: Signal and background distributions showing the number of MB2 rechits within $\Delta R < 0.4$ of the cluster. The background is measured in a control region selected by inverting the $|\Delta\phi(\text{cluster}, \vec{E}_T^{\text{miss}})|$ cut. The peak at 12 hits corresponds to 1 hit per DT layer in MB2, as expected for muon backgrounds.

385 Any cluster that is matched to more than 1 hit in MB1 within $\Delta < 0.4$ is vetoed. Additionally,
 386 clusters made up of more hits in MB3 or MB4 than MB2 are vetoed if there is more than 1 hit in
 387 MB2 within $\Delta R < 0.4$. If the cluster is mostly made up of MB2 hits, the MB2 veto is not applied,
 388 while the MB1 veto is always applied. Because of this cut, only events where the shower from
 389 the long-lived particle decay occurs in the outer three stations, MB2-4, are included in the signal
 390 region. Limiting the search to the three outer MB stations reduces the sensitivity to models with
 391 shorter lifetimes, however those models are better covered by other analyses.

392 It is possible for some backgrounds, such as cosmic muons, to produce a cluster in MB2-4
 393 without having matching hits in MB1 or clusters in MB3-4 without hits in MB1 or MB2. For
 394 cosmic muons with a trajectory not through the IP, the associated hits in inner stations may
 395 be at a much different η so would not be vetoed with the ΔR match described previously. An
 396 example of such an event is shown in Figure 17. The yellow dots are DT rechits, the purple
 397 elements correspond to RPC rechits, and the muons are the thin red lines. Tracker tracks are
 398 not drawn to make making and interpreting the event displays easier. The $R - \phi$ view on the
 399 left shows the cluster in MB4 with a clear line of DT rechits aligned in ϕ in the inner stations.
 400 The $R - z$ view on the right, however, shows the the hits do not point back to the interaction
 401 point. They are more consistent with a cosmic muon traveling through the detector passing
 402 from the middle wheel (where the cluster is located along with many RPC hits) to the adjacent
 403 wheel. The muon reconstructed also does not point to the cluster so cannot veto it.

404 To reject these types of events, additional vetoes are applied to clusters that have more than 8
 405 hits in the MB1 stations in adjacent wheels within $\Delta\phi < \pi/4$ or clusters in MB3-4 that have
 406 more than 8 hits in the MB2 stations in adjacent wheels within $\Delta\phi < \pi/4$. The expected
 407 number of hits for a muon in one station is 12, so this veto can reject cosmic muon clusters
 408 while also having a high threshold so that signal clusters are not accidentally vetoed by noise
 409 (see Figure 18).

410 6.4 RPC matching

411 In addition to the DT hits that are clustered, hits in the Resistive Plate Chambers (RPCs) in the
 412 Barrel Muon System can also be used to discriminate signal from background. Each DT station

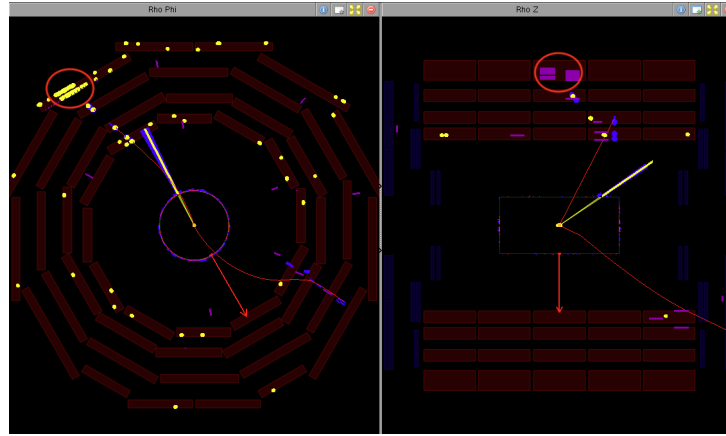


Figure 17: Example event display showing the type of cosmic muon event that can pass the standard MB1 veto. Tracker tracks are not drawn to make making and interpreting the event displays easier.

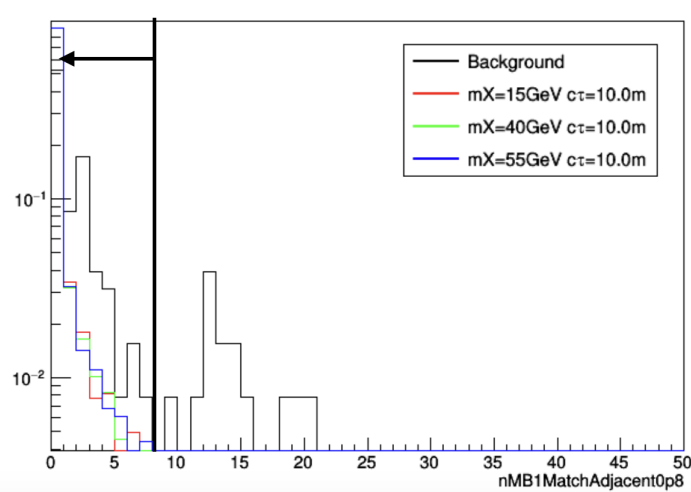


Figure 18: Signal and background distributions showing the number of MB1 rechits from wheels adjacent to the cluster wheel within $\Delta\phi < \pi/4$ of the cluster. The background is measured in a control region selected by inverting the $|\Delta\phi(\text{cluster}, \vec{E}_T^{\text{miss}})|$ cut. The $\Delta R < 0.4$ MB1 veto is already applied for these events.

413 is bordered by at least one RPC layer so real showers should give hits in DTs and RPCs. Noise
 414 that affects just the DTs giving a cluster of fake hits can be rejected by requiring that the cluster
 415 is matched to at least one RPC rehit. An RPC rehit is matched to a cluster if they are from the
 416 same Muon System wheel and within $\Delta\phi < 0.5$. The matching was chosen to give nearly 100%
 417 efficiency for signal as shown in Figure 20 and Figure 21.

418 6.5 Overall detector activity

419 Showers from the long-lived particle decays are mostly contained within one or two DT cham-
 420 bers, however cosmic showers may produce hits over the entire muon system which can then
 421 be clustered into large signal-like clusters (see Figure 22).

422 Previously a selection on the total number of rechits across the detector was used to veto cosmic
 423 showers, but this was found to be too susceptible to noise fluctuations, giving potentially large
 424 inefficiency for signal events. Instead, these shower events are rejected by using the presence of

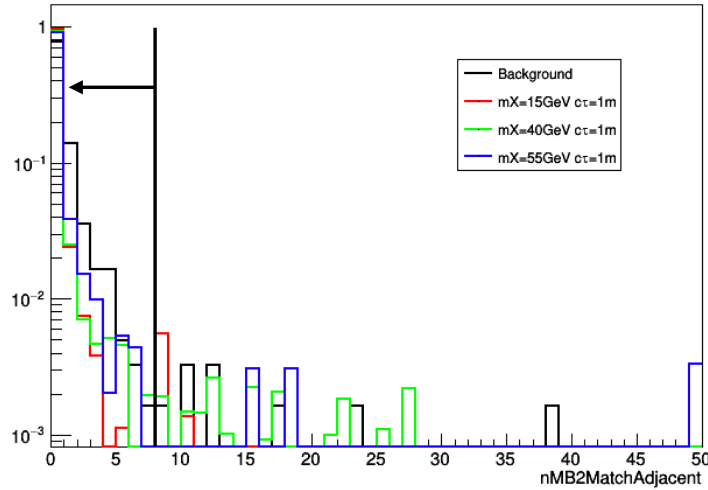


Figure 19: Signal and background distributions showing the number of MB2 rechits from wheels adjacent to the cluster wheel within $\Delta\phi < \pi/4$ of the cluster. The background is measured in a control region selected by inverting the $|\Delta\phi(\text{cluster}, \vec{E}_T^{\text{miss}})|$ cut. The MB1, adjacent MB1, and MB2 vetoes are already applied for these events.

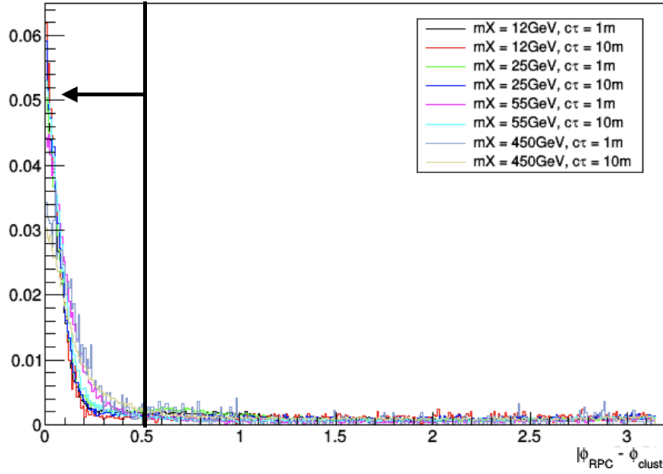


Figure 20: $|\Delta\phi(\text{RPC, cluster})|$ for RPC rechits and clusters from same the wheel for a variety of signal models.

reconstructed muon segments across the detector. Figure 23 shows the number of DT segments with $\Delta R(\text{cluster, segment}) > 0.4$ in the top and bottom hemispheres of the detector for signal and background. The long tails of background events with many segments come from cosmic showers, and clusters in these events contribute to the signal region. Events with more than 14 segments in either hemisphere or more than 10 in both are vetoed. The inefficiency for background and signal is similar overall, but the rejection from this cut is crucial to remove large backgrounds that contribute to the signal region without this cut.

6.6 Orientation of cluster and missing transverse energy

In an event with high E_T^{miss} , it is possible for pileup to produce a DT cluster that is not related to the source of the \vec{E}_T^{miss} so should be equally likely to be at any $\Delta\phi$ from the \vec{E}_T^{miss} . Conversely, the \vec{E}_T^{miss} in signal is coming from the same boosted Higgs system that gives the cluster, so the

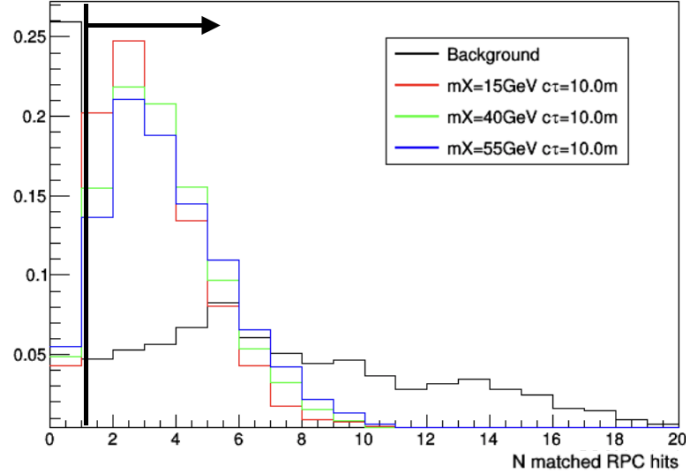


Figure 21: Signal and background distributions showing the number of RPC rechits matched to each cluster. The background is measured in a control region selected by inverting the $|\Delta\phi(\text{cluster}, \vec{E}_T^{\text{miss}})|$ cut.

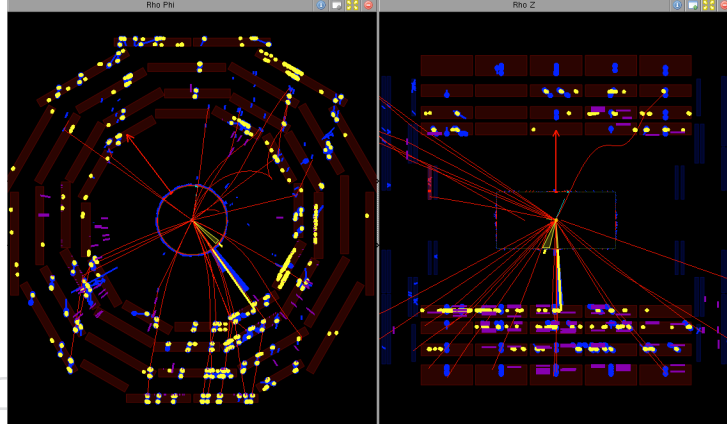


Figure 22: Example event display showing the type of cosmic muon shower event that produces many hits across all stations and wheels of the Barrel Muon System. Tracker tracks are not drawn to make making and interpreting the event displays easier.

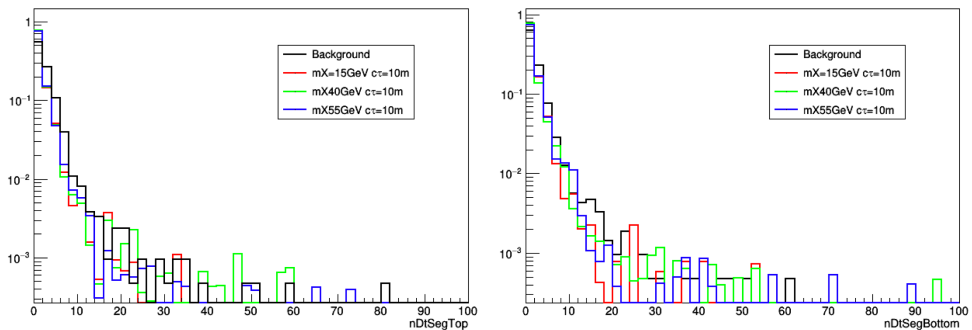


Figure 23: Signal and background distributions showing the number of DT segments in the top (left) and bottom (right) halves of the detector. The background is measured in a control region selected by inverting the MB1 veto cut.

436 \vec{E}_T^{miss} and the cluster should be aligned. These features can be seen in Figure 24. By requiring
 437 $|\Delta\phi(\text{cluster}, \vec{E}_T^{\text{miss}})| < 1.0$, only a factor of $1/\pi$ of the random background passes while signal
 438 is nearly 100% efficient.

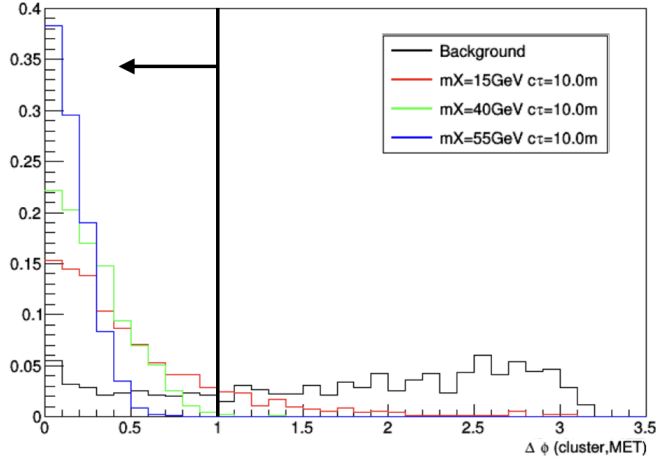


Figure 24: $|\Delta\phi(\text{cluster}, \vec{E}_T^{\text{miss}})|$ distributions for signal and background. The background is measured in a control region selected by requiring the clusters have 0 matched RPC rechits.

439 6.7 Cluster size

440 Most of the backgrounds give relatively few hits in the DTs, so the number of hits in back-
 441 ground clusters falls off quickly. For signal, the distribution falls off much more slowly and
 442 many clusters are well beyond the minimum size of 50 hits. The difference is shown in Fig-
 443 ure 25. Signal region clusters are required to have at least 100 clustered rechits, while the
 444 50-100 rehit clusters can be used as a control sample. This cut is not optimized for any spe-
 445 cific model, but the change in signal and background efficiencies resulting from changing this
 446 threshold does not result in any significant change to the expected results.

447 6.8 Signal region orthogonality

448 In order to keep the DT cluster search independent from the signal regions in the CSC cluster
 449 search and the two cluster signal regions of the combination, a veto is applied to remove events
 450 that would enter multiple analysis regions. Preference is given to the all the ABCD regions of
 451 the double-cluster and the single CSC cluster analyses, then to the single DT analysis regions.
 452 An event will only be included in a single DT control or signal region if it is not in any control
 453 or signal regions of the other searches. The effect of this veto is a few percent, depending on
 454 the model.

455 6.9 DT noise

456 One remaining possible source of unpredicted background is due to noise in the DTs that is
 457 localized in time and/or location. Figure 26 shows the R, z and ϕ location of clusters in 2016
 458 data. These clusters pass a loose selection of jet, muon, and MB1 vetoes. Nearly half of the
 459 clusters are found in MB2/Wheel 1 near $\phi = 0.5$. The run number for this peak is shown in
 460 Figure 27. There is a large spike in the number of clusters in this region during a short part of
 461 the 2016C era (corresponding to about 1.5 fb^{-1}), due to a few noisy wires in the DTs. Since this
 462 spike gives more clusters than every other part of the detector, clusters that are found in Wheel

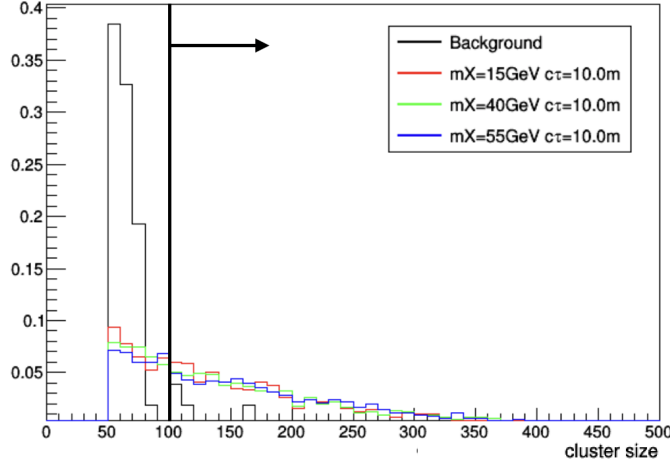


Figure 25: Cluster size distributions for signal and background. The background is measured in a control region selected by inverting the $|\Delta\phi(\text{cluster}, \vec{E}_T^{\text{miss}})|$ cut. Signal and background events both pass the jet and E_T^{miss} event-level requirements, and the clusters pass the jet, muon, and MB1 vetoes.

463 1/Sector 2 where the station with most hits in the cluster is MB2, for runs 275750-275950 are
 464 vetoed.

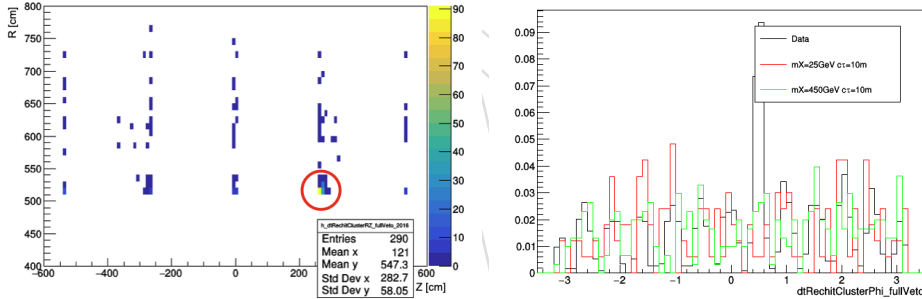


Figure 26: Cluster R, z (left) and ϕ (right) locations for background clusters passing the jet, muon, and MB1 vetoes for 2016 data. Nearly half of the clusters are localized to one station and wheel, with a large peak near $\phi = 0.5$.

465 A similar spike is also seen in 2018 data in MB4/Wheel -2. Figure 28 shows the location of
 466 a subset of MB4 clusters that were appearing in the inverted MB1 veto CR. These clusters
 467 are not spread uniformly across the detector, but predominantly show up in Wheel -2 with
 468 $-1.8 < \phi < -1.6$. The run number plot also shows that the rate of these clusters increases
 469 significantly in 2018. Clusters in this station/wheel/phi portion of the detector in 2018 data are
 470 vetoed.

471 The corresponding signal inefficiency for these noise filters, about a 1% effect, is accounted for
 472 in the overall signal efficiencies.

473 6.10 The signal regions

474 The signal region selection requires that an event passing all event-level cuts must have at least
 475 one cluster that passes all cluster requirements. These requirements are summarized in Table 7.
 476 One remaining variable that is unused is the DT station of the cluster, which can be from MB2-

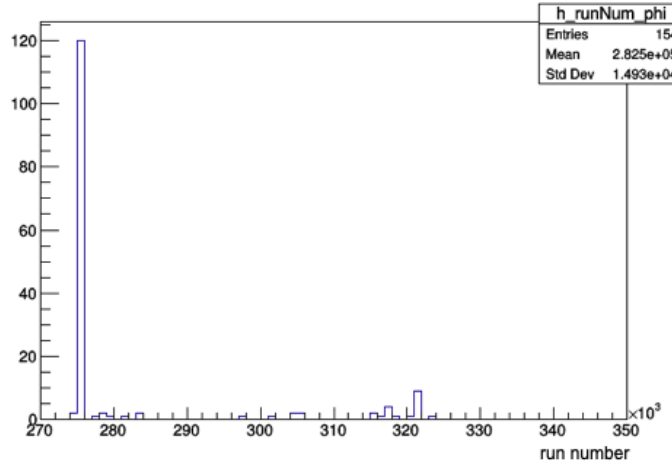


Figure 27: Run number for 2016 background clusters with $0.4 < \phi < 0.6$ passing the jet, muon, and MB1 vetoes for 2016 data. Nearly all of the clusters are from one portion of 2016C era.

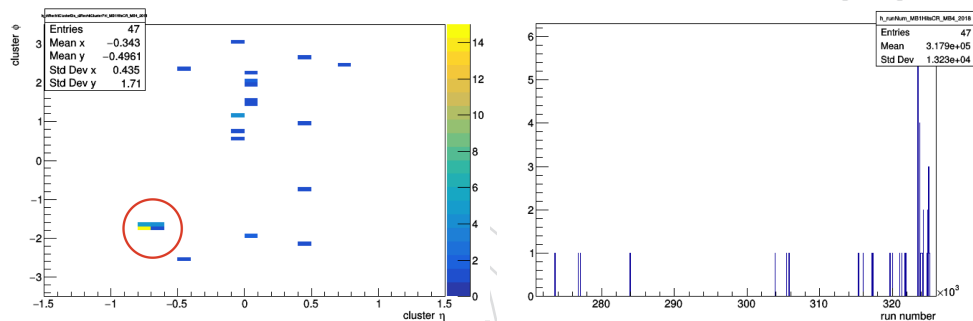


Figure 28: η, ϕ locations and run number for an excess of clusters in MB4 seen in the inverted MB1 veto CR. The clusters are localized to a small portion of ϕ in Wheel -2. The rate of these events increases significantly in 2018 data.

477 4. Possible remaining backgrounds are expected to be different depending on the station. MB2
 478 has a larger punch-through background contribution than MB3 which has more punch-through
 479 than MB4 because the punch-through contribution falls off as it must pass through more ma-
 480 terial to get to the outer stations. Clusters are categorized by which station has the most hits
 481 in the cluster, so punch-through will almost always contribute to MB2 background rather than
 482 MB3 or MB4. Because the different background contributions lead to different background
 483 predictions, three signal regions are used - one for each of the MB stations.

Table 7: Summary of the selections used to define the signal region.

Object	Selection
Event level	$E_T^{\text{miss}} > 200 \text{ GeV}$
Event level	$N_{\text{jets}} > 0$
Event level	$N_{\text{DT segments } \phi>0} \leq 14 \text{ AND } N_{\text{DT segments } \phi<0} \leq 14$
Event level	$N_{\text{DT segments } \phi>0} \leq 10 \text{ OR } N_{\text{DT segments } \phi<0} \leq 10$
Event level	$\min \Delta\phi(\text{jet}, \vec{E}_T^{\text{miss}}) > 0.6$
Event level	$N_{\text{clusters}} > 0$
Event level	Pass CSC cluster and DT noise filters
Leading jet	$p_T > 30 \text{ GeV AND } \eta < 2.4 \text{ AND pass loose ID}$
DT clusters	Not $\Delta R < 0.4$ matched to jet with $p_T > 10 \text{ GeV}$ or $\Delta R < 1.2$ with leading jet
DT clusters	Not $\Delta R < 0.4$ matched to loose ID muon with $p_T > 10 \text{ GeV}$
DT clusters	Not $\Delta R < 0.4$ matched to more than 1 MB1 rechit or 1 MB2 rechit (MB3-4 clusters)
DT clusters	Not $\Delta\phi < \pi/4$ matched to more than 8 adjacent MB1 rechits or MB2 rechits (MB3-4 clusters)
DT clusters	Matched to at least 1 RPC rechit
DT clusters	$ \Delta\phi(\text{cluster}, \vec{E}_T^{\text{miss}}) < 1.0$
DT clusters	$N_{\text{rechits}} \geq 100$

484 7 Background estimation

485 Section 6.2 lists the dominant sources of background clusters. The contribution of each of these
 486 backgrounds to the signal region after all cuts are made can be estimated with data-driven
 487 methods.

488 The contributions from noise and pileup are predicted using an ABCD method, with the plane
 489 defined by N_{rechits} and $|\Delta\phi(\text{cluster}, \vec{E}_T^{\text{miss}})|$. Signal clusters are expected to have $|\Delta\phi(\text{cluster}, \vec{E}_T^{\text{miss}})|$
 490 peak at 0 while the random background is expected to be flat (since \vec{E}_T^{miss} is not correlated with
 491 the cluster position for these backgrounds), and the N_{rechits} for signal extends past 100 while
 492 the background distribution falls off between 50 and 100.

493 The ABCD plane is shown in Figure 29, with region D being the signal region. Because the
 494 two variables are expected to be independent and signal contamination in the other 3 regions
 495 is low, the background prediction for the signal region is given by $N_D = N_B \times \frac{N_C}{N_A}$.

496 Since the random background is expected to be flat in $|\Delta\phi(\text{cluster}, \vec{E}_T^{\text{miss}})|$, the ratio $\frac{N_C}{N_A}$ is ex-
 497 pected to be given by the relative ϕ sizes of the two regions. This ratio should also therefore
 498 be constant across different stations. Due to the small number of events expected in the ABCD
 499 regions of the MB3 and MB4 selections, regions C and A are combined to measure the ratio and
 500 predict the background in region D using the region B yields in MB3 and MB4.

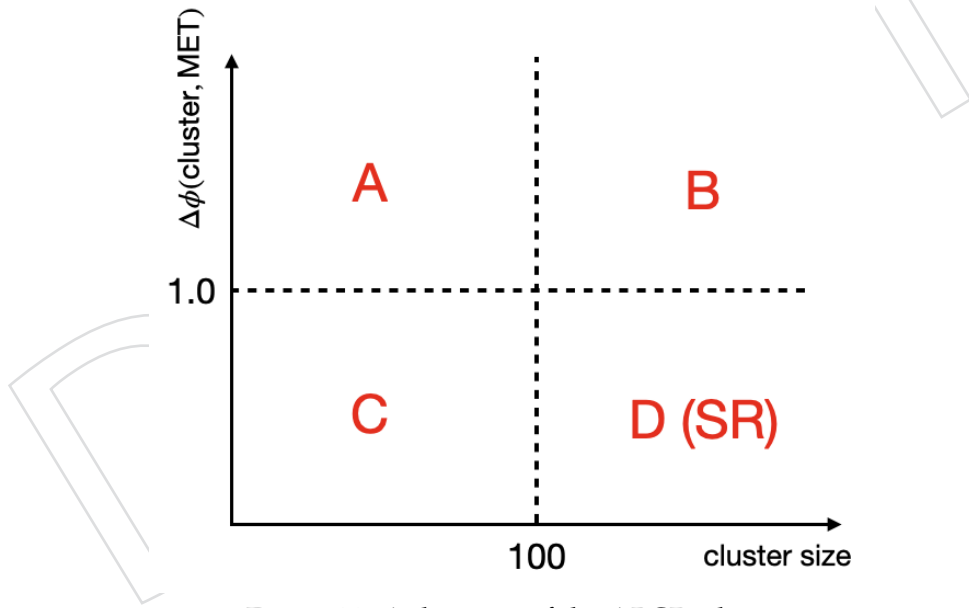


Figure 29: A diagram of the ABCD plane.

501 The ABCD method relies on the $|\Delta\phi(\text{cluster}, \vec{E}_T^{\text{miss}})|$ and cluster size being independent, there-
 502 fore backgrounds that have correlated \vec{E}_T^{miss} and cluster directions are not included in this
 503 method and are instead predicted separately. Clusters from punch-through jets and primary
 504 vertex muons fall into this correlated-direction category and contribute to the signal region
 505 background. These backgrounds are enriched by inverting the MB1 and MB2 vetoes and their
 506 contribution to the signal region is predicted by deriving a transfer factor from the inverted
 507 MB1 selection to the signal region.

508 **7.1 Testing the ABCD prediction method**

509 The ABCD method is tested using a validation region enriched in the random backgrounds
 510 that the ABCD is designed to predict. For this validation region, no E_T^{miss} filters are applied. The
 511 leading p_T jet must fail the loose ID criteria and no cut is made on the leading jet $|\Delta\phi(\text{jet}, \vec{E}_T^{\text{miss}})|$.
 512 This selection is dominated by events where the E_T^{miss} is fake or mis-measured, which happens
 513 for the noise and pileup events predicted by the ABCD. Additionally, no RPC match require-
 514 ment is made for the clusters, which increases the statistics of the validation test by enriching
 515 the selection with clusters caused by noise.

516 The test of the ABCD prediction versus observed events is shown in Table 8. For the MB2
 517 signal-like region, 1.3 ± 0.9 events were predicted and 3 were observed. For the MB3 signal-
 518 like region, 0.4 ± 0.4 events were predicted and 1 was observed. For the MB4 signal-like region,
 519 0.0 ± 1.3 events were predicted and 1 was observed. The MB3 and MB4 predictions are made
 520 combining the A and C regions, following the method for the signal region prediction. The
 521 observed consistency in these background dominated regions is taken as validation of the pre-
 522 diction method.

Table 8: Inverted Jet ID and E_T^{miss} filters ABCD prediction

Cluster station	A	B	C	D (pred.)	D (obs.)
MB2	130	2	82	1.3 ± 0.9	3
MB3	20	1	11	0.4 ± 0.4	1
MB4	0			0.0 ± 1.1	1

523 **7.2 Estimation of non-random background**

524 The background which cannot be predicted by the ABCD because of the correlation in \vec{E}_T^{miss} and
 525 cluster ϕ is predicted separately in a control sample defined by inverting the MB1 and MB2 ve-
 526 toes. This correlated background includes: punch-through clusters where an under-measured
 527 jet results in E_T^{miss} and can cause a DT cluster; cosmic muons that can form a cluster through
 528 bremsstrahlung on one side of the detector and incorrectly reconstructed or not reconstructed
 529 at all on the other side; and boosted W boson decays that produce E_T^{miss} and a muon that can
 530 cause a cluster. The full selection in Table 7 is applied, except requiring that the cluster does
 531 match more than 1 MB1 rechit and more than 1 MB2 rechit. This inversion gives a selection
 532 dominated by backgrounds that are heavily suppressed by the actual MB1 and MB2 vetoes,
 533 such as clusters from punch-through jets and muon backgrounds. These backgrounds can be
 534 studied with high statistics in this region. The number of events with clusters passing signal
 535 region-like $|\Delta\phi(\text{cluster}, \vec{E}_T^{\text{miss}})|$ and cluster size requirements can be measured in the inverted
 536 MB1/MB2 region, and given the efficiency of the vetoes for these backgrounds, the actual con-
 537 tribution to the signal region can be predicted.

538 **7.2.1 Inverted MB1 region**

539 The distribution of N_{rechits} and $|\Delta\phi(\text{cluster}, \vec{E}_T^{\text{miss}})|$ are shown in Figure 30. There is a correlation
 540 between \vec{E}_T^{miss} and cluster ϕ for the backgrounds enriched in this region, and these backgrounds
 541 tend to result in larger clusters than other random background sources. The observed number
 542 of events above the random prediction gives the size of the correlated backgrounds in this

543 region, and those events can be used to understand the size of the non-random background in
 544 the signal region.

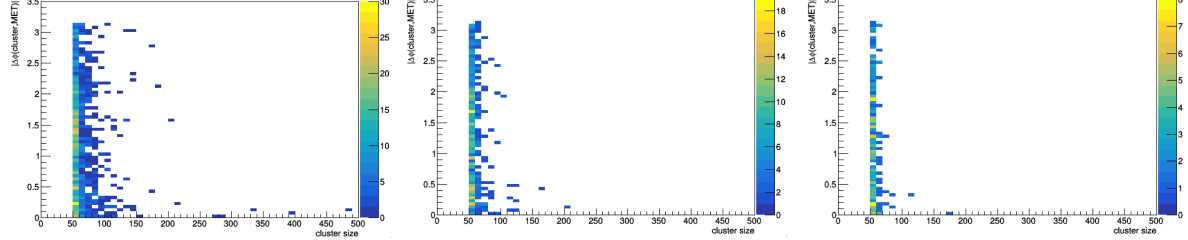


Figure 30: The distribution of $|\Delta\phi(\text{cluster}, \vec{E}_T^{\text{miss}})|$ and cluster size for events with MB2 (left), MB3 (center), and MB4 (right) clusters that pass the inverted MB1/MB2 veto control region selection.

545 The ABCD random cluster prediction and observed events in this inverted MB1/MB2 veto
 546 control region are shown in Table 9. For the MB2 signal-like region, 13.6 ± 3.1 events were
 547 predicted and 36 were observed. For the MB3 signal-like region, 0.6 ± 0.6 events were pre-
 548 dicted and 8 were observed. For the MB4 signal-like region, 0.0 ± 1.0 events were predicted
 549 and 2 were observed. The excesses observed in these regions indicate an additional correlated
 550 background of about 22.4, 7.4, and 2 events with the inverted MB1/MB2 veto in stations MB2,
 551 MB3, and MB4, respectively. Punch-through contributes less as the station number increases
 552 since that background falls off with increasing detector radius, which is consistent with the
 553 observed number of events in each region. The observed correlated background from this test
 554 is used in the following sections to predict the additional background in the signal region.
 555 Given the number of observed events in region D of this control sample, the contribution of
 556 punch-through and isolated muon clusters in the signal region can be predicted separately by
 557 measuring the MB1/MB2 veto efficiency for these two types of backgrounds.

Table 9: Inverted MB1 ABCD prediction

Cluster station	A	B	C	D (pred.)	D (obs.)
MB2	717	20	487	13.6 ± 3.1	36
MB3	359	1	227	0.6 ± 0.6	8
MB4	120	0	93	0.0 ± 1.0	2

558 7.2.2 Punch-through background

559 The punch-through background can be studied further by inverting the jet veto so the cluster is
 560 matched to a jet (see Figure 31). This inversion, like the MB1/MB2 veto inversion, enriches in
 561 any background that gives hits in the inner parts of the detector before creating a cluster of hits
 562 in MB2-4. Matching clusters to jets gives a selection of punch-through clusters, but to contribute
 563 to the signal region, these clusters must pass both the MB1 and jet vetoes. To understand
 564 the fraction of clusters that can pass both, the MB1/MB2 veto efficiency is measured for this
 565 background as a function of matched jet p_T (see Figure 32. This measurement is made without
 566 applying the $|\Delta\phi(\text{cluster}, \vec{E}_T^{\text{miss}})|$ cut to increase statistics for the test, and the rate of a cluster
 567 matched to a jet that still passes the MB1/MB2 veto should be a feature of the cluster and jet,
 568 not the \vec{E}_T^{miss} .

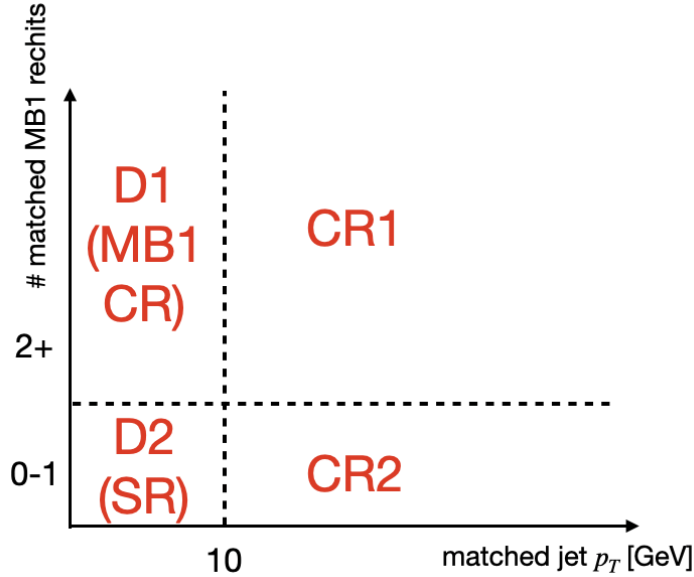


Figure 31: A sketch of the regions used to study the punch-through background. The ratio of CR2 to CR1 is measured as a function of matched jet p_T , and that measurement is extrapolated to determine the ratio between D2 and D1, ultimately giving a prediction of the size of the punch-through background in the signal region (D2), given the observed background in the inverted MB1/MB2 veto region (D1).

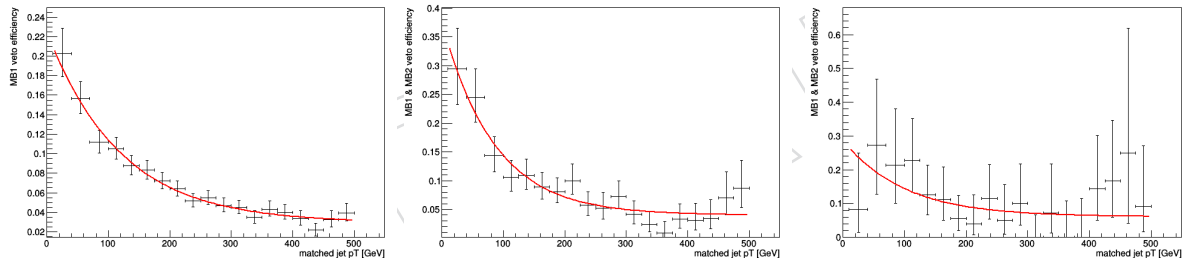


Figure 32: MB1 and MB2 veto efficiency for MB2 (left), MB3 (center), and MB4 (right) clusters measured as a function of matched jet p_T in an inverted jet veto selection. Only the MB1 veto efficiency is measured for MB2 clusters, while the efficiency measured for MB3 and MB4 clusters is the efficiency to pass both the MB1 and MB2 vetoes. The distributions are fit to an exponential which is used to extrapolate to the signal region. The χ^2 per degree of freedom of the fits are 11.1/16, 12.0/16, and 14.2/16 for MB2, MB3, and MB4, respectively.

- 569 Clusters that are matched to jets may pass the MB1/MB2 veto if the cluster matches to an
 570 unrelated jet randomly so there is not expected to be any associated MB1/MB2 hits, or if the
 571 cluster comes from a real jet or muon which produces a cluster in MB2-4 with no matched hits
 572 in inner stations, either because of gaps in detector coverage or because particles bend enough
 573 so that the cluster, MB1 hits, and the jet cannot all be matched to each other. The dominant
 574 source of punch-through clusters that pass these vetoes is jets that punch through a gap in the
 575 coverage of the inner chambers and form a cluster in an outer station (see Appendix B).
- 576 Jets are more likely to punch through into the muon system as p_T increases, and as p_T increases
 577 so does the number of particles that can punch through, which makes leaving associated hits in
 578 MB1 more likely. Since high- p_T jets have a higher likelihood of punching through the detector
 579 and have more particles that can give hits in MB1, high- p_T punch-through is unlikely to pass

580 the MB1 veto unless the jet punches through a gap in MB1. However, low- p_T jets are unlikely
 581 to be able to punch through all the way to an outer MB station unless they make it through a
 582 gap in MB1. They will also have fewer particles punch through, so the likelihood that there is
 583 more than 1 MB1 rechit associated with the cluster is lower. This effect can be seen in Figure 32,
 584 which shows the MB1/MB2 veto efficiencies as a function of matched jet p_T for clusters in the
 585 inverted jet veto selection. The p_T dependence is more prominent for MB2 and MB3 clusters
 586 than for those in MB4. In order for punch-through to give a cluster in MB3 or MB4 it must
 587 miss all the inner stations, otherwise those stations will likely have more DT hits and be the
 588 location of the cluster. At all p_T this will only happen if the jet lines up with a gap in MB1 and
 589 MB2 (and MB3 for MB4 clusters). This makes MB4 clusters in this category rare, which leads
 590 to fewer events in the sample and larger uncertainties. This is consistent with the amount of
 591 punch-through observed in the signal-like regions of the inverted MB1 and MB2 vetoes CR, as
 592 well as the size of the predicted punch-through in each signal region.

593 These distributions are fit to an exponential which can be used to extrapolate below the jet veto
 594 threshold, to predict the veto efficiencies for clusters that actually pass the jet veto. The choice
 595 of exponential is empirical, however, the χ^2 per degree of freedom of the fit across a wide range
 596 of matched jet p_T is 11.1/16. The predicted MB1 veto efficiency for MB2 clusters that would
 597 be matched to jets with $p_T < 10$ GeV (i.e. would pass all other MB2 signal region cuts) is
 598 0.225 ± 0.020 . For MB2 clusters matched to jets with $p_T < 10$ GeV (or no jet), about 1 in 4 will
 599 pass the MB1 veto. This veto efficiency gives a ratio of pass:fail of 0.290 ± 0.033 . This is the
 600 ratio of punch-through events in the MB2 cluster signal region to punch-through events in the
 601 MB2 cluster inverted MB1 veto region D. Assuming all 22.4 unpredicted events in the inverted
 602 MB1 region D are from this type of punch-through background, the expected background in
 603 the signal region is then 6.5 ± 2.1 in addition to the ABCD prediction.

604 A similar method is used in the MB3 and MB4 signal regions. The predicted MB1 and MB2
 605 veto efficiency for MB3 clusters that would be matched to jets with $p_T < 10$ GeV (i.e. would
 606 pass all other MB3 signal region cuts) is 0.376 ± 0.070 . This veto efficiency gives a ratio of
 607 pass:fail of 0.603 ± 0.180 . Assuming the 7.4 unpredicted events in the inverted MB1 region D
 608 is from punch-through, the expected background in the MB3 signal region is then 4.4 ± 2.2 in
 609 addition to the ABCD prediction. For MB4 clusters, the measured MB1 and MB2 veto efficiency
 610 is 0.286 ± 0.135 , which corresponds to a pass:fail ratio of 0.401 ± 0.265 . This gives a predicted
 611 punch-through background of 0.8 ± 0.9 events in MB4.

612 The uncertainties on these predictions are the propagated statistical uncertainties on the num-
 613 ber of events used in each step of the method for the two signal regions as well as the uncer-
 614 tainty on the predicted efficiency from the exponential fit.

615 The number of events in each region in this study is summarized in Table 10.

Table 10: Events in each region used for the MB2 punch-through background prediction

Cluster station	CR1	CR2	D2	D1 (pred.)
MB2	3878	222	22.4 ± 6.8	6.5 ± 2.1
MB3	293	21	7.4 ± 2.9	4.4 ± 2.2
MB4	36	1	2.0 ± 1.7	0.8 ± 0.9

7.2.3 Validating punch-through prediction method

Two tests are done to validate the method used to predict the punch-through background in the signal regions. The first tests the consistency of the test when the $|\Delta\phi(\text{cluster}, \vec{E}_T^{\text{miss}})|$ is required to match the signal region cut. This is a lower statistics test than using the full range, as seen in Figure 33. The predicted veto efficiencies below 10 GeV are 0.258 ± 0.055 , 0.412 ± 0.156 , and 0.029 ± 0.025 for MB2, MB3, and MB4 clusters, respectively. The uncertainties on these low statistics tests are relatively, but the predictions are consistent with the higher statistics measurement. The individual parameter values of the fits each agree within their uncertainties between the two studies. The largest differences are seen in MB4, where the statistics are very low.

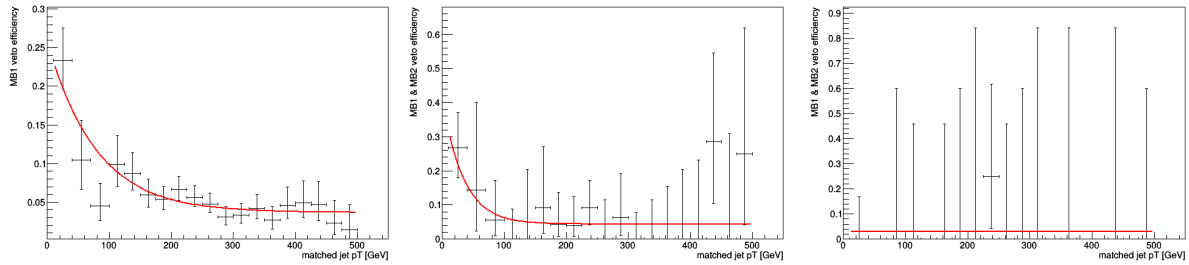


Figure 33: MB1 and MB2 veto efficiency for MB2 (left), MB3 (center), and MB4 (right) clusters measured as a function of matched jet p_T in an inverted jet veto selection. Only the MB1 veto efficiency is measured for MB2 clusters, while the efficiency measured for MB3 and MB4 clusters is the efficiency to pass both the MB1 and MB2 vetoes. The distributions are fit to an exponential which is used to extrapolate to the signal region, and the predicted efficiencies are consistent with the predictions using the higher statistics, full $|\Delta\phi(\text{cluster}, \vec{E}_T^{\text{miss}})|$ selection.

The second test of the method is done within the inverted MB1/MB2 selection. Instead of using the method to predict the clusters in the signal region matched to fewer than 2 MB1 rechits, the method is used to predict the clusters in the inverted MB1 signal-like region with 2-5 matched MB1 rechits. The regions used are analogous to those in Figure 31, but rather than regions D1/CR1 and D2/CR2 being 0-1 and 2+ matched MB1 rechits, the regions for this test are 2-5 and 6+ matched MB1 rechits for the MB2 cluster region. For MB3-4 clusters, the low rechits regions are where clusters match to either 2-5 MB1 rechits or 2-5 MB2 rechits, and the high rechits region is the inverse of this. With the inverted MB1 veto applied, the fraction of clusters matched to a small number of hits is measured as a function of jet p_T , as seen in Figure 34. Rather than the signal region prediction which was a prediction from one orthogonal region to another, this is a measurement of the fraction of low number of matched MB1/MB2 hits within the entire matched MB1/MB2 hits control region.

The exponential fit to the data predicts that for clusters in the signal-like region (matched to jets with $p_T < 10$ GeV), the fraction that are in the low hits region is 0.208 ± 0.020 for MB2, 0.207 ± 0.097 for MB3 and 0.478 ± 0.157 for MB4. Given the observed punch-through clusters, equal to the difference between the observed and predicted uncorrelated events in Table 9, the expected number of events in the low hits regions are 4.7 ± 1.5 for MB2, 1.5 ± 0.9 for MB3, and 1.0 ± 0.9 for MB4. There were 6 such clusters observed in MB2, and 0 in MB3 and MB4. All 3 observations are consistent with the predicted values within the uncertainties. The numbers of events in each region in this study are summarized in Table 11.

Together, these two tests indicate that this prediction method is a valid way to measure the punch-through background, within statistical uncertainty due to the small number of events used in the prediction and validations.

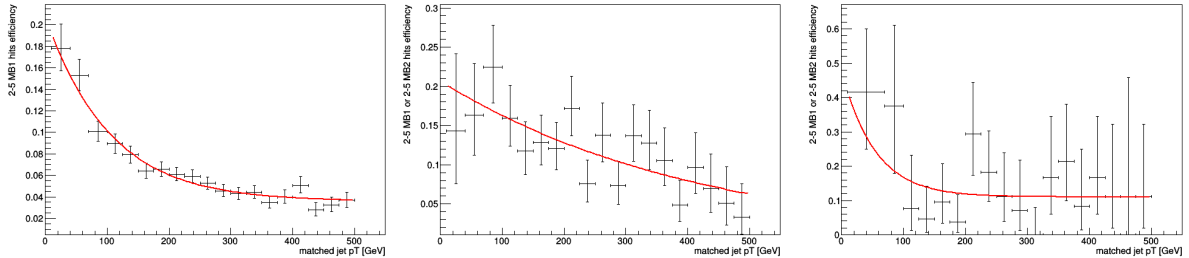


Figure 34: Fraction of MB2 (left), MB3 (center), and MB4 (right) clusters in the inverted MB1/MB2 veto selection that are matched to 2-5 MB1 hits (MB2 clusters) or 2-5 MB1 hits or 2-5 MB2 hits (MB3-4 clusters), measured as a function of matched jet p_T in an inverted jet veto selection. The distribution is fit to an exponential which is used to extrapolate to the signal-like region, below 10 GeV, which is used to predict the number of 2-5 MB1 matched clusters in the signal-like region. The prediction is consistent with the observed number of such clusters, providing a validation of this type of test.

Table 11: Events in each region used for the validation of the punch-through background prediction using the inverted MB1/MB2 veto control region

Cluster station	CR1	CR2	D1	D2 (pred.)	D2 (obs.)
MB2	3713	165	30	4.7 ± 1.5	6
MB3	258	21	8	1.5 ± 0.9	0
MB4	29	6	2	1.0 ± 0.9	0

649 7.2.4 Isolated muon background

650 The previous section described a method to predict the punch-through background in the sig-
 651 nal region. This method uses an inverted jet veto, so the backgrounds predicted are any process
 652 that can form both a cluster and a jet, including some muons. The method does not address
 653 backgrounds that do not form jets, and the dominant type of this background is clusters pro-
 654 duced by bremsstrahlung photons from isolated muons that are not identified by the muon
 655 veto. The source of these isolated muons are W+Jets events, where the W is boosted against a
 656 high- p_T jet and decays to a muon and a neutrino. This results in a high- p_T ν , giving enough
 657 E_T^{miss} to pass the requirement, and if the muon produces a cluster through bremsstrahlung, the
 658 cluster and \vec{E}_T^{miss} will have small ϕ separation and contribute to the signal region. This section
 659 estimates the size of this background in the signal region.

660 The tag-and-probe muon bremsstrahlung selection described in Section 8 gives the type of clus-
 661 ters necessary to study this background. Clusters in this selection are required to match muons
 662 that pass loose ID and isolation requirements. To further clean the selection, the clusters cannot
 663 be matched to any jets, so that they would not be covered by the punch-through prediction.
 664 The final requirement is that the clusters are matched to 10-16 hits in MB1. A muon traveling
 665 through MB1 leaving one hit in each DT layer will give 12 hits, so the 10-16 requirement adds
 666 an additional check that the cluster is from a muon traversing MB1.

667 The distribution of cluster sizes for this selection is plotted in Figure 35. The distribution is
 668 fit to an exponential function which is drawn in red. The bulk of the distribution falls off
 669 exponentially, but there is a small tail that extends to higher cluster sizes that appears to be

670 from a different distribution. The ratio of clusters with at least 100 rechits to those with fewer
 671 than 100 rechits is measured to be 0.017 ± 0.007 . Since these are the same types of muons that
 672 may be an unpredicted background, this ratio can be used to predict the contribution to the
 673 signal region, given an estimate of the non-vetoed muon sample size. Figure 36 shows that the
 674 size of these clusters does not depend on which MB station the cluster forms in, so the value
 675 taken from the combined distribution is used.

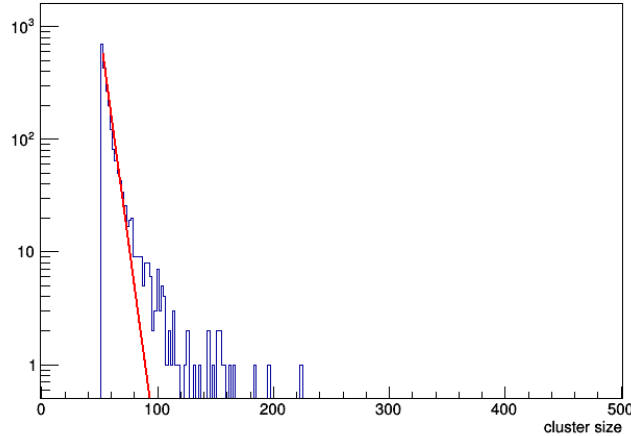


Figure 35: Cluster size for clusters matched to the probe muon in the muon bremsstrahlung selection and pass the jet veto and 10-16 matched MB1 hits requirement. The plot is fit to an exponential function, drawn in red. This distribution is used to measure the ratio of large to small clusters, using the signal region cut of 100 rechits.

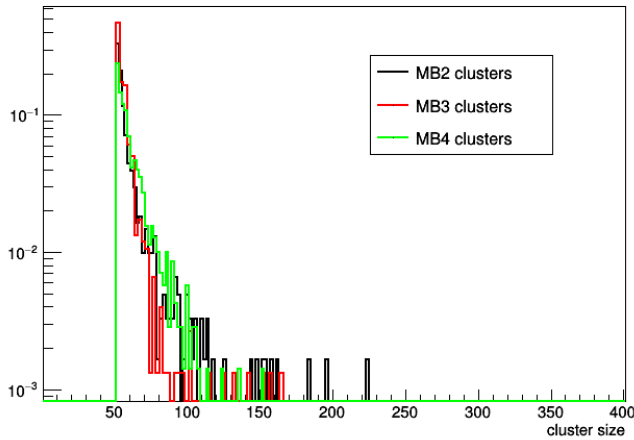


Figure 36: Cluster size for clusters matched to the probe muon in the muon bremsstrahlung selection and pass the jet veto and 10-16 matched MB1 hits requirement, for three different Barrel Muon System stations. The size distribution is constant across the three stations. Additionally, the ratio of clusters above 100 rechits to below 100 rechits is the same within statistical uncertainty for the three stations.

676 The size of this isolated muon background is estimated using region C of the inverted MB1/MB2
 677 selection. Assuming that all 487 clusters in region C of the MB2 selection are from isolated
 678 muons (an overestimate), the measured ratio predicts there would be 8.3 ± 1.4 clusters from
 679 isolated muons in region D. These clusters would be on top of the uncorrelated background

680 prediction, like the punch-through. These 8.3 ± 1.4 predicted clusters fail the MB1 veto, but the
 681 fraction of similar clusters that would pass the MB1 veto can be estimated. Figure 37 shows
 682 the number of MB1 hits matched to clusters that are also matched to RECO muons in a low
 683 $|\Delta\phi(\text{cluster}, \vec{E}_T^{\text{miss}})|$, low cluster size selection (region C with an inverted RECO muon veto).
 684 RECO muons are used here rather than the loose muons used to define the actual muon veto
 685 to include clusters from muons that may not be well-measured, which are likely the types of
 686 muons that could produce clusters in the signal region. The ratio of these clusters that could
 687 pass the MB1 veto to those that would fail is measured to be 0.083 ± 0.033 . Given the 8.3 ± 1.4
 688 predicted clusters in the inverted MB1 region D, the expected number of clusters in the signal
 689 region is 0.7 ± 0.3 .

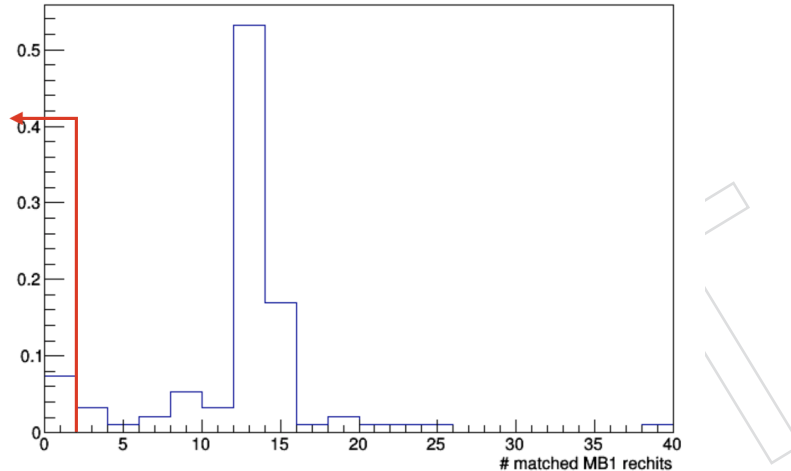


Figure 37: Number of MB1 rechits matched to clusters that are matched to RECO muons. The majority of these clusters are matched around 12 MB1 hits, the expected number for a muon, but about 8% of the clusters can pass the MB1 veto.

690 Repeating this procedure for MB3-4 clusters and predicting the number of clusters from muons
 691 that could pass both the MB1 and MB2 vetoes also gives an estimate of a few tenths of an event
 692 in the signal region.

693 In this estimation of the background, there is a significant number of clusters from isolated
 694 muons in inverted MB1/MB2 region D. Therefore, the punch-through prediction must be re-
 695 done since the isolated muon and punch-through predictions are for distinct background sources.
 696 With the assumed number of isolated muon clusters, the number of clusters from punch-
 697 through is taken to be smaller, equal to the total observation minus the muon clusters and
 698 uncorrelated prediction. This then gives a smaller prediction for the punch-through in the sig-
 699 nal region than the punch-through only prediction.

700 Estimating the combination of punch-through plus isolated muons gives a prediction that is
 701 about 1 sigma smaller than the estimate of only punch-through. Since the MB1/MB2 veto
 702 efficiencies are much smaller for isolated muon clusters than for punch-through clusters, as-
 703 suming any isolated muon background in the inverted MB1/MB2 region D will necessarily
 704 lead to a smaller overall background prediction in the signal region. Because of this, the most
 705 conservative approach is taken, and the inverted MB1/MB2 regions are assumed to have only
 706 punch-through and no isolated muons. The only additional contribution beyond the uncorre-
 707 lated background included in the likelihood is the punch-through background.

708 **8 Modeling of key variables**

709 This section demonstrates the validation of the modeling of the variables used to define the
 710 signal region. Potential mis-modeling observed from comparisons of signal MC and data is
 711 taken as a systematic uncertainty on the signal efficiency.

712 **8.1 Muon bremsstrahlung comparison**

713 Muon bremsstrahlung is used as a proxy for signal, as high energy muons can produce photons
 714 that shower in the DTs, giving a signal-like cluster. A proxy like this is required since there is
 715 no straightforward Standard Model process that can be used to study signal modeling directly.
 716 These showers are photons and electrons, but they are used as a proxy for the hadronic showers
 717 of the benchmark Twin Higgs model and the various showers of the Dark Shower models since
 718 they are the only way to study signal modeling. This selection is made using Drell-Yan to $\mu\mu$
 719 datasets. Table 12 shows the RECO datasets used for this comparison, while Table 13 details
 720 the MC samples used.

Table 12: Zmumu skim of SingleMuon datasets used to study signal modeling

```
/SingleMuon/Run2017H-ZMu-17Nov2017-v2/RAW-RECO
/SingleMuon/Run2017G-ZMu-17Nov2017-v1/RAW-RECO
/SingleMuon/Run2017F-ZMu-17Nov2017-v1/RAW-RECO
/SingleMuon/Run2017E-ZMu-17Nov2017-v1/RAW-RECO
/SingleMuon/Run2017D-ZMu-17Nov2017-v1/RAW-RECO
/SingleMuon/Run2017C-ZMu-17Nov2017-v1/RAW-RECO
/SingleMuon/Run2017B-ZMu-17Nov2017-v1/RAW-RECO
```

Table 13: Monte Carlo samples used to study signal modeling

MC samples	σ (pb)
ZToMuMu_NNPDF31_13TeV-powheg_M_50_120	2112.9
ZToMuMu_NNPDF31_13TeV-powheg_M_120_200	20.55
ZToMuMu_NNPDF31_13TeV-powheg_M_200_400	2.889
ZToMuMu_NNPDF31_13TeV-powheg_M_400_800	0.251

721 A tag-and-probe method is used to select clean Drell-Yan events with isolated muons. Events
 722 must have two oppositely charged muons and both must have $p_T > 50 \text{ GeV}$ and $|\eta| < 2.4$.
 723 The invariant mass of the two muons is required to be $> 120 \text{ GeV}$ because using a Z mass
 724 requirement could bias against events with bremsstrahlung. The tag muon must pass tight
 725 muon ID and isolation requirements, while the probe muon must pass loose muon ID and
 726 isolation requirements. Additionally, MC reconstructed muons are required to be within $\Delta R <$
 727 0.4 of the generator-level muons.

728 The MC samples are normalized to the cross sections in Table 13 and scaled to match the 2017
 729 luminosity. Then a k-factor is derived for each sample to match the overall normalization

730 between MC and data seen in the dimuon mass distribution. The k-factors derived range from
 731 1.09-1.37 and after applying them, the dimuon mass distributions for data and MC agree (see
 732 Figure 38).

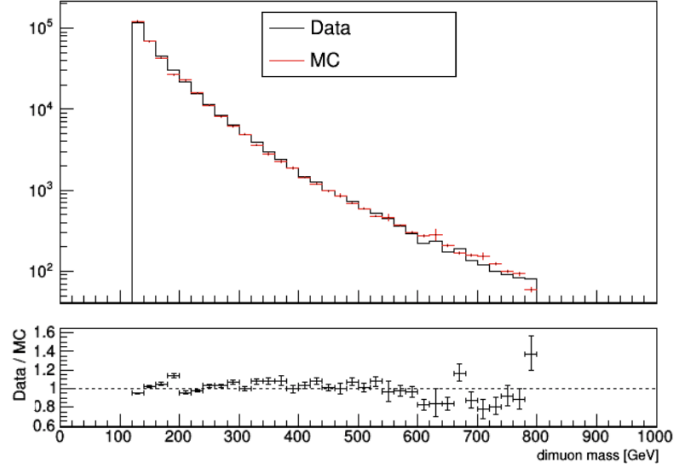


Figure 38: Dimuon mass distributions for MC and data in the Tag+Probe ZMuMu selection. The distributions agree after k-factors are derived and applied as overall normalization corrections.

733 To study the modeling of cluster properties, the probe muon is required to match $\Delta R < 0.4$ to
 734 a DT cluster. To ensure that the cluster is similar to the signal region clusters, it is required to
 735 pass the MB1 veto as well as RPC match requirement. The p_T of both the tag and probe muons
 736 (in data) after these requirements are made is shown in Figure 39.

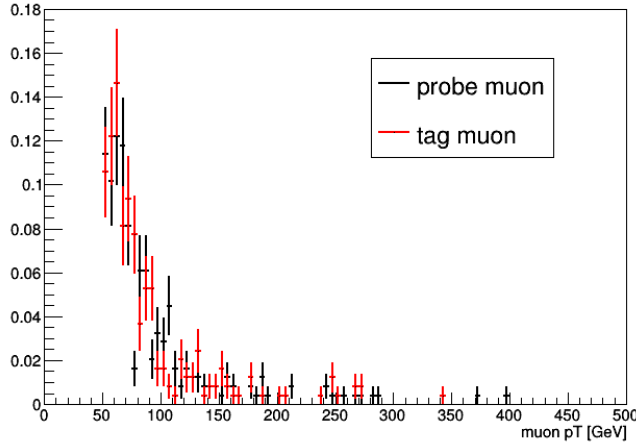


Figure 39: Tag and probe muon p_T for events passing the tag-and-probe requirements as well as cluster requirements on the DT cluster matched to the probe muon.

737 8.1.1 Clustering efficiency

738 The rate of matching a probe muon to a cluster can be used to study differences in clustering
 739 efficiency for data and MC. This efficiency can be studied for various probe muon and cluster
 740 properties. One example, shown in Figure 40, is clustering efficiency as a function of the η of the

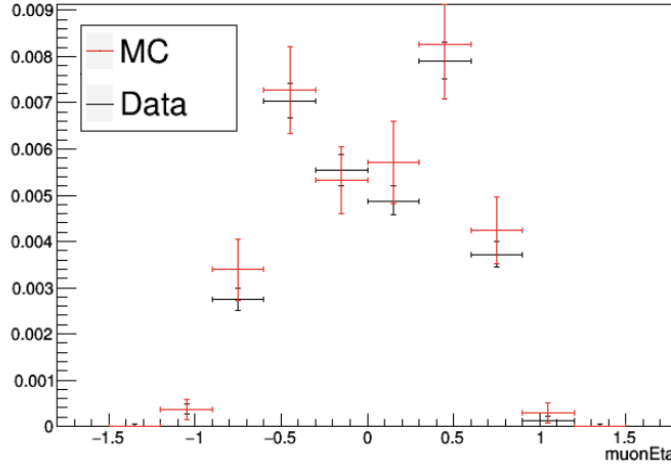


Figure 40: Clustering efficiency as a function of probe muon η for data and MC. There is no observed η -dependent difference between data and MC.

741 probe muon. As seen, the η dependence is modeled well, so there is no systematic uncertainty
 742 related to the cluster η necessary.

743 The RPC match requirement can be removed so that it may be studied as well. Figure 41 shows
 744 the fraction of clusters that match to at least one RPC rechit for data and MC. The difference
 745 in the second bin was used to correct signal efficiency by applying a correction factor of
 746 0.907 ± 0.048 to signal MC.

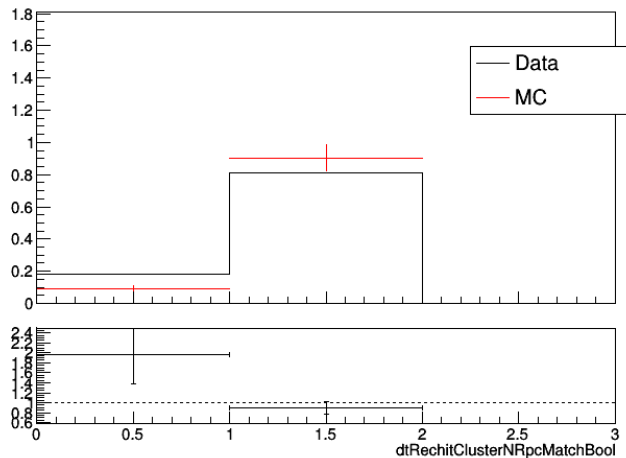


Figure 41: Histogram showing fraction of clusters in data and MC in the muon bremsstrahlung selection which pass the MB1 veto that also pass the RPC match requirement. The second bin shows the clusters that match to at least one RPC rechit, and the difference between data and MC is used to correct signal efficiency and derive an uncertainty.

747 8.1.2 Cluster size modeling

748 After identifying clusters coming from muon bremsstrahlung, they can be used to study any
 749 differences between data and MC modeling. Perhaps the most important cluster feature that
 750 can be studied is the size of the clusters because that is one of the two variables used for back-
 751 ground prediction. The MC and data distributions have some disagreement (see Figure 42)
 752 which could impact the analysis because size mis-modeling of clusters with around 100 rechits

753 will move events into different ABCD regions, ultimately affecting the prediction and signal
 754 yield.

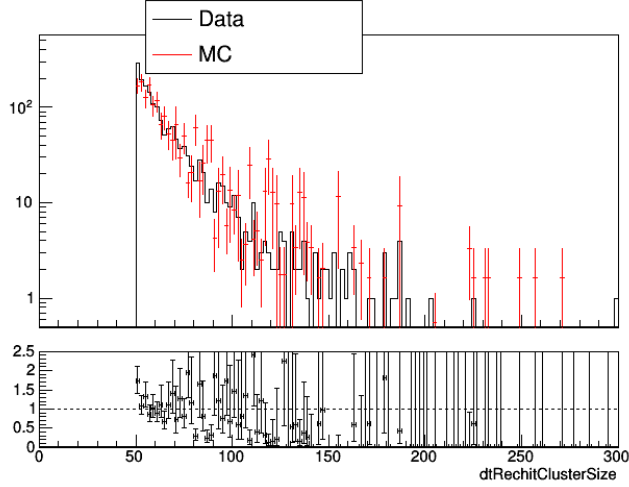


Figure 42: Cluster size distributions for MC and data in the muon bremsstrahlung selection. MC does not match the data perfectly. While 13.0% of MC clusters have 100 or more rechits, only 6.7% of data clusters do.

755 To study the impact of this difference, the difference in distribution shapes is turned into an
 756 uncertainty to cover the extent to which MC modeling affects signal efficiency. Of the clusters
 757 in data, 6.7% have 100 or more rechits, while 13.0% of MC clusters do. For a threshold of 100
 758 rechits in data, MC matches the efficiency with 122 rechits. Conversely, for a threshold of 100
 759 rechits in MC, data matches the efficiency with 82 rechits. The discrepancy corresponds to
 760 about a 20 rehit difference in cluster size. To see the effect of a roughly 20 rehit mis-modeling
 761 in MC (Figure 43 shows the cluster size distributions for 1 and 10m signal models), signal
 762 yields are calculated for thresholds of 82, 100, and 122 rechits, as seen in Table 14. Overall, a
 763 15% uncertainty on cluster size covers the signal efficiency difference from possible MC mis-
 764 modeling.

765 The difference between cluster sizes in different MB stations is smaller than this overall cluster
 766 size effect, so only one uncertainty is derived and only one cluster size signal region cut is used.

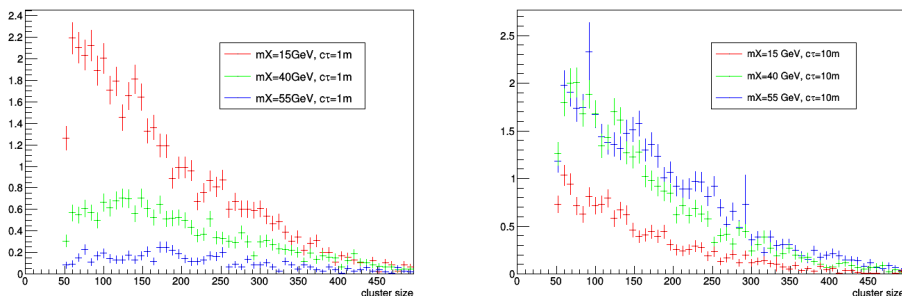


Figure 43: Cluster size distributions for 1m (left) and 10m (right) proper lifetime signal models.

767 8.1.3 Other cluster feature modeling

768 The muon bremsstrahlung selection can be used to validate the modeling of other cluster prop-
 769 erties used for the signal region selection.

Table 14: Changes in signal yield for different cluster size thresholds

Signal model	≥ 82 (% change)	≥ 100	≥ 122 (% change)
15 GeV, 1m	27.78 (+13%)	24.48	20.79 (-15%)
15 GeV, 10m	8.62 (+15%)	7.47	6.12 (-18%)
40 GeV, 1m	13.23 (+8%)	12.22	10.75 (-12%)
40 GeV, 10m	21.33 (+17%)	18.30	15.17 (-17%)
55 GeV, 1m	3.95 (+6%)	3.73	3.36 (-10%)
55 GeV, 10m	25.54 (+15%)	22.22	19.14 (-14%)

770 Figure 44 shows the station with the most DT rechits in a cluster for data and MC. The MC
 771 modeling of where clusters form that pass this selection matches the data, so no systematic
 772 uncertainty related to the cluster station is derived.

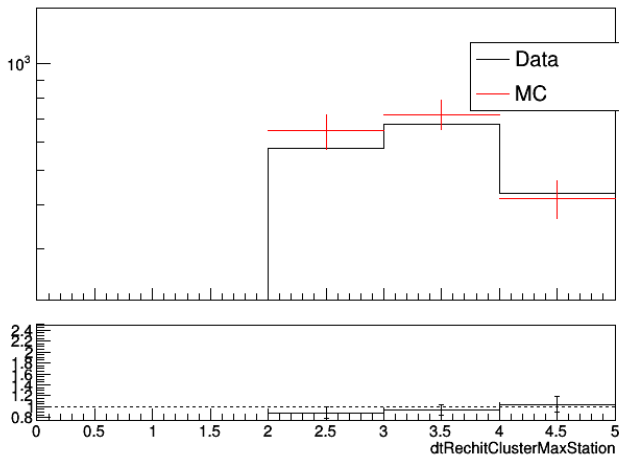


Figure 44: Distribution of MB station with the most DT rechits in clusters matched to probe muons in the muon bremsstrahlung selection for data and MC. This property is modeled well in MC so no associated uncertainty is required.

773 This selection is also used to measure the rate of clusters overlapping with random jets, leading
 774 to an inefficiency in the jet veto. The random jet overlap is measured by choosing a random
 775 section of the MB system by selecting an η, ϕ position from the distributions of signal clusters.
 776 If this randomly chosen section of the detector overlaps with a jet that would veto a cluster in
 777 this position, the second bin of the plot in Figure 45 is filled, otherwise the first bin is filled.
 778 This random overlap inefficiency is 4% in both data and MC. In the same way, the rate of
 779 overlapping with loose ID muons is measured in data and MC. The result is shown in Figure 46,
 780 with about 1% of clusters in both data and MC randomly overlapping with a muon.

781 Similarly, the MB1 and MB2 vetoes can be studied with these events. If a cluster randomly
 782 overlaps with 2 or more MB1 or MB2 rechits, it will be vetoed, and any difference between
 783 MC and data will lead to mismodeled signal efficiency. Using the same method as the jet and
 784 muon studies to select a random part of the detector, the number of matched MB1 rechits at
 785 that location are counted and plotted in Figure 47. The first two bins represent events with
 786 clusters that would pass the MB1 veto, while clusters that match to 2 or more random MB1

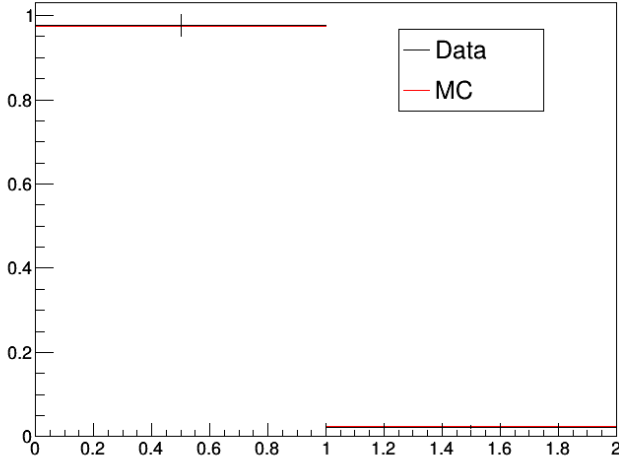


Figure 45: Comparison of the jet veto inefficiency in data and MC due to overlap with random jets. The rate of a cluster overlapping with a random jet is measured by choosing a random part of the MB system using a random η, ϕ from the signal DT cluster distributions. If there is a jet that would veto a cluster in that location, the second bin is filled. If not, the first is filled. The rate of random jet overlap is measured to be 4% in both data and MC.

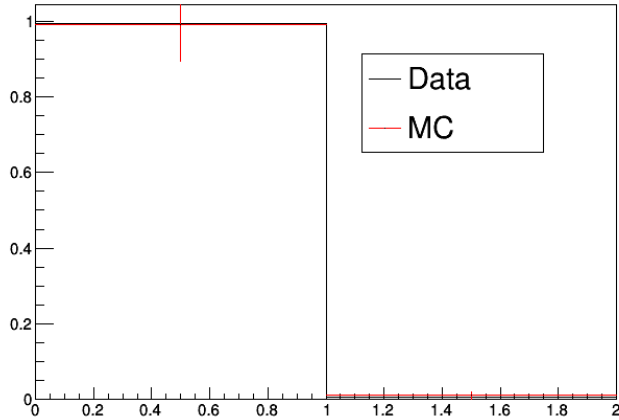


Figure 46: Comparison of the muon veto inefficiency in data and MC due to overlap with random muons. The rate of a cluster overlapping with a random muon is measured by choosing a random part of the MB system using a random η, ϕ from the signal DT cluster distributions. If there is a muon that would veto a cluster in that location, the second bin is filled. If not, the first is filled. The rate of random muon overlap is measured to be 1% in both data and MC.

787 rechits would be vetoed. The difference in the MC and data distributions was used to correct
 788 signal efficiency, by applying a correction factor of 0.932 ± 0.069 to signal MC. The same is
 789 done to make the distributions of matched MB2 hits in Figure 48, binned to show clearly the
 790 rate of passing or failing the veto, which shows better agreement than the MB1 noise, and no
 791 correction is applied.

792 Similarly, MB1 and MB2 rechits can veto clusters in adjacent wheels. The data and MC distri-
 793 butions for the number of MB1 and MB2 rechits in a $\Delta R < 0.8$ cone are shown in Fig 49. MB1
 794 shows more noise than MB2 and more noise in data than MC, similar to the check using the

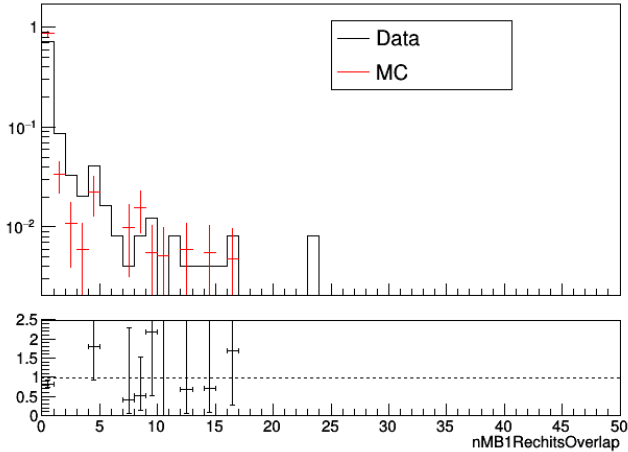


Figure 47: Histogram showing number of MB1 rechits that would be randomly matched to clusters in data and MC in the muon bremsstrahlung selection. Clusters matched to 2 or more of these random MB1 rechits would be vetoed. The difference between data and MC is used to correct signal efficiency and derive an uncertainty.

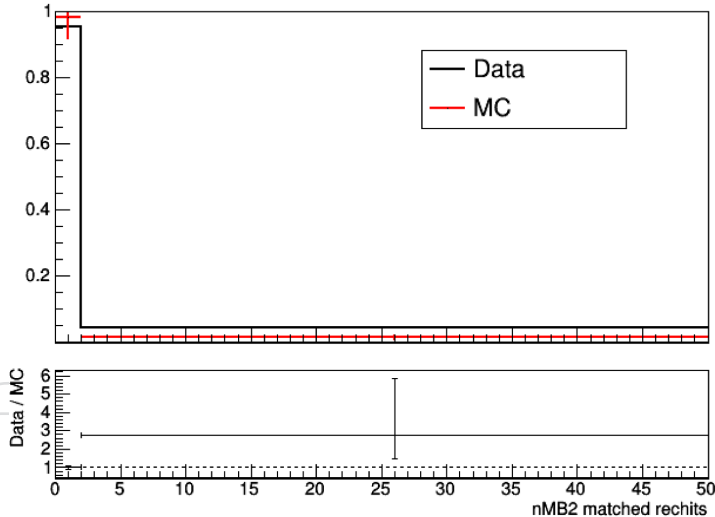


Figure 48: Histogram showing number of MB2 rechits that would be randomly matched to clusters in data and MC in the muon bremsstrahlung selection. Clusters matched to 2 or more of these random MB2 rechits (the second bin) would be vetoed. No uncertainty is applied from these distributions.

795 smaller cone used for the other MB1 veto. MB2 shows agreement between the data and MC
 796 again. The MC correction factor from the MB1 difference is 0.910 ± 0.075 .

797 8.2 Event level modeling

798 The muon bremsstrahlung selection is used to validate the modeling of the number of DT
 799 segments veto. The selection gives clean events, and outside the $\Delta R = 0.4$ cone around the
 800 muon and cluster, the expected number of segments in the detector can be compared between
 801 data and MC. Figure 50 shows the number of DT segments in the top half of the detector that
 802 are $\Delta R > 0.4$ from the cluster. This gives a measure of the noise in both data and MC. The noise
 803 behavior is slightly different in data and MC, as seen in the different shapes at low number of

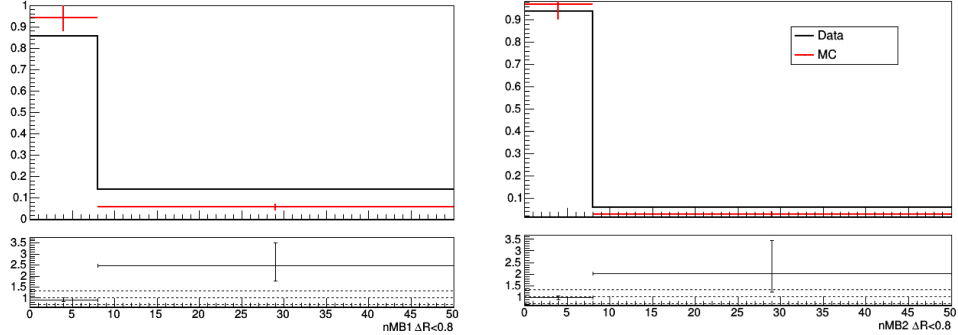


Figure 49: Histogram showing number of MB1 (left) and MB2 (right) rechits that would be randomly matched to adjacent wheel clusters in data and MC in the muon bremsstrahlung selection. Clusters matched to more than 8 of these random rechits in an adjacent wheel (the second bin) would be vetoed. The difference in MB1 modeling is used to derive a correction factor.

804 segments. However, at the large thresholds used for the veto, the two agree on the rate of noise
805 causing more than 14 segments in one hemisphere.

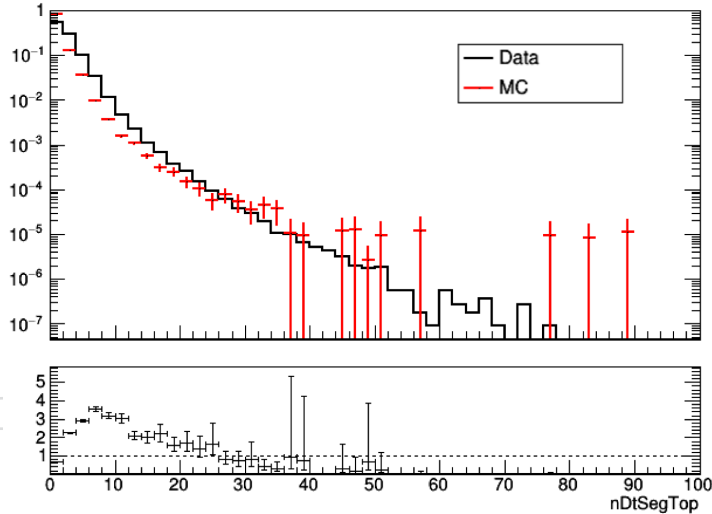


Figure 50: Histogram showing number of DT segments in data and MC in the top half of the detector, only counting segments separated from the muon and cluster. These noise segments could veto the event if there are more than 14. At this high threshold, the data and MC agree on the rate of noise inefficiency, and no systematic uncertainty is derived.

806 Additionally, Figure 51 shows the number of segments in the top half for events where there
807 are more than 10 segments in the bottom half, separated into one bin below 10 and one bin
808 above 10. The data and MC agree well on the rate of noise fluctuating above 10 segments in the
809 top hemisphere when there are also 10 segments in the bottom hemisphere, which would cause
810 the event to be vetoed. This measurement and the measurement of one hemisphere fluctuating
811 above 14 segments agree well between data and MC, so no systematic uncertainty is required.

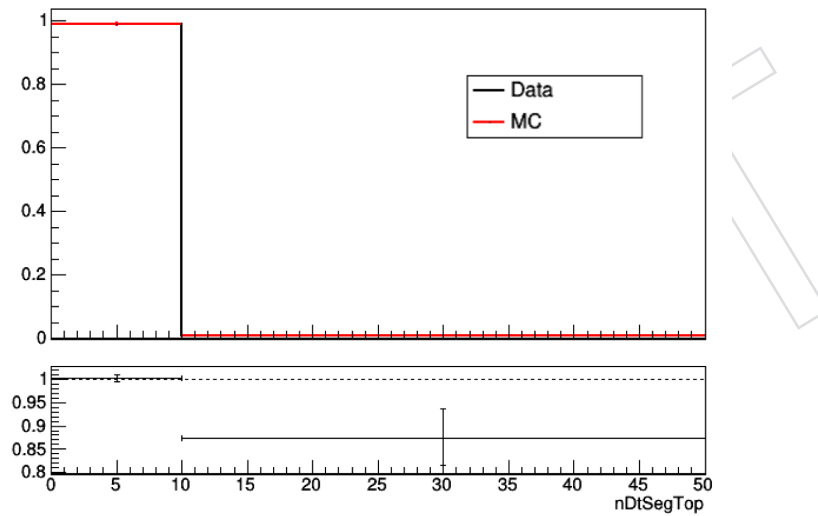


Figure 51: Histogram showing number of DT segments in data and MC in the top half of the detector, only counting segments separated from the muon and cluster, for events where there are more than 10 segments in the bottom half. These noise segments could veto the event if there are more than 10. At this high threshold, the data and MC agree on the rate of noise inefficiency, and no systematic uncertainty is derived.

812 **9 Uncertainties**

813 **9.1 Background uncertainties**

814 Since the validation tests done in Section 7 showed good agreement for the background, there
 815 is no systematic uncertainty assigned to the signal region prediction. The uncertainty on the
 816 random background comes from the statistical uncertainty on the observed number of events
 817 in regions A, B, and C. The uncertainty on the correlated background comes from the statistical
 818 uncertainty on the number of events in the inverted MB1 veto region used to make the signal
 819 region prediction.

820 **9.2 Signal uncertainties**

821 The total systematic uncertainty on the signal efficiency is given by the uncertainties described
 822 in Section 8 as well as uncertainties from pileup reweighting, luminosity, jet energy scale, and
 823 Higgs p_T reweighting. These uncertainties are discussed in the following sections. The studies
 824 are not complete for all sources of uncertainty but will be updated for the next iteration and
 825 new expected results will be generated with the complete list of uncertainties.

826 **9.2.1 DT cluster modeling**

827 The cluster modeling uncertainty is taken from the studies in Section 8. The dominant source
 828 of uncertainty is the 15% cluster size systematic uncertainty.

829 **9.2.2 Pileup reweighting**

830 The uncertainty from the pileup reweighting is estimated by measuring the effect of a one
 831 sigma variation up and down in the pp inelastic cross section on the signal yield. The size
 832 of this systematic uncertainty is 1.3% and is independent of the signal model and consistent
 833 between the two signal regions.

834 **9.2.3 Luminosity**

835 A 1.6% luminosity is taken for each year, as is recommended by the Luminosity Physics Object
 836 Group.

837 **9.2.4 Jet Energy Scale**

838 The uncertainty from varying the jet energy scale is about 3-10%, depending on the signal
 839 model. The jet energy scale affects the analysis mainly through the E_T^{miss} calculation, and also
 840 through the p_T of jets used for the jet veto and leading jet requirement.

841 **9.2.5 Signal cross section**

842 The uncertainties on the theoretical cross sections are taken from the LHC Higgs Cross Section
 843 Working Group for each production mode. The uncertainty for ggH is -6.7% / +4.6%, -0.3%
 844 / +0.4% for VBF, -0.7% / +0.5% for WH, -0.6% / +0.5% for qqZH, -18.9% / +25.1% for ggZH,
 845 and -9.2% / +5.8% for ttH.

846 **9.2.6 Parton distribution functions and strong coupling constant**

847 The uncertainties on the parton distribution function and strong coupling constant are taken
 848 from the LHC Higgs Cross Section Working Group for each production mode. The uncertainty
 849 is 3.2% for ggH, 2.1% for VBF, 1.9% for WH, 1.9% for qqZH, 2.4% for ggZH, and 3.6% for ttH.

850 **9.2.7 Higgs p_T reweighting**

851 The systematic uncertainty due to the Higgs p_T reweighting is estimated by changing the fac-
852 torization and renormalization scales up and down by a factor of 2 and measuring the change
853 in signal yield. Halving the factorization scale leads to an 18% change in yield, while halv-
854 ing the renormalization scale gives a 7.5% change. When both are halved together, the total
855 change is about 11%. These changes are independent of signal model and signal region. When
856 the scales are doubled, the measured changes in signal yield are 7%, 3%, and 11% for factor-
857 ization, renormalization, and both scales, respectively. Following the prescription used by the
858 CSC cluster analysis, these uncertainties are added in quadrature to determine a single double-
859 sided systematic uncertainty due to the Higgs p_T reweighting uncertainty. This systematic is
860 then -13% / +23%.

861 **9.2.8 Monte Carlo statistics**

862 The uncertainty due to the number of Monte Carlo events used to measure the signal yield is
863 typically around 5-10% but can be larger for some models depending on the acceptance. This
864 uncertainty is calculated individually for each ABCD region for all signal models considered.

DRAFT

865 10 Results

866 After validating the ABCD method for predicting random background and predicting the cor-
 867 related punch-through background in Section 7, the method is applied to the signal region.
 868 The predictions for the two signal regions are shown in Table 15 and Table 16. The expected
 869 background decreases with increasing station number. The uncorrelated background ranges
 870 from 3.2 ± 1.5 in MB2 to 0.0 ± 1.3 in MB4, while the punch-through background ranges from
 871 6.5 ± 2.1 in MB2 to 0.8 ± 0.9 in MB4. This section will be updated with the observation once the
 872 search is unblinded.

Table 15: Signal region ABCD prediction.

Cluster station	A	B	C	D (ABC pred.)
MB2	119	5	77	3.2 ± 1.5
MB3	6	1	8	$1.3^{+1.5}_{-1.3}$
MB4		0		$0.0^{+1.3}_{-0.0}$

Table 16: Signal region punch-through prediction.

Cluster station	MB1 veto eff.	MB1 pass/fail ratio	Inverted MB1 events	SR punch-through pred.
MB2	0.225 ± 0.020	0.290 ± 0.033	22.4 ± 6.8	6.5 ± 2.1
MB3	0.376 ± 0.070	0.603 ± 0.180	7.4 ± 2.9	4.4 ± 2.2
MB4	0.286 ± 0.135	0.401 ± 0.265	2.0 ± 1.7	$0.8^{+0.9}_{-0.8}$

873 11 Interpretation

874 This section details the efficiency for both the Twin Higgs and Dark Shower signal models and
 875 presents the expected limits on the Higgs boson branching ratio.

876 11.1 Signal Efficiency

877 11.1.1 Twin Higgs Model

878 For the Twin Higgs model, the overall signal efficiency as a function of radius and z position
 879 given a cluster was formed from a decay at the plotted position are shown in Figure 52 and
 880 Figure 53. Signal efficiency is highest for decays right before DT stations, allowing the full
 881 shower to form and leave hits in DTs and RPCs. Efficiency is also flat as a function of z, except
 882 for dips in efficiency between the Barrel Muon System wheels. The expected signal yield is
 883 shown in Table 17 for a selection of masses and lifetimes, assuming $\text{BR}(\text{H} \rightarrow \text{ss}) = 1\%$. The
 884 expected signal yields are fairly evenly spread cross the three signal regions corresponding to
 885 different DT stations. Yields in individual search regions range from about 1 to 10 events.

886 Table 18 shows the efficiency of all the signal region selections for a subset of the Twin Higgs
 887 signal samples.

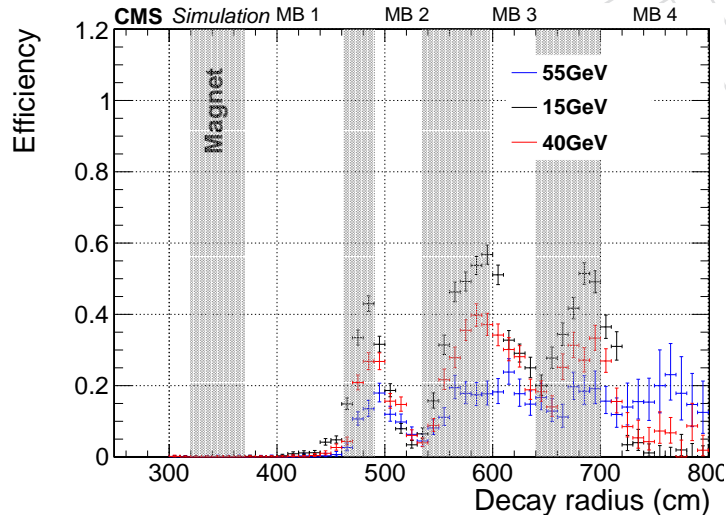


Figure 52: Signal efficiency assuming a decay at the plotted radius formed a DT cluster. The peaks of efficiency are when the decay is right at the start of a DT station.

888 11.1.2 Dark Shower Model

889 The expected signal yields are shown in Table 19 through Table 23 for a selection of masses
 890 and lifetimes, assuming $\text{BR}(\text{H} \rightarrow \text{ss}) = 1\%$. Table 24 through Table 28 also show the efficiency
 891 for all signal region cuts for each of the Dark Shower portals for a subset of long-lived particle
 892 mass and lifetime. For all portals except the vector, efficiencies are shown for two different
 893 hierarchies, $(x_{i\Omega}, x_{i\Lambda}) = (1, 1)$ and $(2.5, 2.5)$.

894 The efficiencies are typically higher for $(1, 1)$ than $(2.5, 2.5)$ as the E_T^{miss} in the final state is
 895 increased due to the presence of stable dark vector mesons. The reduced visible content of
 896 the Dark Shower also leads to a reduced probability of having decays occur before the cluster,
 897 which can cause the cluster to fail the jet, muon and MB1 vetoes. The efficiency for the dark
 898 photon is significantly lower than for the other portals. In the case of the dark photon, the dark
 899 scalar decays promptly to a pair of vector mediators (as detailed in Section 3.2). The vector

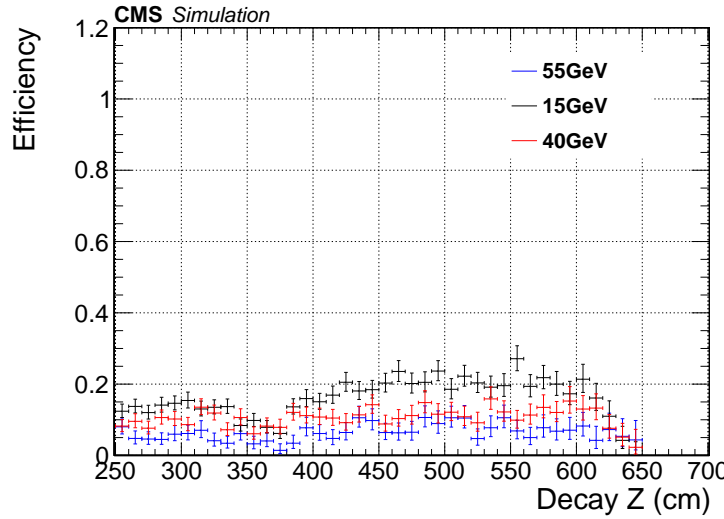


Figure 53: Signal efficiency assuming a decay at the plotted z position formed a DT cluster. The efficiency is flat as a function of z except when they decay occurs in the gaps between wheels.

Table 17: Expected signal yield in signal regions for the Twin Higgs signal model.

Cluster station		0.1m	1m	10m	100m
MB2	15 GeV	1.5	11.2	3.5	0.4
	40 GeV	0.0	5.9	10.3	1.6
	55 GeV	0.0	1.9	12.6	2.0
MB3	15 GeV	2.0	15.2	4.8	0.7
	40 GeV	0.02	7.4	13.1	1.9
	55 GeV	0.0	2.0	16.4	2.7
MB4	15 GeV	1.8	12.5	3.8	0.4
	40 GeV	0.0	5.2	9.5	1.7
	55 GeV	0.0	1.2	10.9	2.1

mediators then undergo displaced decays back to the Standard Model. The visible energy is therefore split among double the number of particles compared to the other portals. The reduction of energy available for each decay means the dark photon mediator has the lowest efficiency to produce any DT clusters. Even when clusters are formed, a higher percentage are vetoed compared to other portals. This is because there is a significantly higher probability of decays occurring before the cluster. Therefore the cluster is substantially more likely to be rejected by the jet, muon and MB1 vetoes.

11.2 Likelihood model

The analysis relies on the ABCD method to predict the uncorrelated background in each of the signal regions (MB2, MB3, and MB4). The likelihood model can be split into signal and control regions linked by floating parameters for the prediction. This can be written concisely as

Table 18: Signal efficiency (%) for each cut for Twin Higgs models with a long-lived particle with a mass of 15 GeV and 55 GeV and lifetimes of 0.1m, 1m and 10m for the 4b final state from ggH production. The cuts are made sequentially, and the reported efficiency is with all previous cuts applied, except for the final three lines which show the percentage of events in the three signal regions. The overall efficiency relative to the first line is included in parentheses. The first line is the percentage of ggH production (48.58 fb^{-1}) events that pass the MET requirements.

Selection	15 GeV			55 GeV		
	0.1m	1m	10m	0.1m	1m	10m
$E_T^{\text{miss}} > 200$, E_T^{miss} filters, HLT	0.183	1.05	1.48	0.00679	0.314	1.24
$N_{\text{jets}} > 0$	99.7 (99.7)	99.6 (99.6)	99.6 (99.6)	100 (100)	99.8 (99.8)	99.6 (99.6)
$\min \Delta\phi(\text{jet}, \bar{E}_T^{\text{miss}}) > 0.6$	66 (65.8)	85 (84.6)	90.5 (90.1)	7.47 (7.47)	52.6 (52.5)	87.7 (87.4)
$N_{\text{clusters}} > 0$	43.6 (28.7)	26.9 (22.8)	6.62 (5.96)	2.22 (0.166)	38.0 (20.0)	17.0 (14.9)
$N_{\text{DT segments}} \text{ veto}$	98.1 (28.1)	93.9 (21.4)	97.6 (5.82)	100 (0.166)	89.7 (17.9)	96.4 (14.3)
Leading jet pass ID	100 (28.1)	100 (21.4)	100 (5.82)	100 (0.166)	100 (17.9)	100 (14.3)
Jet veto	88.5 (24.9)	88 (18.8)	76.6 (4.46)	0 (0)	83.8 (15)	87.7 (12.6)
Muon veto	100 (24.9)	100 (18.8)	100 (4.46)	–	99.9 (15)	100 (12.6)
MB1/MB2 vetoes	17.2 (4.3)	34.4 (6.47)	40 (1.78)	–	18.5 (2.78)	41.5 (5.21)
RPC Match	84.2 (3.62)	86.6 (5.6)	86.9 (1.55)	–	84.5 (2.35)	86.4 (4.51)
Adjacent MB1/MB2 vetoes	94.3 (3.42)	95.4 (5.35)	97.2 (1.5)	–	88.2 (2.07)	97.1 (4.38)
$ \Delta\phi(\text{cluster}, \bar{E}_T^{\text{miss}}) < 1.0$	100 (3.42)	96.8 (5.18)	82.6 (1.24)	–	100 (2.07)	100 (4.38)
$N_{\text{rechits}} \geq 100$	84.7 (2.89)	71.4 (3.7)	66 (0.822)	–	84.7 (1.76)	73.9 (3.24)
CSC/Combination veto	97.1 (2.81)	98.6 (3.65)	95.9 (0.788)	–	98.1 (1.72)	99.7 (3.23)
MB2	25.7	29.2	28.8	–	36.1	32.6
MB3	37.1	39.1	41.2	–	38.9	40.4
MB4	37.1	31.6	30.0	–	25.0	27.0

Table 19: Expected signal yield in signal regions for the gluon portal Dark Shower model.

Station	1m			10m			100m		
	(1.0, 1.0)	(2.5, 1.0)	(2.5, 2.5)	(1.0, 1.0)	(2.5, 1.0)	(2.5, 2.5)	(1.0, 1.0)	(2.5, 1.0)	(2.5, 2.5)
MB2	3 GeV	3.3	1.8	2.0	0.9	2.7	3.0	0.1	0.5
	10 GeV	4.3	2.4	3.4	2.2	7.1	6.3	0.3	1.4
	20 GeV	4.7	2.4	3.6	2.9	8.7	7.6	0.3	1.4
MB3	3 GeV	2.8	1.3	1.5	0.6	2.5	2.3	0.1	0.4
	10 GeV	4.1	1.9	3.2	2.6	6.9	6.3	0.2	1.2
	20 GeV	4.7	2.8	3.8	3.4	9.7	9.1	0.5	1.6
MB4	3 GeV	1.3	0.7	1.0	0.4	1.2	1.2	0.03	0.2
	10 GeV	2.4	1.3	2.1	1.2	3.1	3.7	0.1	0.5
	20 GeV	2.7	1.4	2.4	1.9	5.8	5.1	0.2	1.1

$$\mathcal{L} = \prod_i \text{Pois}(n_{\text{sig}}^i | \sum_i \frac{\beta^i \times \gamma^i}{\delta^i} \times +\psi^i \times \phi_{\text{sig}}^i + \rho^i \times r \times s_{\text{sig}}^i) \\ \times \text{Pois}(n_B^i | \beta^i + \rho_B^i \times r \times s_B^i) \times \text{Pois}(n_C^i | \gamma^i + \rho_C^i \times r \times s_C^i) \times \text{Pois}(n_D^i | \delta^i + \rho_D^i \times r \times s_D^i) \quad (1)$$

where the product is over the three signal regions (MB2, MB3, and MB4); n_{sig}^i is the observation in each signal region; n_B^i , n_C^i and n_D^i are the observations in the B, C and D control regions respectively; β^i , γ^i and δ^i are unconstrained parameters in each of the B, C and D control regions; ψ^i is the background contribution from correlated sources; ϕ^i contains the systematic

Table 20: Expected signal yield in signal regions for the photon portal Dark Shower model.

Station	1m			10m			100m			
	(1.0, 1.0)	(2.5, 1.0)	(2.5, 2.5)	(1.0, 1.0)	(2.5, 1.0)	(2.5, 2.5)	(1.0, 1.0)	(2.5, 1.0)	(2.5, 2.5)	
MB2	2 GeV	3.5	2.3	2.7	1.2	3.4	3.3	0.2	0.7	0.7
	10 GeV	4.4	3.0	4.4	2.0	6.2	5.8	0.3	0.9	1.1
	20 GeV	5.4	3.1	4.3	2.9	7.1	6.8	0.3	1.5	0.9
MB3	2 GeV	2.4	1.2	1.7	0.9	2.5	2.6	0.1	0.4	0.4
	10 GeV	2.3	1.2	2.0	1.3	4.3	4.1	0.3	0.8	0.7
	20 GeV	2.1	1.3	2.0	1.7	4.7	4.2	0.2	0.7	0.7
MB4	2 GeV	1.7	0.8	1.1	0.6	1.2	1.5	0.1	0.2	0.2
	10 GeV	1.9	0.9	1.5	1.2	3.0	3.7	0.1	0.6	0.4
	20 GeV	1.5	0.8	1.1	1.4	4.1	3.6	0.2	0.7	0.7

Table 21: Expected signal yield in signal regions for the vector portal Dark Shower model.

Station	0.1m				
	(1.0, 1.0)	(1.0, 1.0)	(1.0, 1.0)	(1.0, 1.0)	
MB2	2 GeV	0.2	1.6	1.5	0.2
	10 GeV	0.2	2.7	3.5	0.7
	20 GeV	0.1	3.2	4.6	0.8
MB3	2 GeV	0.2	1.0	1.0	0.1
	10 GeV	0.1	2.1	3.5	0.6
	20 GeV	0.03	3.0	4.9	1.0
MB4	2 GeV	0.1	0.7	0.5	0.1
	10 GeV	0.1	1.6	2.1	0.4
	20 GeV	0.04	2.1	3.0	0.5

Table 22: Expected signal yield in signal regions for the Higgs portal Dark Shower model.

Station	1m			10m			100m			
	(1.0, 1.0)	(2.5, 1.0)	(2.5, 2.5)	(1.0, 1.0)	(2.5, 1.0)	(2.5, 2.5)	(1.0, 1.0)	(2.5, 1.0)	(2.5, 2.5)	
MB2	4 GeV	2.9	1.7	2.2	1.0	2.8	3.0	0.05	0.4	0.4
	10 GeV	3.3	2.2	3.3	1.6	4.7	4.3	0.2	0.7	0.7
	20 GeV	3.6	2.3	3.5	2.5	7.5	6.1	0.3	1.4	1.2
MB3	4 GeV	2.5	1.4	1.8	0.9	2.3	2.4	0.2	0.5	0.5
	10 GeV	2.8	2.0	3.1	1.4	4.3	4.2	0.2	0.8	0.7
	20 GeV	3.9	2.5	3.6	2.6	8.2	7.2	0.4	1.8	1.0
MB4	4 GeV	1.4	0.9	1.1	0.5	1.2	1.1	0.04	0.2	0.2
	10 GeV	1.7	1.4	1.8	0.8	2.4	2.4	0.1	0.5	0.4
	20 GeV	2.3	1.4	2.1	1.6	4.5	4.5	0.2	1.0	0.6

uncertainties in the correlated background prediction discussed in Section 7; s is the signal yield taken from simulation; ρ contains the relevant systematic uncertainties in the signal yield discussed in Section 8 and r is the unconstrained signal strength. The uncertainties on the background prediction and signal yields are modeled using ‘log normal’ uncertainties such that the

Table 23: Expected signal yield in signal regions for the dark photon portal Dark Shower model.

Station	1m			10m			100m		
	(1.0, 1.0)	(2.5, 1.0)	(2.5, 2.5)	(1.0, 1.0)	(2.5, 1.0)	(2.5, 2.5)	(1.0, 1.0)	(2.5, 1.0)	(2.5, 2.5)
MB2	2 GeV	0.01	0.0	0.0	0.0	0.0	0.0	0.0	0.01
	10 GeV	0.6	0.04	0.1	0.3	0.3	0.4	0.1	0.2
	20 GeV	0.8	0.1	0.2	0.5	0.5	0.7	0.1	0.2
MB3	2 GeV	0.0	0.0	0.0	0.0	0.0	0.0	0.0	0.0
	10 GeV	0.6	0.01	0.1	0.4	0.2	0.3	0.1	0.2
	20 GeV	0.8	0.1	0.3	0.5	0.5	0.6	0.2	0.4
MB4	2 GeV	0.0	0.0	0.0	0.0	0.0	0.0	0.0	0.0
	10 GeV	0.4	0.03	0.1	0.2	0.1	0.2	0.02	0.1
	20 GeV	0.4	0.03	0.1	0.3	0.3	0.2	0.1	0.1

Table 24: Signal efficiency (%) for each cut for gluon portal Dark Shower models with a long-lived particle with various masses, lifetimes, and dark sector mass hierarchies. The cuts are made sequentially, and the reported efficiency is with all previous cuts applied, except for the final three lines which show the percentage of events in the three signal regions. The overall efficiency relative to the first line is included in parentheses.

Selection	5 GeV				15 GeV			
	0.5m		5m		0.5m		5m	
	(1.0, 1.0)	(2.5, 2.5)	(1.0, 1.0)	(2.5, 2.5)	(1.0, 1.0)	(2.5, 2.5)	(1.0, 1.0)	(2.5, 2.5)
$E_T^{\text{miss}} > 200$, E_T^{miss} filters, HLTT	1.1	0.47	1.36	1.21	1.04	0.389	1.36	1.15
$N_{\text{jets}} > 0$	99.6 (99.6)	99.8 (99.8)	99.5 (99.5)	99.6 (99.6)	99.6 (99.6)	99.8 (99.8)	99.6 (99.6)	99.6 (99.6)
$\min \Delta\phi(\text{jet}, \vec{E}_T^{\text{miss}}) > 0.6$	76.3 (76)	40.4 (40.3)	89.8 (89.4)	82.8 (82.5)	75.3 (75)	45.2 (45.1)	88.3 (88)	81.1 (80.8)
$N_{\text{clusters}} > 0$	14.0 (10.6)	36.1 (14.5)	8.1 (7.2)	23.3 (19.2)	10.4 (7.8)	34.7 (15.7)	8.37 (7.37)	23.9 (19.3)
$N_{\text{DT segments}} \text{ veto}$	96.0 (10.2)	87.7 (12.8)	95.3 (6.9)	89.7 (17.3)	99.6 (7.62)	91.7 (14.4)	96.4 (7.1)	93.2 (18)
Leading jet pass ID	100 (10.2)	100 (12.8)	100 (6.9)	100 (17.3)	100 (7.62)	100 (14.4)	100 (7.1)	100 (18)
Jet veto	71.3 (7.3)	61.2 (7.81)	77.9 (5.38)	80.4 (13.9)	78.1 (5.95)	70.7 (10.1)	82 (5.83)	86.3 (15.5)
Muon veto	100 (7.3)	100 (7.8)	100 (5.38)	100 (13.9)	99.9 (5.95)	100 (10.1)	100 (5.82)	100 (15.5)
MB1/MB2 vetoes	26 (1.9)	20.3 (1.58)	33.7 (1.82)	29.9 (4.16)	25.7 (1.53)	23.3 (2.37)	37.1 (2.16)	36 (5.59)
RPC Match	88.3 (1.67)	88.7 (1.41)	87.6 (1.6)	87 (3.61)	88.3 (1.35)	87.3 (2.06)	87.3 (1.89)	86.9 (4.85)
Adjacent MB1/MB2 vetoes	95.7 (1.61)	89.7 (1.26)	94.1 (1.5)	92.1 (3.33)	95.6 (1.28)	92.6 (1.91)	96.2 (1.81)	94.8 (4.61)
$ \Delta\phi(\text{cluster}, \vec{E}_T^{\text{miss}}) < 1.0$	98.3 (1.58)	98.8 (1.25)	97 (1.45)	95.5 (3.18)	99.8 (1.28)	99.7 (1.9)	97.6 (1.77)	96 (4.42)
$N_{\text{rechits}} \geq 100$	54.5 (0.862)	60.4 (0.754)	33.9 (0.493)	40.1 (1.28)	71.7 (0.921)	75.5 (1.44)	57.3 (1.01)	58.9 (2.6)
CSC/Combination veto	95.8 (0.826)	99.2 (0.748)	96.3 (0.475)	98.8 (1.26)	99.1 (0.913)	99.2 (1.43)	99.7 (1.01)	99.9 (2.6)
MB2	40.3	40.8	40.7	42.0	40.0	30.8	37.2	38.2
MB3	36.3	31.5	40.0	37.0	37.2	39.4	38.7	38.7
MB4	23.3	27.7	19.3	20.9	23.2	29.8	24.1	23.2

logarithm of the variable has a Gaussian (normal) constraint.

11.3 Expected Limits

The expected asymptotic limits on the Higgs branching ratio are computed using the reported signal yields and background prediction. The full set of signal systematic uncertainties are described in Section 9 and are accounted for in the limits. The signal contamination in the ABC regions is also accounted for in the limit computation. Figure 54 shows the expected 95% upper limits on the branching ratio of the Higgs to the dark sector, assuming a 4 b final state. Figure 55 shows the same for the 4 d and 4 τ final states. The analysis is sensitive to a wide range of long-lived particle masses and proper lifetimes. For each mass, the lifetime with the optimal sensitivity has an expected limit on the Higgs branching ratio to long-lived particles of about a

Table 25: Signal efficiency (%) for each cut for photon portal Dark Shower models with a long-lived particle with various masses, lifetimes, and dark sector mass hierarchies. The cuts are made sequentially, and the reported efficiency is with all previous cuts applied, except for the final three lines which show the percentage of events in the three signal regions. The overall efficiency relative to the first line is included in parentheses.

Selection	2 GeV				15 GeV			
	0.5m		5m		0.5m		5m	
	(1.0, 1.0)	(2.5, 2.5)	(1.0, 1.0)	(2.5, 2.5)	(1.0, 1.0)	(2.5, 2.5)	(1.0, 1.0)	(2.5, 2.5)
$E_T^{\text{miss}} > 200$, E_T^{miss} filters, HLT	1.12	0.489	1.39	1.22	0.96	0.3	1.33	1.08
$N_{\text{jets}} > 0$	99.6 (99.6)	99.9 (99.9)	99.6 (99.6)	99.6 (99.6)	99.7 (99.7)	99.8 (99.8)	99.6 (99.6)	99.6 (99.6)
$\min \Delta\phi(\text{jet}, \vec{E}_T^{\text{miss}}) > 0.6$	79.6 (79.3)	40.5 (40.4)	90.8 (90.4)	85.5 (85.2)	74.9 (74.7)	39.7 (39.7)	88.4 (88)	81.4 (81.1)
$N_{\text{clusters}} > 0$	9.16 (7.26)	23.4 (9.45)	4.38 (3.96)	13.2 (11.2)	6.57 (4.91)	24.4 (9.69)	4.67 (4.11)	13.3 (10.8)
$N_{\text{DT segments veto}}$	97.4 (7.07)	94.7 (8.98)	96.4 (3.82)	95.3 (10.7)	98.2 (4.81)	97.5 (9.44)	97.8 (4.02)	97.1 (10.5)
Leading jet pass ID	100 (7.07)	100 (8.98)	100 (3.82)	100 (10.7)	100 (4.81)	100 (9.44)	100 (4.02)	100 (10.5)
Jet veto	64.8 (4.58)	46.7 (4.19)	70.3 (2.68)	73.7 (7.91)	77.7 (3.74)	71.2 (6.72)	75.5 (3.03)	85.5 (8.97)
Muon veto	100 (4.58)	100 (4.19)	99.9 (2.68)	100 (7.91)	100 (3.74)	100 (6.72)	100 (3.03)	100 (8.97)
MB1/MB2 vetoes	33.3 (1.53)	27.4 (1.15)	40.7 (1.09)	37.4 (2.95)	33.4 (1.25)	30.6 (2.06)	45.5 (1.38)	43 (3.86)
RPC Match	88.6 (1.35)	87.8 (1.01)	88.5 (0.972)	88.5 (2.61)	87.9 (1.1)	87.4 (1.81)	87 (1.2)	87.1 (3.36)
Adjacent MB1/MB2 vetoes	94.9 (1.28)	88.3 (0.888)	95 (0.921)	92.5 (2.42)	95.5 (1.05)	90.2 (1.62)	94.9 (1.14)	93.9 (3.15)
$ \Delta\phi(\text{cluster}, \vec{E}_T^{\text{miss}}) < 1.0$	97.2 (1.24)	95.6 (0.854)	94.5 (0.871)	94.5 (2.29)	99.5 (1.05)	100 (1.62)	97.7 (1.11)	96.2 (3.03)
$N_{\text{rechits}} \geq 100$	60.5 (0.753)	60.2 (0.511)	42.8 (0.372)	45.3 (1.04)	73.2 (0.765)	79 (1.28)	69.6 (0.774)	67.5 (2.05)
CSC/Combination veto	95.9 (0.722)	99.9 (0.511)	97.3 (0.362)	98.8 (1.03)	98.1 (0.75)	99.2 (1.27)	98.8 (0.765)	99.9 (0.505)
MB2	50.1	54.9	45.3	46.5	58.9	63.2	45.4	47.0
MB3	30.1	25.1	36.2	31.0	22.0	21.3	30.4	30.2
MB4	19.8	20.0	18.5	22.5	19.1	15.5	24.3	22.8

929 few tenths of a percent.

930 Additionally Figure 56 through Figure 60 show the expected 95% upper limits on the branching
931 ratio of the Higgs to the dark sector for the Dark Shower benchmarks. A wide range of portals,
932 masses and lifetimes are considered, with the search typically achieving an optimal expected
933 limit of about 1% or lower for all portals except for the dark photon. These results highlight the
934 unique sensitivity of the search to dark shower signatures, including in the case that the dark
935 mesons have masses as low as a few GeV and for electromagnetic showers in the muon system.

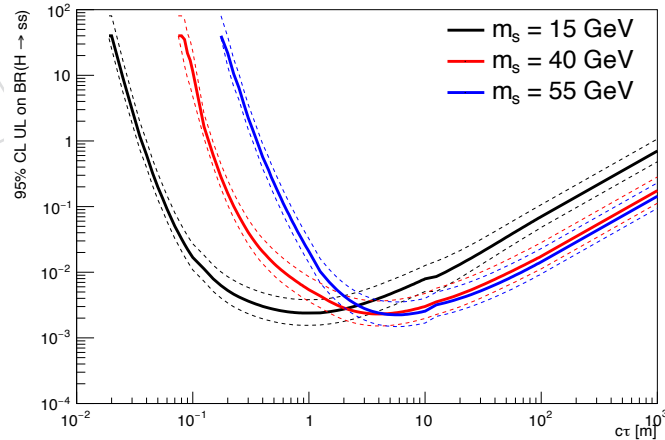


Figure 54: Expected limit on $\text{BR}(\text{H} \rightarrow \text{ss})$ for 4b final state given expected signal yields and background prediction.

Table 26: Signal efficiency (%) for each cut for vector portal Dark Shower models with a long-lived particle with various masses and lifetimes, with dark meson mass ratio of 1. The cuts are made sequentially, and the reported efficiency is with all previous cuts applied, except for the final three lines which show the percentage of events in the three signal regions. The overall efficiency relative to the first line is included in parentheses.

Selection	2 GeV		15 GeV	
	0.5m	5m	0.5m	5m
$E_T^{\text{miss}} > 200$, E_T^{miss} filters, HLT	0.77	1.3	0.521	1.2
$N_{\text{jets}} > 0$	99.7 (99.7)	99.6 (99.6)	99.8 (99.8)	99.6 (99.6)
$\min \Delta\phi(\text{jet}, \vec{E}_T^{\text{miss}}) > 0.6$	55.5 (55.4)	88.1 (87.7)	50 (49.9)	83 (82.7)
$N_{\text{clusters}} > 0$	32.8 (18.2)	14.9 (13.1)	26.9 (13.4)	18.0 (14.9)
$N_{\text{DT segments}} \text{ veto}$	87.1 (15.8)	92.5 (12.1)	93.9 (12.6)	94.2 (14.1)
Leading jet pass ID	100 (15.8)	100 (12.1)	100 (12.6)	100 (14.1)
Jet veto	47 (7.45)	74.2 (8.98)	70.9 (8.94)	83.5 (11.7)
Muon veto	100 (7.45)	99.9 (8.97)	99.8 (8.92)	100 (11.7)
MB1/MB2 vetoes	13.6 (1.02)	20.7 (1.85)	17.5 (1.57)	31.5 (3.7)
RPC Match	86.3 (0.871)	86.4 (1.61)	87.3 (1.36)	86.2 (3.19)
Adjacent MB1/MB2 vetoes	77.8 (0.68)	88.2 (1.41)	87.4 (1.19)	92.7 (2.95)
$ \Delta\phi(\text{cluster}, \vec{E}_T^{\text{miss}}) < 1.0$	94.9 (0.646)	95.5 (1.35)	99.7 (1.19)	97.4 (2.87)
$N_{\text{rechits}} \geq 100$	43.1 (0.279)	30.8 (0.416)	71.7 (0.853)	55.6 (1.6)
CSC/Combination veto	98 (0.273)	97.3 (0.405)	99.8 (0.852)	99.9 (1.6)
MB2	36.0	47.7	34.5	37.0
MB3	36.3	32.9	38.0	40.6
MB4	27.7	19.4	27.5	22.4

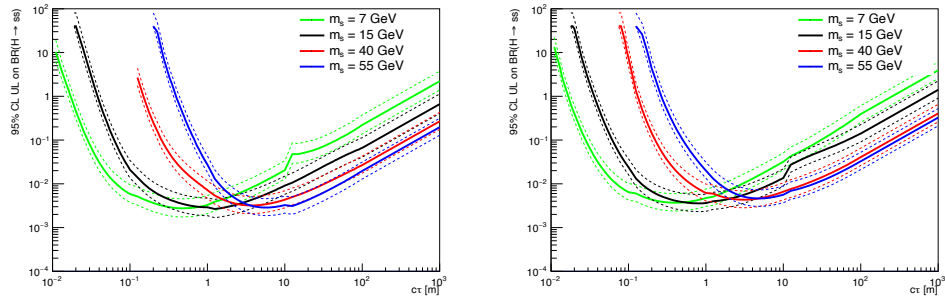


Figure 55: Expected limit on $\text{BR}(\text{H} \rightarrow \text{ss})$ for 4d (left) and 4 τ (right) final state given expected signal yields and background prediction.

Table 27: Signal efficiency (%) for each cut for Higgs portal Dark Shower models with a long-lived particle with various masses, lifetimes, and dark sector mass hierarchies. The cuts are made sequentially, and the reported efficiency is with all previous cuts applied, except for the final three lines which show the percentage of events in the three signal regions. The overall efficiency relative to the first line is included in parentheses.

Selection	4 GeV				15 GeV			
	0.5m		5m		0.5m		5m	
	(1.0, 1.0)	(2.5, 2.5)	(1.0, 1.0)	(2.5, 2.5)	(1.0, 1.0)	(2.5, 2.5)	(1.0, 1.0)	(2.5, 2.5)
$E_T^{\text{miss}} > 200$, E_T^{miss} filters, HLT	1.17	0.59	1.39	1.25	1.07	0.436	1.36	1.17
$N_{\text{jets}} > 0$	99.6 (99.6)	99.8 (99.8)	99.6 (99.6)	99.6 (99.6)	99.6 (99.6)	99.8 (99.8)	99.6 (99.6)	99.6 (99.6)
$\min \Delta\phi(\text{jet}, \vec{E}_T^{\text{miss}}) > 0.6$	79.6 (79.4)	45 (44.9)	90.2 (89.9)	85.1 (84.8)	76.6 (76.3)	46.5 (46.4)	88.7 (88.3)	82 (81.7)
$N_{\text{clusters}} > 0$	13.2 (10.5)	35.1 (15.8)	6.4 (5.75)	19.8 (16.8)	9.62 (7.34)	34.8 (16.1)	7.65 (6.75)	22.4 (18.3)
$N_{\text{DT segments veto}}$	95.9 (10)	88.6 (13.9)	95.1 (5.47)	90.5 (15.2)	97.0 (7.12)	91.8 (14.8)	96.6 (6.53)	93.6 (17.1)
Leading jet pass ID	100 (10)	100 (13.9)	100 (5.47)	100 (15.2)	100 (7.12)	100 (14.8)	100 (6.53)	100 (17.1)
Jet veto	70 (7.01)	57.2 (7.98)	75.3 (4.12)	77.4 (11.7)	77.5 (5.52)	68.9 (10.2)	79.4 (5.18)	84.7 (14.5)
Muon veto	100 (7.01)	99.9 (7.98)	99.9 (4.12)	100 (11.7)	99.9 (5.51)	100 (10.2)	100 (5.18)	100 (14.5)
MB1/MB2 vetoes	24.2 (1.7)	19 (1.52)	31.9 (1.31)	28.2 (3.31)	24.9 (1.37)	23.4 (2.39)	37.1 (1.92)	34.7 (5.02)
RPC Match	87.8 (1.5)	86.3 (1.31)	86.7 (1.14)	86.8 (2.87)	87.3 (1.2)	87.1 (2.08)	87 (1.67)	86.3 (4.34)
Adjacent MB1/MB2 vetoes	93.3 (1.39)	85.2 (1.11)	93.7 (1.07)	90.2 (2.6)	95.7 (1.15)	90.8 (1.89)	96.7 (1.61)	93.5 (4.06)
$ \Delta\phi(\text{cluster}, \vec{E}_T^{\text{miss}}) < 1.0$	98.6 (1.4)	95.9 (1.07)	96.7 (1.03)	94.8 (2.46)	99.8 (1.14)	100 (1.89)	98.1 (1.58)	96.3 (3.91)
$N_{\text{rechits}} \geq 100$	49.2 (0.675)	56.2 (0.603)	34.5 (0.356)	34.4 (0.845)	66.3 (0.759)	69.4 (1.31)	56.8 (0.896)	57.6 (2.25)
CSC/Combination veto	95.7 (0.646)	99.7 (0.601)	96.6 (0.344)	98.9 (0.836)	98.1 (0.745)	98.8 (1.29)	98.7 (0.884)	99.3 (2.23)
MB2	45.1	36.6	47.4	44.4	38.3	30.3	37.7	37.8
MB3	35.0	42.1	36.4	37.0	38.3	38.8	41.1	39.3
MB4	19.8	21.2	16.2	18.6	23.4	30.8	21.2	22.8

Table 28: Signal efficiency (%) for each cut for dark photon portal Dark Shower models with a long-lived particle with various masses, lifetimes, and dark sector mass hierarchies. The cuts are made sequentially, and the reported efficiency is with all previous cuts applied, except for the final three lines which show the percentage of events in the three signal regions. The overall efficiency relative to the first line is included in parentheses.

Selection	2 GeV				15 GeV			
	0.5m		5m		0.5m		5m	
	(1.0, 1.0)	(2.5, 2.5)	(1.0, 1.0)	(2.5, 2.5)	(1.0, 1.0)	(2.5, 2.5)	(1.0, 1.0)	(2.5, 2.5)
$E_T^{\text{miss}} > 200$, E_T^{miss} filters, HLT	0.75	0.0338	1.03	0.362	0.943	0.153	1.17	0.586
$N_{\text{jets}} > 0$	99.8 (99.8)	99.9 (99.9)	99.6 (99.6)	99.8 (99.8)	99.6 (99.6)	99.9 (99.9)	99.6 (99.6)	99.7 (99.7)
$\min \Delta\phi(\text{jet}, \vec{E}_T^{\text{miss}}) > 0.6$	52.2 (52.1)	9.71 (9.7)	69.3 (69.1)	33.5 (33.4)	70.5 (70.2)	22.1 (22.1)	78.5 (78.2)	50.1 (49.9)
$N_{\text{clusters}} > 0$	2.23 (1.16)	1.87 (0.182)	1.46 (1.01)	1.3 (0.434)	7.55 (5.3)	31.4 (6.94)	6.1 (4.77)	16.2 (8.08)
$N_{\text{DT segments veto}}$	94.9 (1.1)	100 (0.182)	92.1 (0.926)	93.3 (0.403)	94.0 (4.98)	85.8 (5.95)	93.5 (4.46)	89.5 (7.23)
Leading jet pass ID	100 (1.1)	100 (0.182)	100 (0.926)	100 (0.403)	100 (4.98)	100 (5.95)	100 (4.46)	100 (7.23)
Jet veto	20.5 (0.226)	55.3 (0.1)	18.2 (0.169)	16.9 (0.0683)	41.2 (2.05)	44.4 (2.64)	52.1 (2.33)	51.7 (3.74)
Muon veto	100 (0.226)	37.5 (0.0377)	100 (0.169)	100 (0.0683)	99.4 (2.04)	98.8 (2.61)	99.4 (2.31)	99.3 (3.71)
MB1/MB2 vetoes	6.6 (0.0149)	0 (0)	6.8 (0.0114)	6.02 (0.00411)	18.9 (0.386)	21.2 (0.553)	27.3 (0.631)	25.4 (0.941)
RPC Match	90.7 (0.0135)	–	90.7 (0.0104)	0 (0)	87.3 (0.336)	89.2 (0.493)	86.7 (0.548)	85.3 (0.803)
Adjacent MB1/MB2 vetoes	100 (0.0135)	–	100 (0.0104)	–	91.1 (0.307)	90.7 (0.447)	92.4 (0.506)	86.5 (0.694)
$ \Delta\phi(\text{cluster}, \vec{E}_T^{\text{miss}}) < 1.0$	76.8 (0.0104)	–	82.4 (0.00862)	–	99.6 (0.305)	100 (0.447)	95.9 (0.485)	91.1 (0.632)
$N_{\text{rechits}} \geq 100$	16.2 (0.00169)	–	14.8 (0.00128)	–	44.9 (0.137)	63.2 (0.283)	35.7 (0.173)	43.2 (0.273)
CSC/Combination veto	100 (0.00169)	–	97.6 (0.00125)	–	97.3 (0.133)	97.5 (0.276)	99.2 (0.172)	99.3 (0.271)
MB2	0.00	–	100.	–	47.0	32.4	49.9	50.1
MB3	100.	–	0.00	–	35.2	32.9	34.8	35.0
MB4	0.00	–	0.00	–	17.8	34.6	15.2	14.9

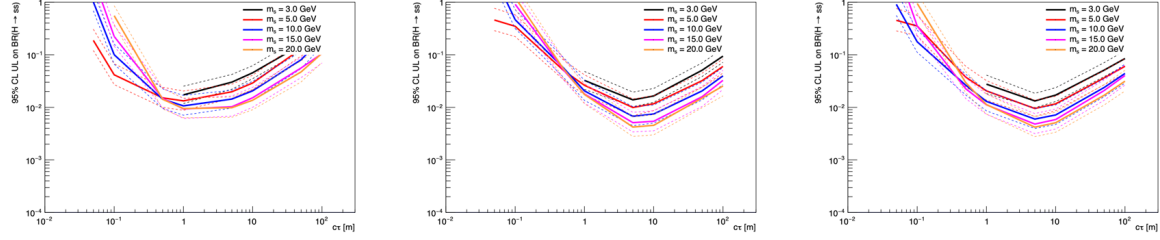


Figure 56: Expected limit on $\text{BR}(\text{H} \rightarrow \text{ss})$ for Higgs Dark Shower model with gluon portal and mass ratios $x_{i\omega} = x_{i\Lambda} = 1.0$ (left), $x_{i\omega} = 2.5, x_{i\Lambda} = 1.0$ (middle), and $x_{i\omega} = x_{i\Lambda} = 2.5$ (right).

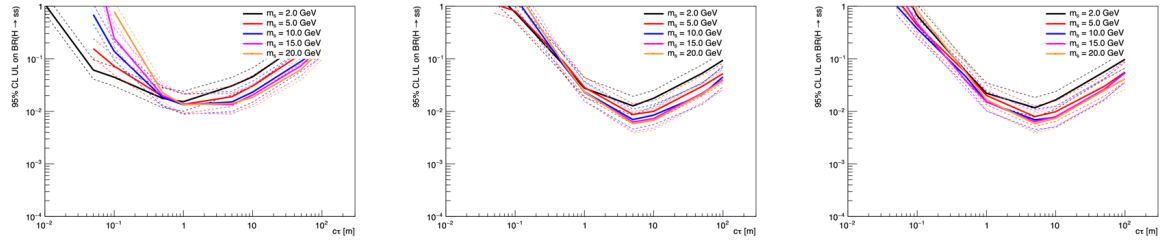


Figure 57: Expected limit on $\text{BR}(\text{H} \rightarrow \text{ss})$ for Higgs Dark Shower model with photon portal and mass ratios $x_{i\omega} = x_{i\Lambda} = 1.0$ (left), $x_{i\omega} = 2.5, x_{i\Lambda} = 1.0$ (middle), and $x_{i\omega} = x_{i\Lambda} = 2.5$ (right).

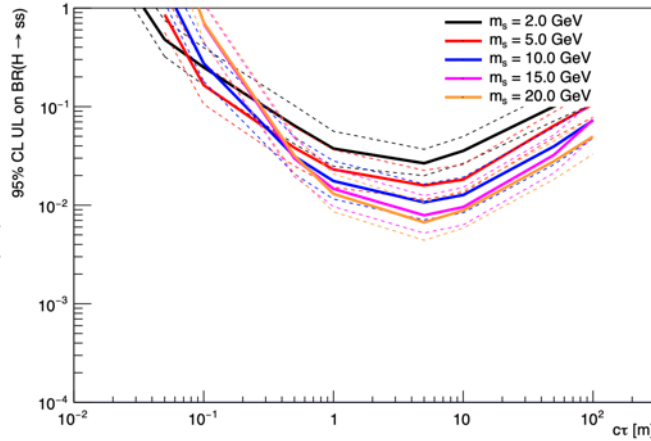


Figure 58: Expected limit on $\text{BR}(\text{H} \rightarrow \text{ss})$ for Higgs Dark Shower model with vector portal and mass ratio $x_{i\omega} = x_{i\Lambda} = 1.0$.

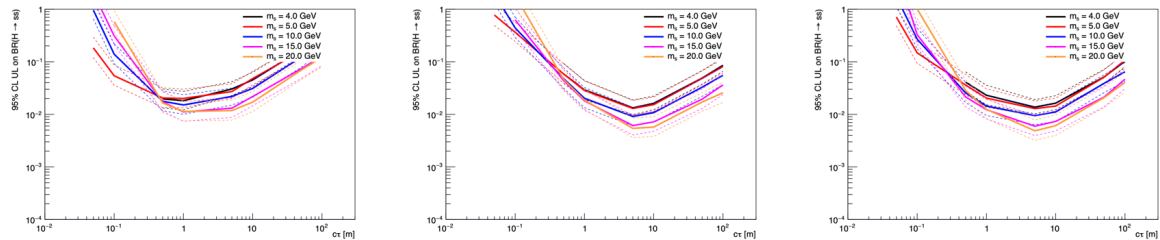


Figure 59: Expected limit on $\text{BR}(\text{H} \rightarrow \text{ss})$ for Higgs Dark Shower model with Higgs portal and mass ratios $x_{i\omega} = x_{i\Lambda} = 1.0$ (left), $x_{i\omega} = 2.5, x_{i\Lambda} = 1.0$ (middle), and $x_{i\omega} = x_{i\Lambda} = 2.5$ (right).

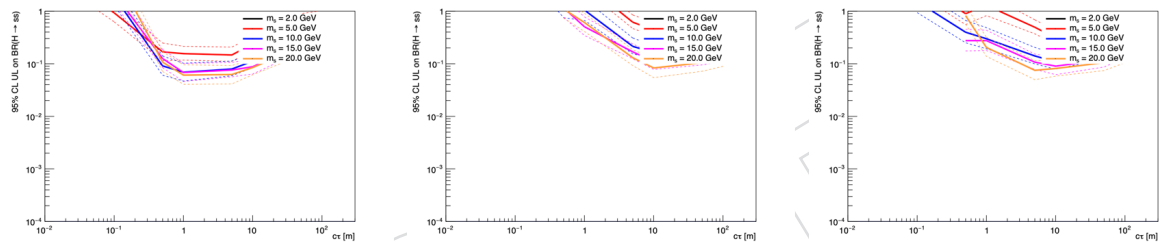


Figure 60: Expected limit on $\text{BR}(H \rightarrow ss)$ for Higgs Dark Shower model with dark photon portal and mass ratios $x_{i\omega} = x_{i\Lambda} = 1.0$ (left), $x_{i\omega} = 2.5, x_{i\Lambda} = 1.0$ (middle), and $x_{i\omega} = x_{i\Lambda} = 2.5$ (right).

936 **12 Summary**

937 A search for long-lived particles decaying in the Barrel Muon System is reported, based on a
938 data sample of pp collisions collected at $\sqrt{s} = 13$ TeV, with the full Run 2 dataset, correspond-
939 ing to an integrated luminosity of 137 fb^{-1} . The DT hits from the decay are clustered together,
940 and requirements for the clusters reject backgrounds from punch-through jets, primary vertex
941 and cosmic muons, pileup, and noise. The remaining background in the signal regions is pre-
942 dicted using a data-driven ABCD method. The analysis is sensitive to long-lived particles with
943 proper lifetimes from 1-100m, and the expected limits on the Higgs boson branching ratio to
944 long-lived particles are sub-percent level for a range of masses. Additionally, the first limits
945 on a simplified Dark Shower model are set for a variety of dark sector portals, masses, and
946 lifetimes.

DRAFT

Acknowledgments

References

- [1] J. Alimena et al., "Searching for long-lived particles beyond the standard model at the large hadron collider", *Journal of Physics G: Nuclear and Particle Physics* **47** (2020) 090501, doi:10.1088/1361-6471/ab4574.
- [2] ATLAS Collaboration, "Search for long-lived, massive particles in events with a displaced vertex and a muon with large impact parameter in pp collisions at $\sqrt{s} = 13$ TeV with the ATLAS detector", *Phys. Rev. D* **102** (2020) 032006, doi:10.1103/PhysRevD.102.032006, arXiv:2003.11956.
- [3] M. Aaboud et al., "Search for long-lived neutral particles in pp collisions at $\sqrt{s} = 13$ TeV that decay into displaced hadronic jets in the ATLAS calorimeter", *The European Physical Journal C* **79** (2019) doi:10.1140/epjc/s10052-019-6962-6.
- [4] M. Aaboud et al., "Search for long-lived particles produced in pp collisions at $\sqrt{s} = 13$ TeV that decay into displaced hadronic jets in the ATLAS muon spectrometer", *Physical Review D* **99** (2019) doi:10.1103/physrevd.99.052005.
- [5] M. Aaboud et al., "Search for the Production of a Long-Lived Neutral Particle Decaying within the ATLAS Hadronic Calorimeter in Association with a Z Boson from pp Collisions at $\sqrt{s} = 13$ TeV", *Physical Review Letters* **122** (2019) doi:10.1103/physrevlett.122.151801.
- [6] CMS Collaboration, "Search for long-lived particles using displaced jets in proton-proton collisions at $\sqrt{s} = 13$ TeV", 2020. <https://arxiv.org/abs/2012.01581>.
- [7] CMS Collaboration, "Search for Neutral Long-lived Particles Decaying in the CSCs", 2021. <https://cms.cern.ch/iCMS/analysisadmin/cadilines?line=EXO-20-015&tp=an&id=2391&ancode=EXO-20-015>.
- [8] N. Craig, S. Koren, and T. Trott, "Cosmological signals of a mirror twin higgs", *Journal of High Energy Physics* **2017** (2017) doi:10.1007/jhep05(2017)038.
- [9] D. Curtin and C. B. Verhaaren, "Discovering uncolored naturalness in exotic higgs decays", *Journal of High Energy Physics* **2015** (2015) 1, doi:10.1007/jhep12(2015)072.
- [10] S. Knapen, J. Shelton, and D. Xu, "Perturbative benchmark models for a dark shower search program", 2021. <https://arxiv.org/abs/2103.01238>.
- [11] CMS Collaboration, "Search for new particles decaying to a jet and an emerging jet", *JHEP* **02** (2019) 179, doi:10.1007/JHEP02(2019)179, arXiv:1810.10069.
- [12] CMS Collaboration, "Particle-flow reconstruction and global event description with the cms detector", *Journal of Instrumentation* **12** (2017), no. 10, P10003, doi:10.1088/1748-0221/12/10/p10003.

983 A Dark Shower features

984 This section includes MC generator-level distributions for the Dark Shower models used for
 985 interpretation.

986 Figure 61 shows the total number of visible decays when requiring that there is at least one LLP
 987 decay in the Barrel Muon System, for each of the simulated Dark Shower models. Due to the
 988 decays from the vector meson to the scalar meson, the visible content increases for all portals
 989 other than vector portal when $x_{i\omega} = 2.5$. Additionally, due to the intermediate decay from the
 990 dark scalar meson to two vector mediators, the dark photon portal has approximately double
 991 the visible content of the other portals.

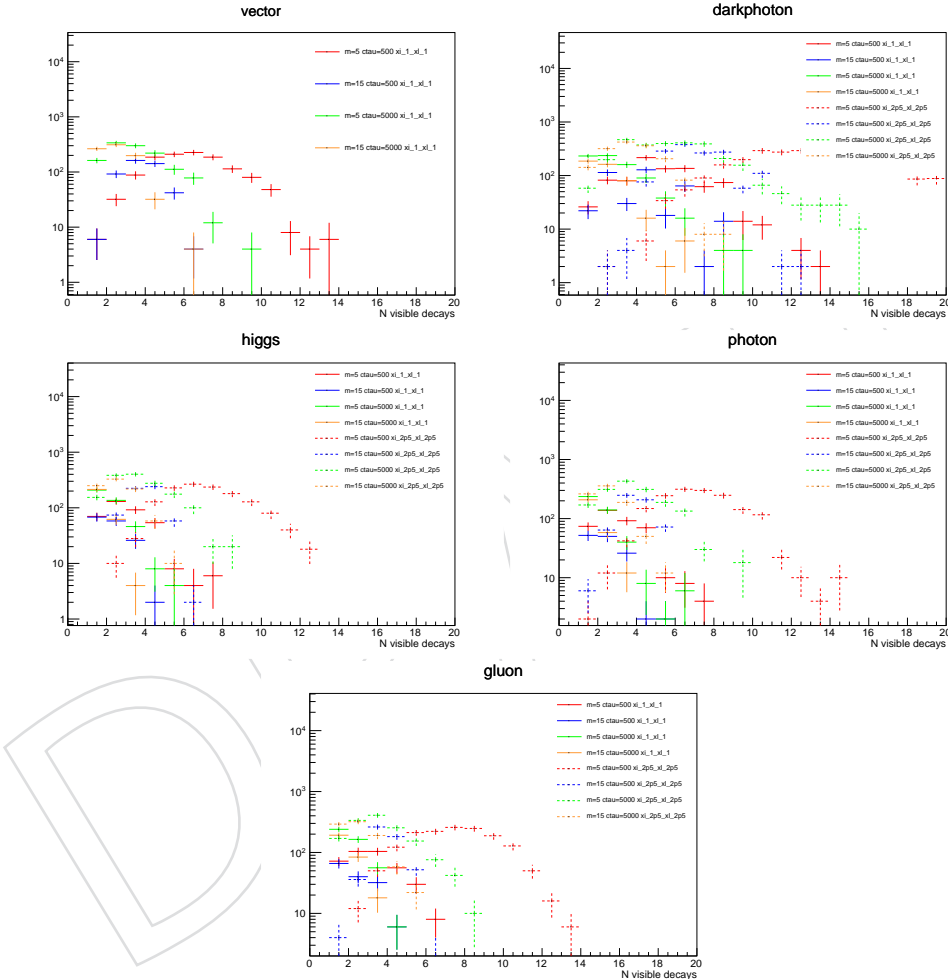


Figure 61: Number of visible decays for events with at least one LLP decay in the Barrel Muon System for each of the Dark Shower models. For $x_{i\omega} = x_{i\Lambda} = 2.5$, the multiplicity tends to be higher, and the dark photon portal has higher multiplicity than the other portals.

992 Figure 62 shows the decay radius for each visible decay in Dark Shower events with at least one
 993 LLP decay in the Barrel Muon System. The distributions increase at 400cm where the muon
 994 system begins since all events have at least one decay there. All decays before 400cm could
 995 lead to objects that veto the DT clusters. Due to the overall higher visible content of the dark
 996 photon portal and $x_{i\omega} = 2.5$ models, there are more decays before the muon system.

997 Figure 63 shows the transverse momentum for each visible decay product in Dark Shower
 998 events with at least one LLP decay in the Barrel Muon System. To cause a cluster, there must

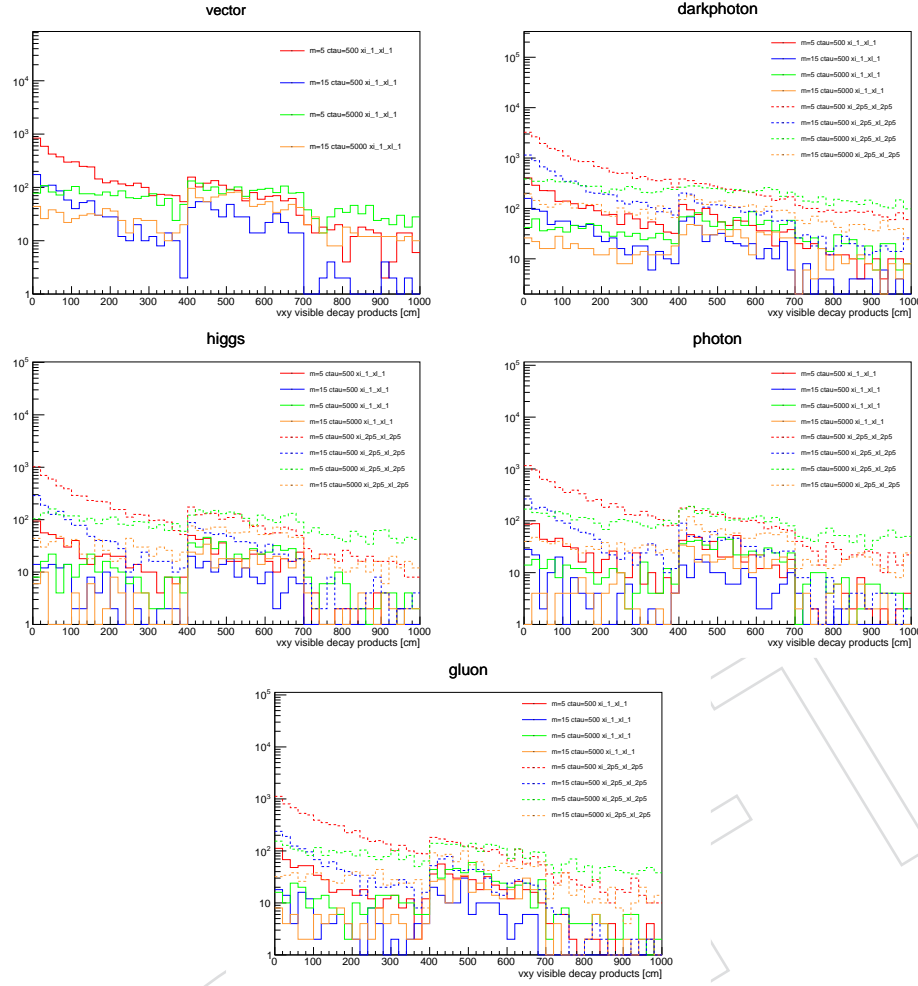


Figure 62: Radius (cm) of visible decays within the dark shower for each model for events with at least one LLP decay in the Barrel Muon System. For models with higher overall visible content ($x_{i\omega} = x_{i\Lambda} = 2.5$ and dark photon portal), there are more decays before the Barrel Muon System begins (400cm) which could lead to vetoes of DT clusters.

999 be visible particles with enough momentum to cause a large number of nearby hits in the DTs.
1000 When the average momentum of visible decay products is lower, the showers are less likely to
1001 cause DT clusters. This leads to a lower probability of finding a cluster for models with higher
1002 multiplicity ($x_{i\omega} = x_{i\Lambda} = 2.5$ and dark photon portal), since the total momentum of the shower
1003 is shared among more decay vertices.

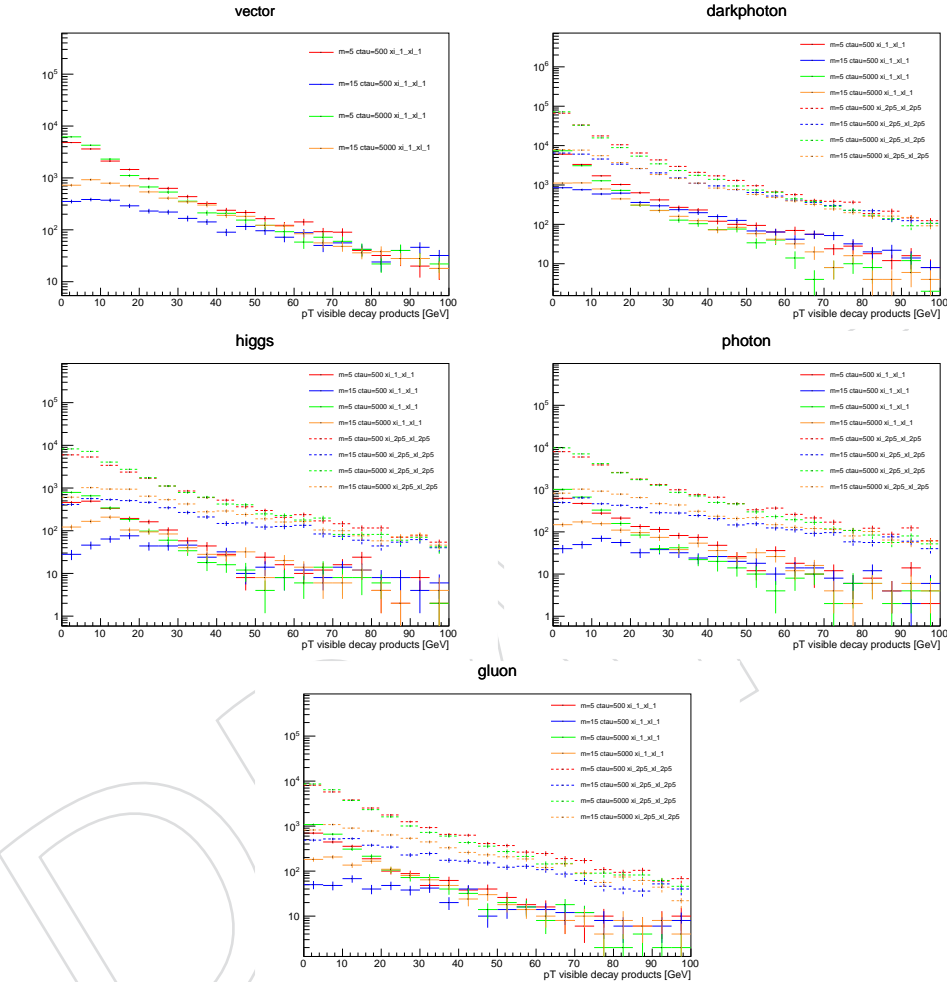


Figure 63: Transverse momentum (GeV) for all visible decay products within the dark shower for events with at least one LLP decay in the Barrel Muon System for each of the Dark Shower models. For models with higher overall visible content ($x_{i\omega} = x_{i\Lambda} = 2.5$ and dark photon portal), the total momentum of the shower is divided among more vertices, so decay products tend to have lower average p_T . Lower p_T decay products are less likely to create enough hits in the DTs to form a cluster.

1004 B Punch-through background

1005 This section includes supplemental material related to the punch-through background.

1006 Figure 64 shows the number of MB1 rechits matched to clusters that fail the jet veto. These
 1007 distributions show the peak near 12 hits, which is one hit per drift tube layer, as well as a peak
 1008 falling off from 0. The clusters matched to fewer than 2 MB1 rechits are the punch-through
 1009 background described and studied in Section 7.2.1.

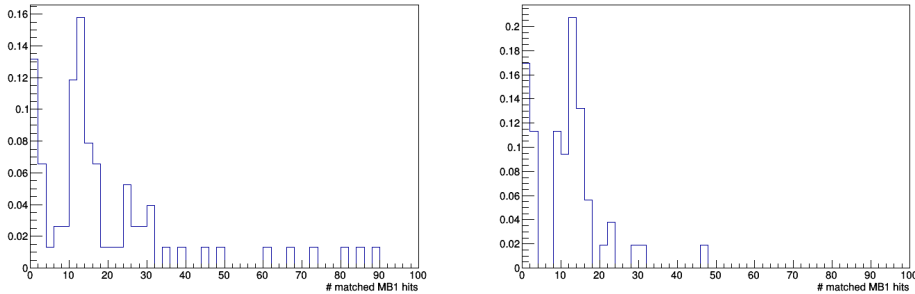


Figure 64: Number of MB1 rechits matched to clusters in MB2 (left) and MB3-4 (right) when clusters are matched to a jet with $p_T > 10$ GeV. All other signal region cuts are applied. Both plots show similar distributions with a peak at 12, the expected number for a MIP passing through MB1, as well as a peak at 0 that falls off rapidly, which contains the clusters that would pass the MB1 veto.

1010 Figure 65 shows the η, ϕ location of clusters that pass the MB1 veto but are matched to jets with
 1011 $p_T > 10$ GeV. The event-level $\Delta\phi(\text{jet}, \vec{E}_T^{\text{miss}})$ is not applied to increase the statistics. Since this is
 1012 just to demonstrate where in the detector these punch-through clusters that pass the MB1 veto
 1013 are formed, removing this cut does not have any impact. The plots do not indicate that this
 1014 behavior is isolated to specific regions of the detector, so these clusters cannot be effectively
 1015 vetoed with just a geometric cut.

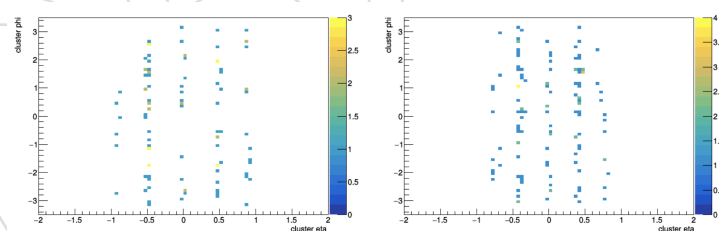


Figure 65: The η, ϕ location of clusters that fail the jet veto but pass the MB1 veto. These clusters are found in all stations, wheels, and phi segments roughly equally. There is no indication that there is a geometric effect causing punch-through clusters to pass the MB1 veto.

1016 Figure 66 shows two different fits for the MB1 veto efficiency as a function of matched jet p_T
 1017 – an exponential and an exponential plus a constant. The fits both perform similarly, with
 1018 a χ^2 per degrees of freedom of 47.0/45 for the exponential and 41.7/44 for the exponential
 1019 plus constant. The exponential only fit predicts an efficiency of 0.254 ± 0.039 at $p_T = 0$, while
 1020 the exponential plus constant fit predicts 0.411 ± 0.104 . The exponential plus constant fit was
 1021 used for the analysis because it is more consistent with the explanation for the clusters in the
 1022 inverted jet veto selection that pass the MB1 veto. The punch-through background has a jet
 1023 p_T -dependent behavior in the MB1 veto efficiency because lower p_T jet constituents bend more
 1024 in the detector so MB1 hits don't necessarily line up with the DT clusters, which gives the

1025 exponential piece of the plot. But there is also a random contribution that passes the MB1
 1026 veto because of gaps in the detector or random overlaps with jets, which would lead to a flat
 1027 contribution to the MB1 veto efficiency plot. Therefore, the exponential plus constant is more
 1028 physically motivated and is the fit used for the signal prediction.

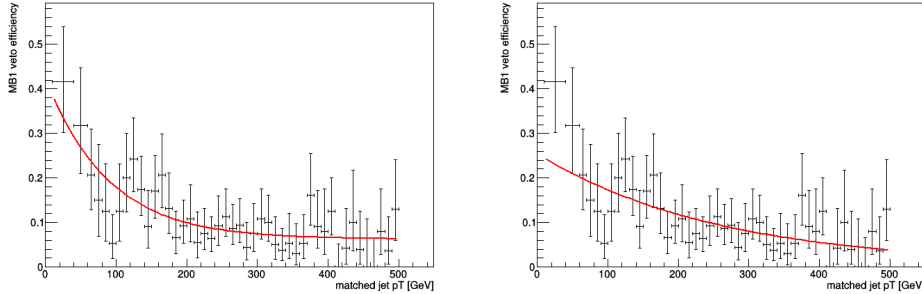


Figure 66: MB1 veto efficiency as a function of matched jet p_T for MB2 clusters, fit to an exponential plus constant (left) and just an exponential (right). The χ^2 per degrees of freedom is similar for the two fits: 41.7/44 (left) and 47.0/45 (right). There is a significant difference between the prediction of the fits for the value at $p_T = 0$. Ultimately, the exponential plus constant fit was chosen for the prediction because it is more physically motivated and consistent with the contributions to this study.

1029 B.1 Event displays

1030 Figure 67 and Figure 68 contain several example event displays for events with clusters that
 1031 are matched to a jet with $p_T > 10$ GeV and pass the MB1 veto, for clusters in MB2 and MB3,
 1032 respectively. As seen in these displays, the dominant source of these types of clusters is that the
 1033 jets punch through a gap in the coverage of the MB1 chambers. This can happen in between the
 1034 ϕ segmentation of MB1 within one wheel or in between the z segmentation of the MB wheels.

1035 As described in Section 7.2.2, high p_T jets are more likely to punch-through anywhere in the
 1036 detector with more particles that can cause MB1 hits, while low p_T jets are more likely to only
 1037 make it to MB2 if they pass through MB1 gaps. Therefore, most of these punch-through clusters
 1038 that pass the MB1 veto are from jets that point to a gap in MB1, but for lower p_T jets this
 1039 represents a larger fraction of the total number of punch-through at that p_T compared to higher
 1040 p_T jets.

1041 For MB3 and MB4 clusters, jets must pass through gaps in all of the inner stations, otherwise if
 1042 they only avoid MB1 they will likely be categorized as MB2 clusters.

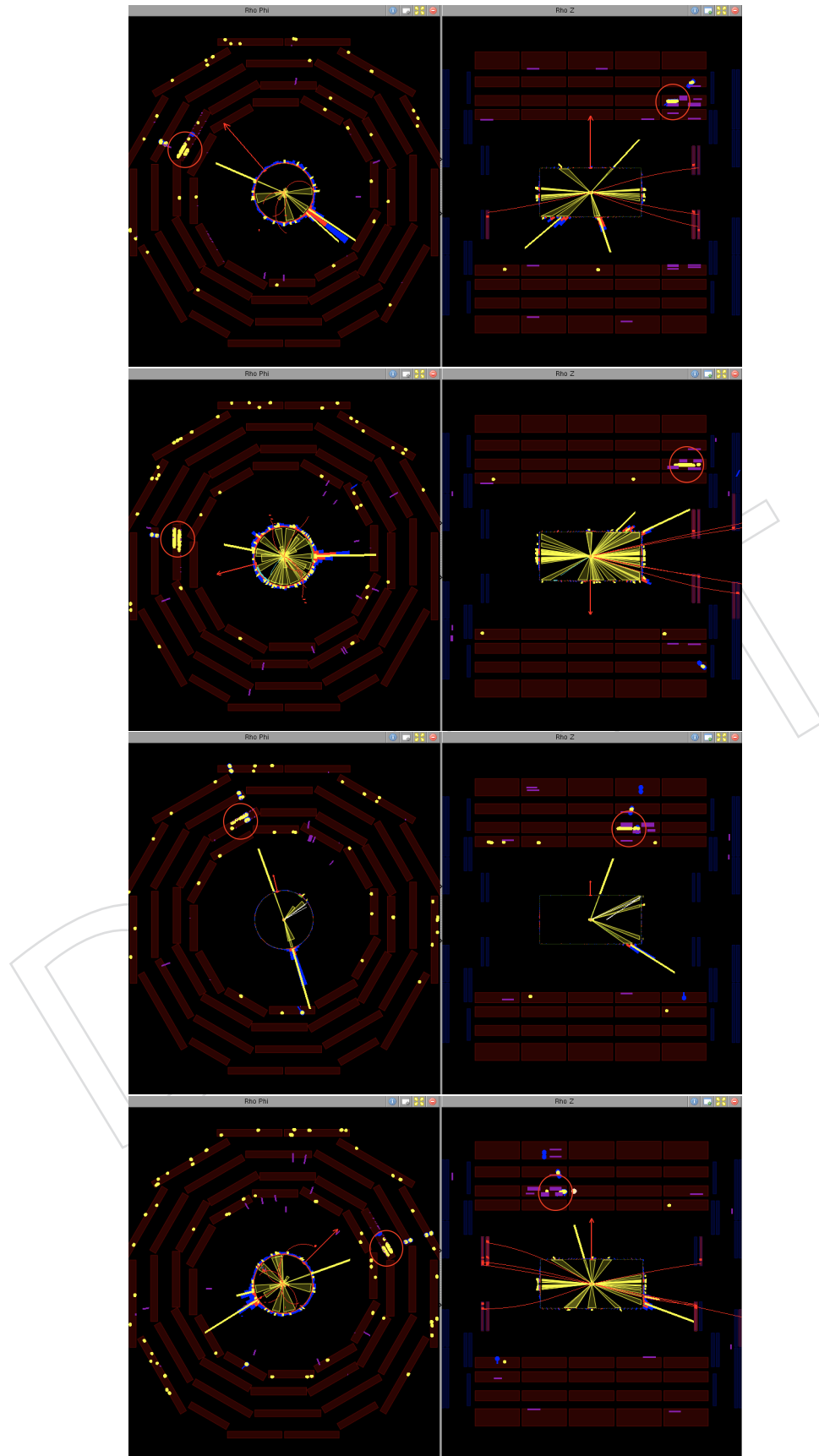


Figure 67: Event displays for events with MB2 clusters that are matched to jets with $p_T > 10$ GeV but pass the MB1 veto.

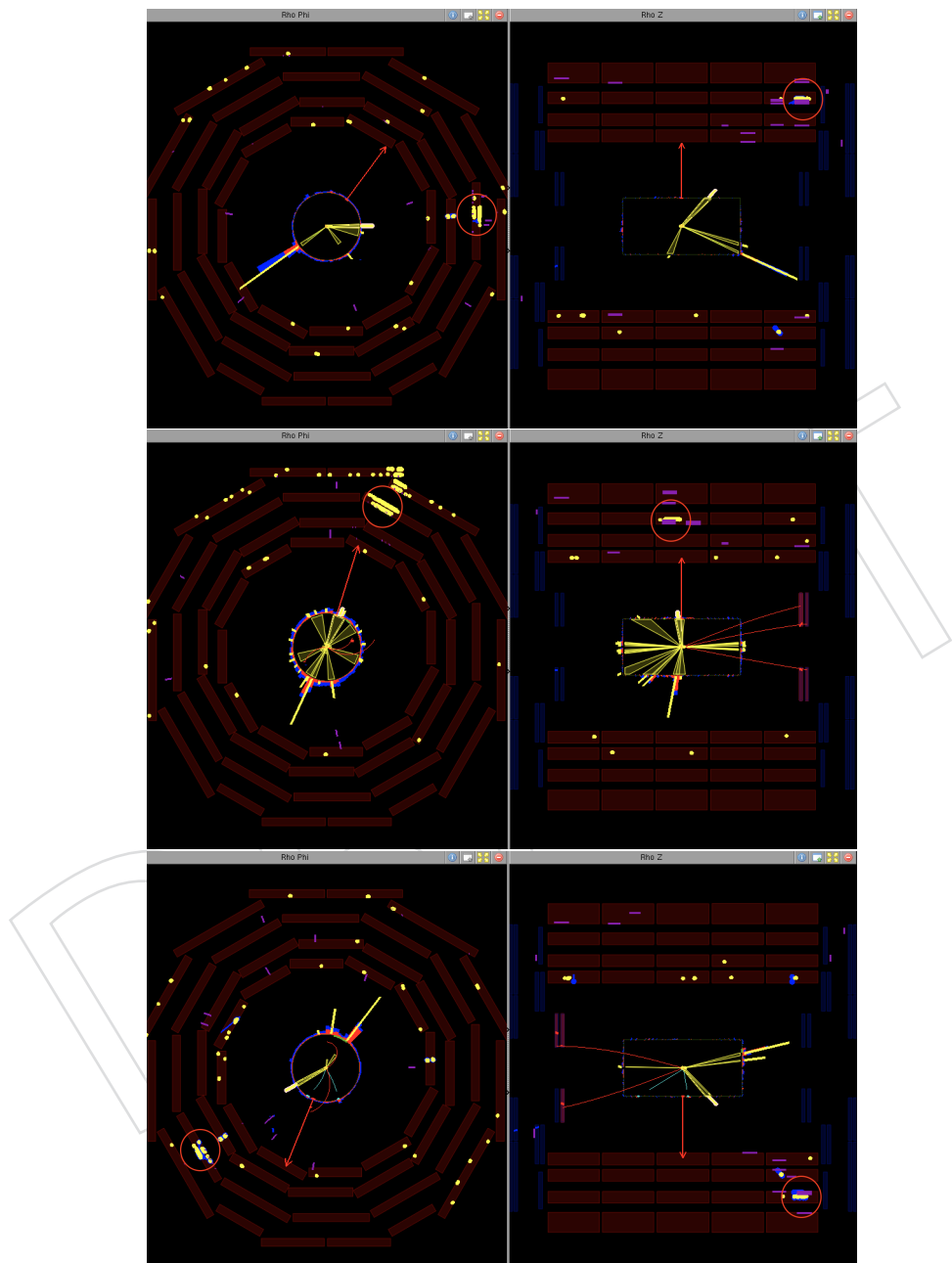


Figure 68: Event displays for events with MB2 clusters that are matched to jets with $p_T > 10$ GeV but pass the MB1 veto.

1043 C Control regions comparison

1044 This section provides comparisons of key variables in different background control regions.
 1045 The first is the inverted MB1 veto control region, which enriches in clusters from punch-through
 1046 and muons. The second is the inverted $|\Delta\phi(\text{cluster}, \vec{E}_T^{\text{miss}})|$ control region, which enriches in
 1047 noise and pileup clusters. Finally, the no RPC match control region, which also enriches in
 1048 noise clusters, is used to study the $|\Delta\phi(\text{cluster}, \vec{E}_T^{\text{miss}})|$ distribution.

1049 All comparisons indicate that there are no significant differences between the different back-
 1050 ground sources, so the signal region cuts are approximately optimal for all the major back-
 1051 grounds. The largest discrepancy can be seen in the jet veto efficiency, where the inverted MB1
 1052 veto background has lower efficiency than inverted $|\Delta\phi(\text{cluster}, \vec{E}_T^{\text{miss}})|$, which is to be expected
 1053 given the enrichment in clusters from punch-through jets, but there is not much to be gained
 1054 from altering that veto.

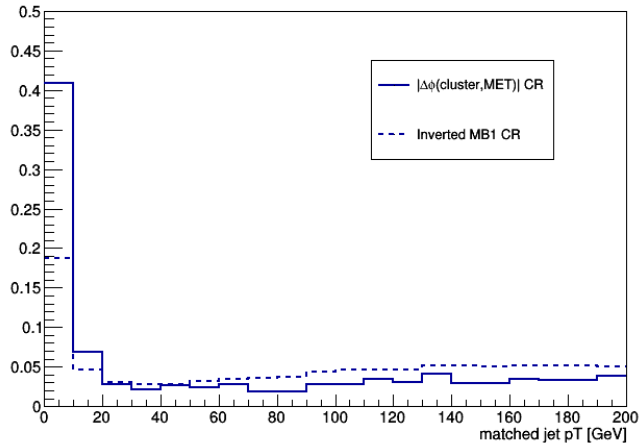


Figure 69: A comparison between background in two different control regions of the variable used for the jet veto: the p_T of the closest jet within $\Delta R < 0.4$ of a cluster, or 0 if there is no matched jet. This value must be less than 10 GeV for signal region clusters.

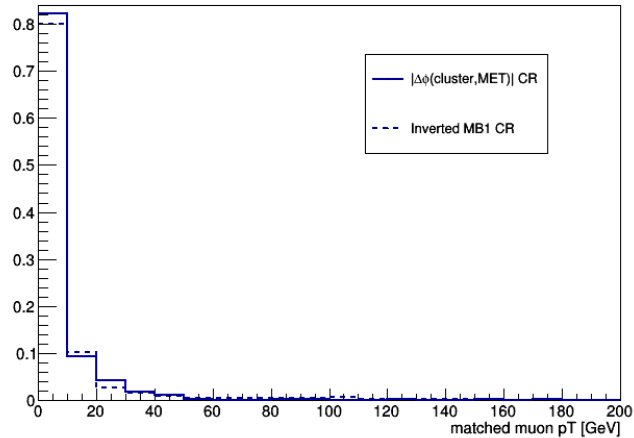


Figure 70: A comparison between background in two different control regions of the variable used for the muon veto: the p_T of the closest loose ID muon within $\Delta R < 0.4$ of a cluster, or 0 if there is no matched muon. This value must be less than 10 GeV for signal region clusters.

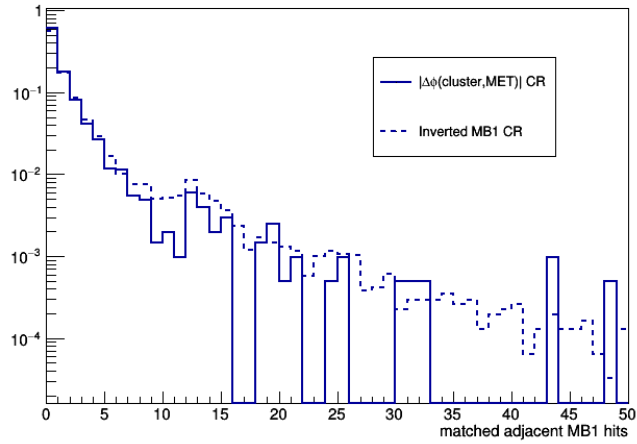


Figure 71: A comparison between background in two different control regions of the number of MB1 rechits from the adjacent wheels matched to a cluster. This value must be 8 or fewer for signal region clusters.

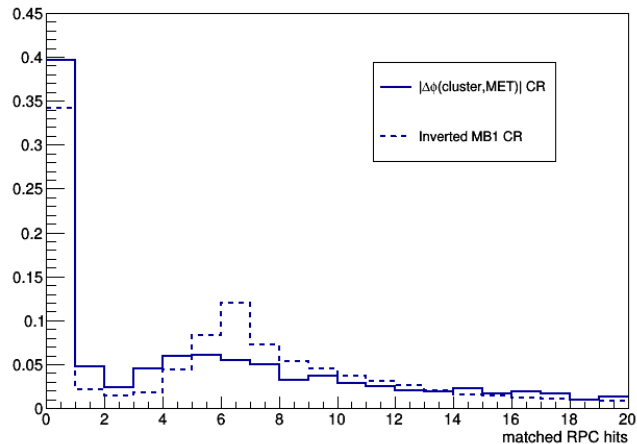


Figure 72: A comparison between background in two different control regions of the number of RPC rechits matched to a cluster. This value must be greater than 0 for signal region clusters.

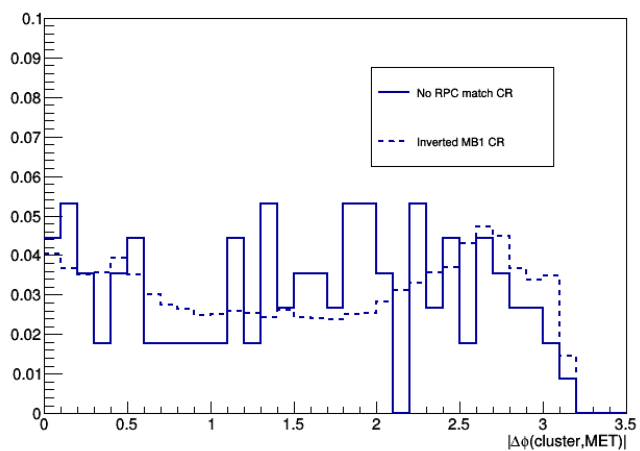


Figure 73: A comparison between background in two different control regions of the $|\Delta\phi(\text{cluster}, \vec{E}_T^{\text{miss}})|$ variable. This value must be less than 1.0 for signal region clusters.

D Dark shower Monte Carlo validation

This section provides a validation of the privately produced dark shower model MC using centrally produced MC samples for a subset of the signal points used for the analysis. The centrally produced samples are for an LLP with a mass of 15 GeV and $c\tau$ 5m. There are samples for all 3 years of data, each of the 5 portals, and the three mass hierarchies ($x_{i\omega}, x_{i\Lambda}$).

The following distributions show various event-level, jet-level, and cluster-level quantities for the private and central samples for each year, portal, and hierarchy. All distributions show good agreement between the two samples.

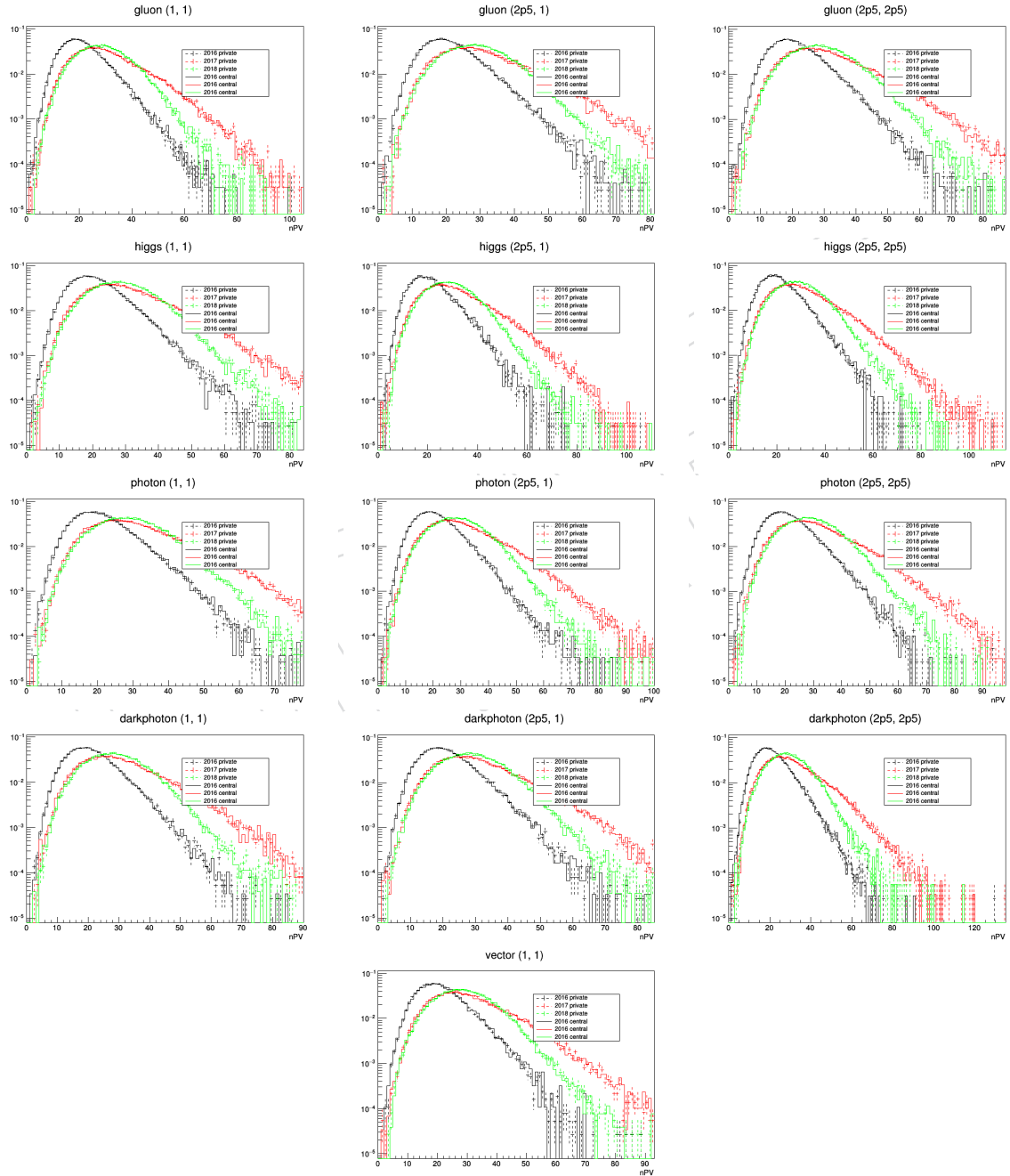


Figure 74: The nPV distributions for privately and centrally produced MC samples for 5 dark shower portals and 3 mass hierarchies.

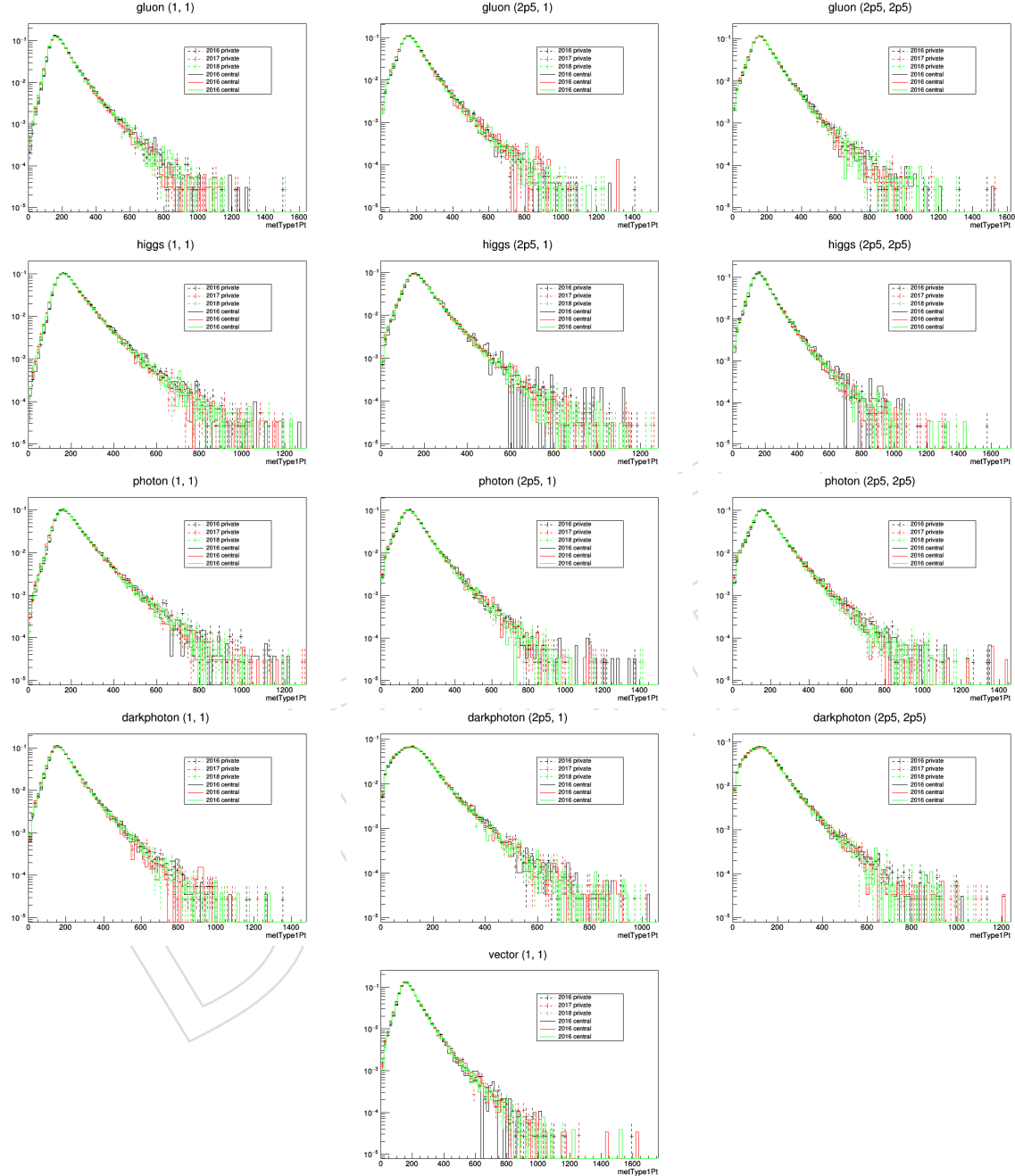


Figure 75: The E_T^{miss} distributions for privately and centrally produced MC samples for 5 dark shower portals and 3 mass hierarchies.

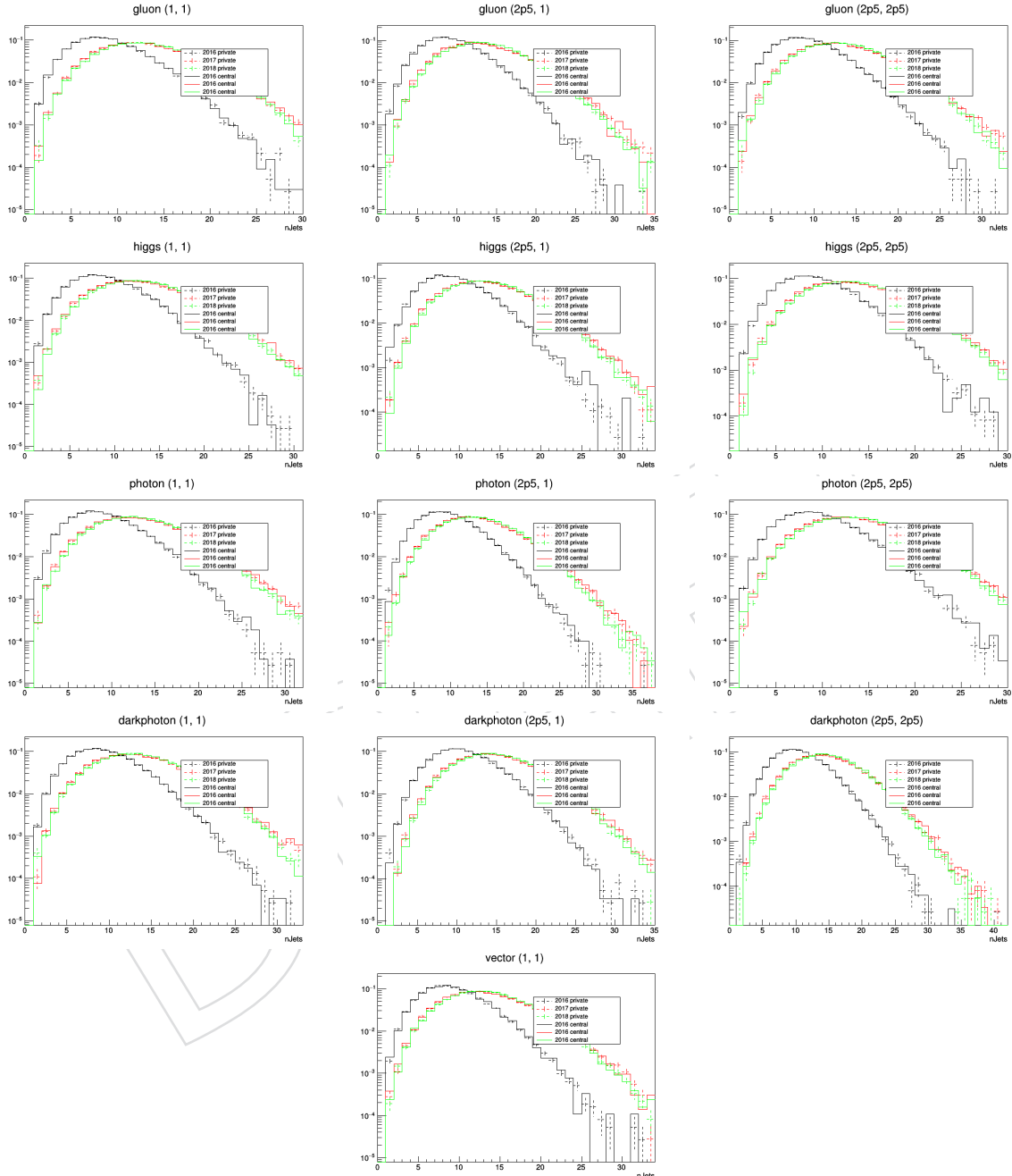


Figure 76: The number of jets distributions for privately and centrally produced MC samples for 5 dark shower portals and 3 mass hierarchies.

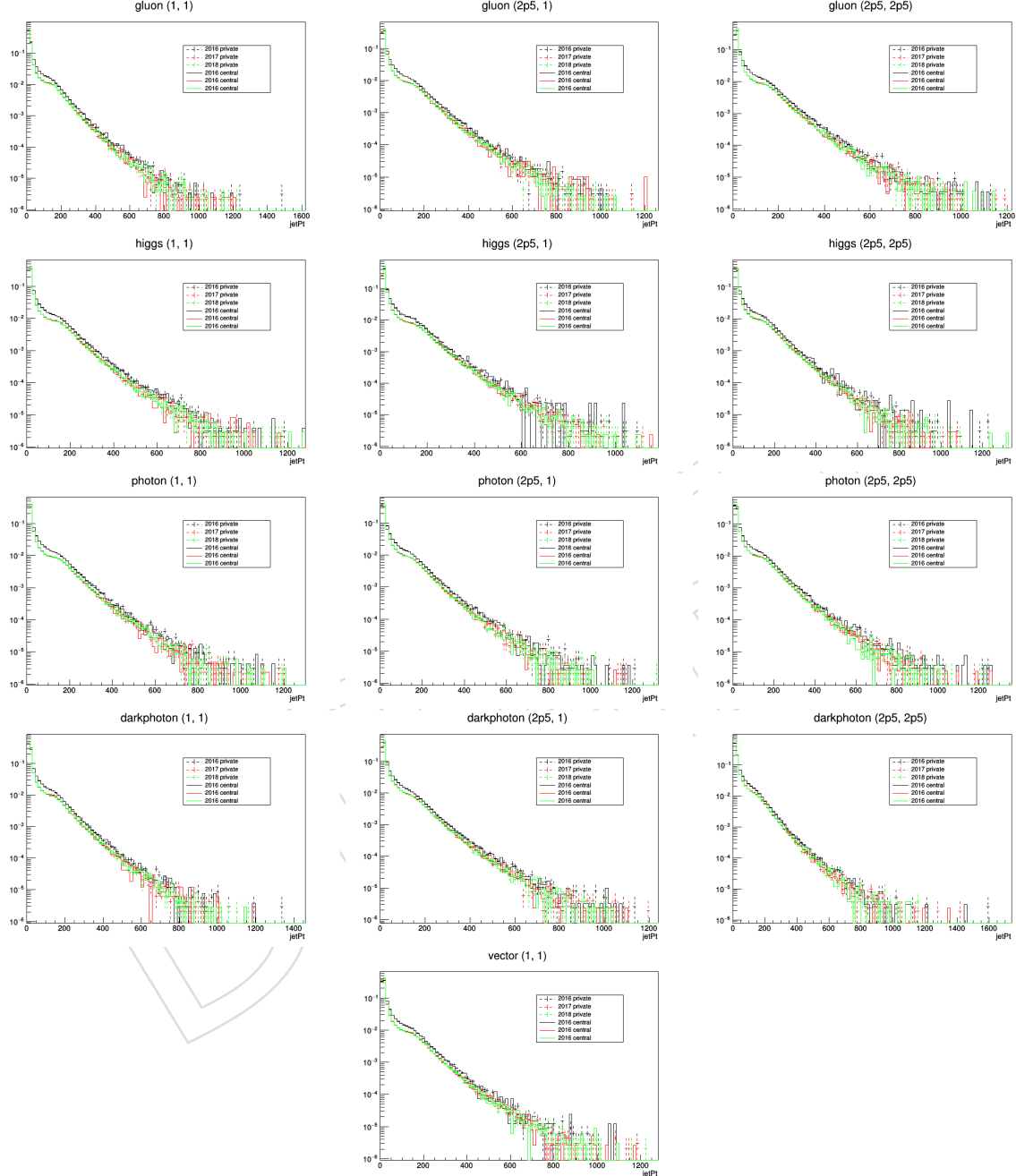


Figure 77: The jet p_T distributions for privately and centrally produced MC samples for 5 dark shower portals and 3 mass hierarchies.

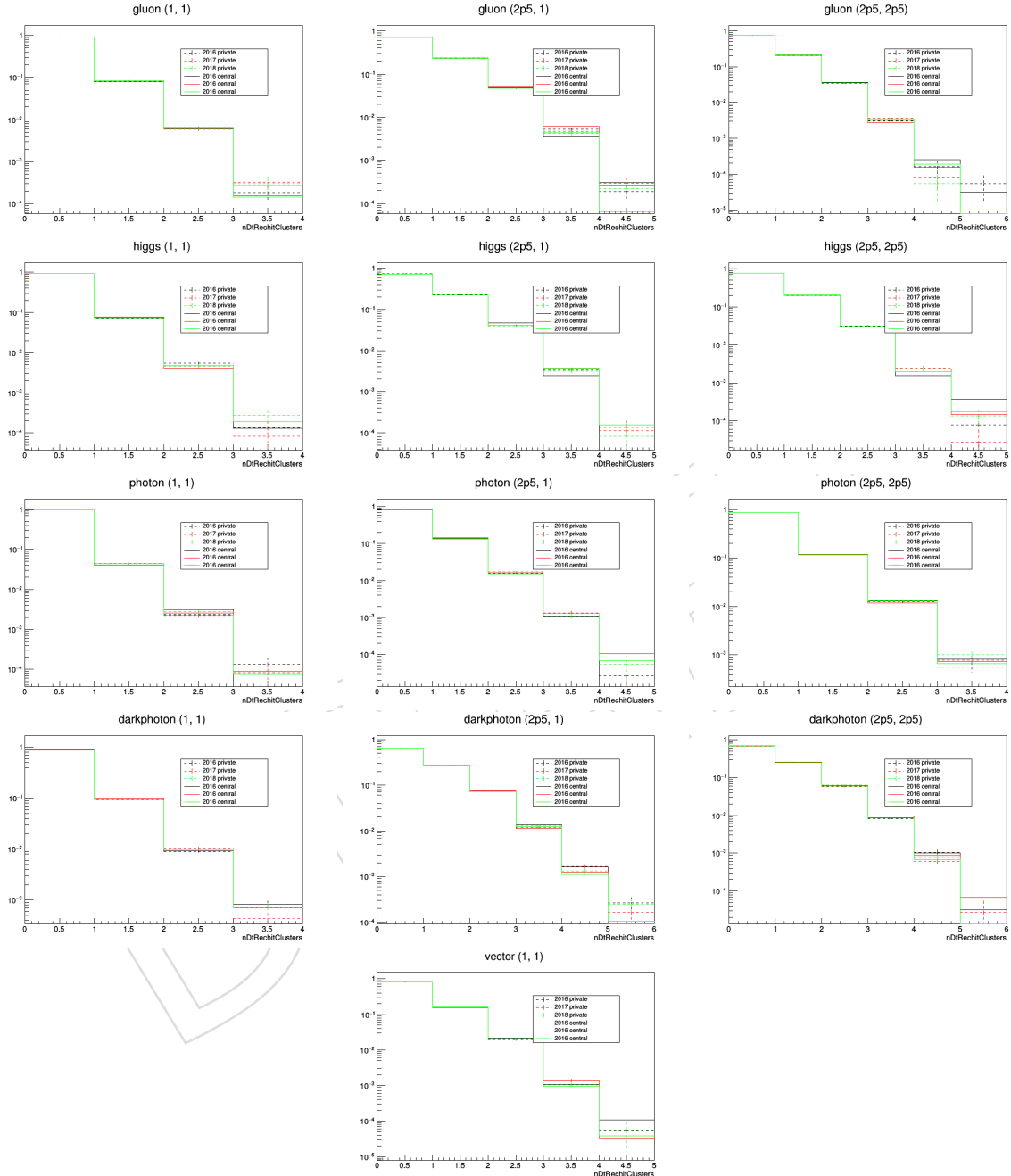


Figure 78: The number of DT clusters distributions for privately and centrally produced MC samples for 5 dark shower portals and 3 mass hierarchies.

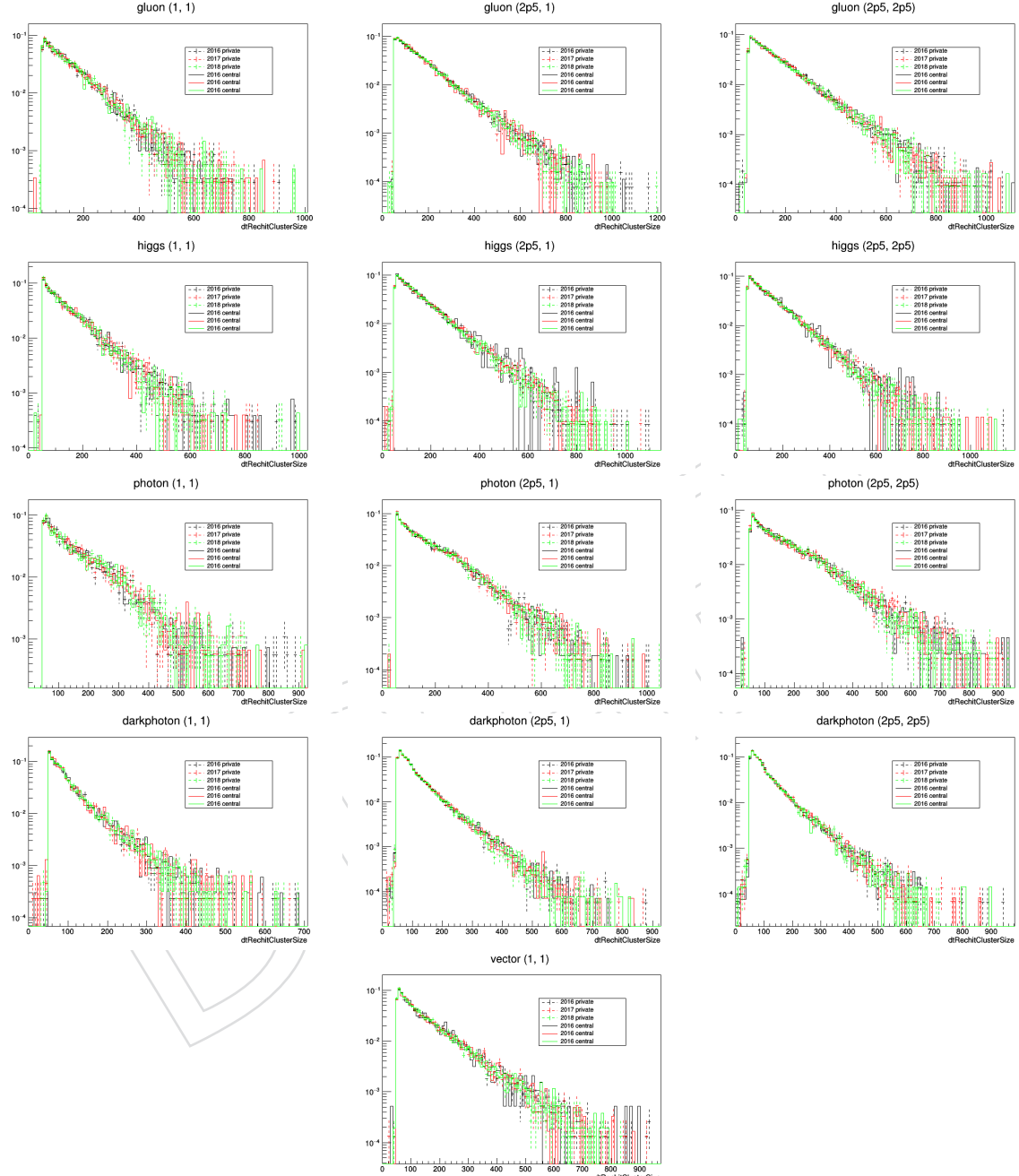


Figure 79: The DT cluster size distributions for privately and centrally produced MC samples for 5 dark shower portals and 3 mass hierarchies.

1063 E Signal efficiency tables

1064 This appendix includes signal efficiency tables that are not included in the main text of the note,
 1065 such as efficiencies for alternative final states and Higgs production modes.

1066 E.1 4d and 4 τ final states

Table 29: Signal efficiency (%) for each cut for Twin Higgs models with a long-lived particle with a mass of 15 GeV and 55 GeV and lifetimes of 0.1m, 1m and 10m for the 4d final state and ggH production. The cuts are made sequentially, and the reported efficiency is with all previous cuts applied, except for the final two lines which show the percentage of events in the two signal regions. The overall efficiency relative to the first line is included in parentheses. The first line is the percentage of ggH production (48.58 fb^{-1}) events that pass the MET requirements.

Selection	15 GeV			55 GeV		
	0.1m	1m	10m	0.1m	1m	10m
$E_T^{\text{miss}} > 200$, E_T^{miss} filters, HLT	0.164	1.01	1.46	0.0016	0.277	0.689
$N_{\text{jets}} > 0$	99.7 (99.7)	99.6 (99.6)	99.5 (99.5)	100 (100)	99.8 (99.8)	99.7 (99.7)
$\min \Delta\phi(\text{jet}, \vec{E}_T^{\text{miss}}) > 0.6$	67.9 (67.7)	85.9 (85.5)	90.5 (90)	7.73 (7.73)	55.9 (55.7)	88.5 (88.2)
$N_{\text{clusters}} > 0$	45.0 (30.5)	27.3 (23.3)	6.55 (5.9)	0 (0)	38.2 (21.2)	17.5 (15.4)
$N_{\text{DT segments veto}}$	98.1 (29.9)	94.8 (22.1)	97.7 (5.76)	–	89.8 (19.1)	96.0 (14.8)
Leading jet pass ID	100 (29.9)	100 (22.1)	100 (5.76)	–	100 (19.1)	100 (14.8)
Jet veto	88.1 (26.3)	88.3 (19.6)	77.6 (4.47)	–	87.1 (16.7)	89.5 (13.3)
Muon veto	100 (26.3)	100 (19.6)	100 (4.47)	–	99.9 (16.6)	100 (13.3)
MB1/MB2 vetoes	17.7 (4.65)	33.6 (6.58)	40.2 (1.8)	–	17 (2.81)	39.1 (5.18)
RPC Match	87.3 (4.06)	88 (5.79)	87.9 (1.58)	–	86.3 (2.43)	87.1 (4.51)
Adjacent MB1/MB2 vetoes	96.3 (3.91)	95.5 (5.53)	97.3 (1.54)	–	92.3 (2.24)	97.9 (4.41)
$ \Delta\phi(\text{cluster}, \vec{E}_T^{\text{miss}}) < 1.0$	100 (3.91)	96.3 (5.33)	84.4 (1.29)	–	100 (2.24)	100 (4.41)
$N_{\text{rechits}} \geq 100$	89 (3.47)	75.2 (4.01)	67.1 (0.871)	–	81.6 (1.83)	73.6 (3.25)
CSC/Combination veto	100 (3.47)	96.3 (3.87)	99.1 (0.863)	–	98.9 (1.81)	99.3 (3.22)
MB2	31.2	25.3	25.4	–	32.0	28.8
MB3	34.6	40.5	40.1	–	42.4	41.6
MB4	34.1	34.2	34.5	–	25.5	30.0

1067 E.2 VBF production

Table 30: Signal efficiency (%) for each cut for Twin Higgs models with a long-lived particle with a mass of 15 GeV and 55 GeV and lifetimes of 0.1m, 1m and 10m for the 4τ final state and ggH production. The cuts are made sequentially, and the reported efficiency is with all previous cuts applied, except for the final two lines which show the percentage of events in the two signal regions. The overall efficiency relative to the first line is included in parentheses. The first line is the percentage of ggH production (48.58 fb^{-1}) events that pass the MET requirements.

Selection	15 GeV			55 GeV		
	0.1m	1m	10m	0.1m	1m	10m
$E_T^{\text{miss}} > 200, E_T^{\text{miss}}$ filters, HLT	0.347	1.13	1.48	0.095	0.302	0.748
$N_{\text{jets}} > 0$	99.8 (99.8)	99.6 (99.6)	99.5 (99.5)	100 (100)	99.9 (99.9)	99.7 (99.7)
$\min \Delta\phi(\text{jet}, \vec{E}_T^{\text{miss}}) > 0.6$	54.3 (54.2)	84.4 (84.1)	90.5 (90)	18.1 (18.1)	55.1 (55)	87.4 (87.1)
$N_{\text{clusters}} > 0$	31.3 (17)	19.6 (16.5)	4.47 (4.02)	11.8 (2.14)	32.8 (18)	11.9 (10.4)
$N_{\text{DT segments}}$ veto	97.4 (16.5)	95.5 (15.7)	96.9 (3.89)	92.6 (1.98)	95.0 (17.2)	96.6 (10)
Leading jet pass ID	100 (16.5)	100 (15.7)	100 (3.89)	100 (1.98)	100 (17.2)	100 (10)
Jet veto	82 (13.5)	86.3 (13.6)	72.8 (2.83)	17.9 (0.354)	74.7 (12.8)	86.3 (8.64)
Muon veto	99.9 (13.5)	100 (13.6)	100 (2.83)	100 (0.354)	99.8 (12.8)	100 (8.64)
MB1/MB2 vetoes	17.5 (2.37)	31.9 (4.32)	35 (0.988)	0 (0)	17.1 (2.18)	31.9 (2.76)
RPC Match	85.8 (2.03)	86.9 (3.75)	87 (0.862)	–	84.3 (1.84)	86.6 (2.38)
Adjacent MB1/MB2 vetoes	95 (1.93)	95.5 (3.58)	97.4 (0.839)	–	85.9 (1.58)	96.5 (2.31)
$ \Delta\phi(\text{cluster}, \vec{E}_T^{\text{miss}}) < 1.0$	100 (1.93)	98.1 (3.52)	87.6 (0.735)	–	100 (1.58)	100 (2.31)
$N_{\text{rechits}} \geq 100$	73.1 (1.41)	63.5 (2.24)	63.2 (0.465)	–	70.5 (1.12)	58.8 (1.35)
CSC/Combination veto	100 (1.41)	96.5 (2.16)	96.2 (0.447)	–	96.6 (1.08)	99.8 (1.35)
MB2	41.3	33.3	32.8	–	43.8	34.9
MB3	36.4	35.3	36.3	–	33.2	37.5
MB4	22.3	31.4	30.9	–	22.9	27.6

Table 31: Signal efficiency (%) for each cut for Twin Higgs models with a long-lived particle with a mass of 15 GeV and 55 GeV and lifetimes of 0.1m, 1m and 10m for the $4b$ final state and VBF production. The cuts are made sequentially, and the reported efficiency is with all previous cuts applied, except for the final two lines which show the percentage of events in the two signal regions. The overall efficiency relative to the first line is included in parentheses. The first line is the percentage of VBF production (3.782 fb^{-1}) events that pass the MET requirements.

Selection	15 GeV			55 GeV		
	0.1m	1m	10m	0.1m	1m	10m
$E_T^{\text{miss}} > 200, E_T^{\text{miss}}$ filters, HLT	0.753	4.69	6.80	0.0103	1.30	5.54
$N_{\text{jets}} > 0$	98.8 (98.8)	97.9 (97.9)	97.6 (97.6)	100 (100)	98.8 (98.8)	97.8 (97.8)
$\min \Delta\phi(\text{jet}, \vec{E}_T^{\text{miss}}) > 0.6$	69.4 (68.6)	87.1 (85.3)	92.4 (90.2)	6.33 (6.33)	53.6 (52.9)	89.3 (87.4)
$N_{\text{clusters}} > 0$	45.0 (30.9)	26.8 (22.9)	6.48 (5.84)	49.1 (3.1)	38.2 (20.2)	17.3 (15.1)
$N_{\text{DT segments}}$ veto	98.8 (30.4)	94.5 (21.6)	98.1 (5.74)	100 (3.1)	89.7 (18.2)	95.7 (14.5)
Leading jet pass ID	100 (30.4)	100 (21.6)	100 (5.74)	100 (3.1)	100 (18.2)	100 (14.5)
Jet veto	87.2 (26.5)	89.3 (19.3)	81.5 (4.68)	0 (0)	84.7 (15.4)	90.8 (13.1)
Muon veto	99.9 (26.5)	100 (19.3)	100 (4.68)	–	99.9 (15.4)	100 (13.1)
MB1/MB2 vetoes	16.7 (4.41)	34.8 (6.72)	39.8 (1.86)	–	15.8 (2.41)	39.7 (5.21)
RPC Match	86.5 (3.81)	87 (5.84)	86.4 (1.61)	–	86.2 (2.08)	85.7 (4.73)
Adjacent MB1/MB2 vetoes	94.8 (3.62)	96.1 (5.61)	97.7 (1.57)	–	90.6 (1.89)	96.4 (4.56)
$ \Delta\phi(\text{cluster}, \vec{E}_T^{\text{miss}}) < 1.0$	100 (3.62)	96.3 (5.41)	78.6 (1.23)	–	100 (1.89)	100 (4.56)
$N_{\text{rechits}} \geq 100$	86.8 (3.14)	70.1 (3.79)	64.8 (0.801)	–	83.4 (1.57)	71.9 (3.28)
CSC/Combination veto	100 (3.14)	99.4 (3.76)	98.5 (0.789)	–	98.4 (1.55)	99.9 (3.27)
MB2	32.0	27.9	29.1	–	34.0	29.7
MB3	36.9	38.8	36.9	–	42.5	42.3
MB4	31.1	33.2	34.0	–	23.6	28.0